UNIVERSITY OF CALIFORNIA

Los Angeles

Phase Change Materials and Clinkering-Free Cementation

for Sustainable Building Materials

A dissertation submitted in partial satisfaction

of the requirements for the degree Doctor of Philosophy

in Civil Engineering

by

Zhenhua Wei

2017

ABSTRACT OF THE DISSERTATION

Phase Change Materials and Clinkering-Free Cementation

for Sustainable Building Materials

by

Zhenhua Wei

Doctor of Philosophy in Civil Engineering

University of California, Los Angeles, 2017

Professor Laurent G. Pilon, Co-Chair

Professor Gaurav Sant, Co-Chair

Ordinary portland cement (OPC) has been used as the primary binding material in concrete for construction of buildings and other infrastructure over the last century due to its low-cost and the widespread geographical abundance of its raw materials. The manufacture of OPC accounts for approximately 3% of primary energy use and 9% of anthropogenic CO_2 emissions globally. Such energy consumption and CO_2 release is mainly attributed to the calcination and clinkering of raw materials (i.e., limestone and clay) in the cement kiln at high temperatures. Therefore, there is great need to reduce the CO_2 footprint of cement, and secure alternative solutions for cementation as required for building and infrastructure construction. On the other hand, space conditioning consumes nearly 20% of annual energy consumption in the United States, which is still increasing with the increasing demand for thermal comfort in the context of climate change. The embedment of phase change materials (PCMs) in concrete is an effective means to improve its thermal inertia

for building envelope applications, and can thus improve the energy efficiency of buildings. However, the viability of employing PCMs to enhance thermal performance of concrete depends on the stability and durability of PCMs in the highly caustic cementitious environment, and the durability of the PCM-added concrete. To address these limitations on sustainability and energy efficiency of current cement-based building materials, this dissertation mainly examines:

- PCM survivability during fabrication of PCM-mortar composites with respect to damage and/or rupture of the PCM microcapsules that may occur during mechanical mixing, as well as chemical durability of PCM within cementitious matrices, and the potential interactions between the PCM and the pore-fluid that result in enthalpy alteration,

- Cementitious matrix durability, with emphasis on assessing how dosage of PCMs alters water absorption, drying shrinkage, and restrained shrinkage cracking behaviors of cementitious composites containing PCMs, and

- The feasibility of developing sustainable building material through clinkering-free cementation by fly ash carbonation, with emphasis on the effects of CO_2 concentration and processing temperature on the progress of carbonation reaction, the development of microstructure, and the strength evolution of the material.

The results of research on PCM embedded cementitious composites show that a reduction of around 25% in the phase change enthalpy is observed, irrespective of PCM dosage and aging. Such reduction in enthalpy is mainly caused by chemical interactions with dissolved sulfate ions. Examination of the influence of PCM additions on water absorption and drying shrinkage of PCM-mortar composites reveals that PCM microcapsules reduce the rate and extent of water sorption due to their non-sorptive nature and diluting effect. PCM inclusions do not influence the drying shrinkage of cementitious composites due to their inability to restrain the shrinkage of the cement

paste. Assessments of free and restrained shrinkage, elastic modulus, and tensile strength also show that the addition of PCMs enhances the cracking resistance of cement paste because PCMs as soft inclusions offer crack blunting and deflection, and improved stress relaxation. In an effort to synergize the utilization of fly ash and CO_2 in fly ash, the study shows that Ca-rich fly ash paste can readily react with dilute concentrations of CO_2 in moist environments to produce cemented solids with sufficient strength (35 MPa) for use in structural construction. Detailed results from thermodynamic modeling, XRD analyses, and SEM observations suggest that fly ash carbonation results in the formation of reaction products including calcite, hydrous silica, and C-S-H, which collectively bond proximate particles into a cemented solid.

The dissertation of Zhenhua Wei is approved.

Mathieu Bauchy

Scott Joseph Brandenberg

Laurent G. Pilon, Committee Co-Chair

Gaurav Sant, Committee Co-Chair

University of California, Los Angeles

2017

Table of Contents

List of Tables

Acknowledgements

I would like to thank my advisors and dissertation committee chairs, Professors Gaurav Sant and Laurent Pilon for their support and guidance throughout my Ph.D. work. Their mentoring and supervision have allowed me to learn and develop useful skills. I would like to extend my appreciation to Professors Mathieu Bauchy and Scott Brandenberg for being on my committee.

Thank you to all my friends, past and current members of LCC/PARISlab, and my research collaborators for their support.

Most importantly, I would like to express my utmost gratitude to my family for their steadfast patience, love, understanding, and encouragement throughout my Ph.D. journey. Their support has been invaluable to me and has made this journey possible.

Vita

2010	B.S. in Agricultural Engineering
	Huazhong Agricultural University
	Wuhan, China
2011-2013	Research Assistant
	Institute of Oceanology, Chinese Academy of Sciences
	Qingdao, China
2013	M.S. in Materials Science
	University of Chinese Academy of Sciences
	Beijing, China
2013-2017	Research/Teaching Assistant
	University of California, Los Angeles
	Los Angeles, California

Publications

B. Young, G. Falzone, Z. Wei, G, Sant, P. Pilon. Reduced-scale experiments to evaluate performance of composite building envelopes containing phase change materials. Construction and Building Materials 2017 (under review)

Z. Wei, B. Wang, G. Falzone, E. La Plante, M. Okoronkwo, Z. She, T. Oey, M. Balonis, N. Neithalath, L. Pilon, G. Sant. Clinkering-free cementation by fly ash carbonation. Journal of CO_2 Utilization 2017 (accepted)

Z. Wei, A. G. Falzone, S. Das, N. Saklani, Y. Le Pape, L. Pilon, N. Neithalath, G. Sant. Restrained shrinkage cracking of cementitious composites containing soft PCM inclusions: A paste (matrix) controlled response. Materials and Design 2017, 132, 367-374

Z. Wei, G. Falzone, B. Wang, A. Thiele, G. Puerta Falla, L. Pilon, N. Neithalath, G. Sant. The durability of cementitious composites containing microencapsulated phase change materials. Cement and Concrete Composites 2017, 81, 66-76

B. Young, G. Falzone, Z. She, A. Thiele, Z. Wei, N. Neithalath, L. Pilon, G. Sant. Early-age temperature evolutions in concrete pavements containing microencapsulated phase change materials. Construction and Building Materials 2017, 147, 466-477

B. Young, Z. Wei, J. R. Cruz, G. Falzone, A. Kumar, N. Neithalath, G, Sant, L. Pilon. A general method for retrieving thermal deformation properties of microencapsulated phase change materials or other particulate inclusions in cementitious composites. Materials and Design 2017, 126, 259-267

Y. Gu, Z. Wei, X. Shu, Q. Ran, K. Lv, J. Liu. Characterizing cement paste containing SRA modified nanoSiO2 and evaluating its strength development and shrinkage behavior. Cement and Concrete Composites 2017,75, 30-37

A. Thiele, Z. Wei, G. Falzone, B. Young, N. Neithalath, G. Sant, L. Pilon. Figure of merit for the performance of cementitious composites containing phase change materials. Cement and Concrete Composites 2016, 65, 214-226

G. Fazone, G. Puerta, Z. Wei, M. Zhao, A. Kumar, M. Bauchy, N. Neithalath, L. Pilon, G. Sant. The influences of soft and stiff inclusions on the mechanical properties of cementitious composites. Cement and Concrete Composites 2016, 71, 153-165

Z. Liu, S. Wang, J. Huang, Z. Wei, B. Guan, J. Fang. Experimental investigation on the properties and microstructure of magnesium oxychloride cement prepared with caustic magnesite and dolomite. Construction and Building Materials 2015, 85, 247-255

F. Fernandes, S. Manari, M. Aguayo, K. Santos, T. Oey, Z. Wei, G. Falzone, N. Neithalath, G. Sant. On the feasibility of using phase change materials (PCMs) to mitigate thermal cracking in cementitious materials. Cement and Concrete Composites 2014, 51, 14-26

Chapter 1 Introduction

1.1 Background

At a global production level of 4.2 billion tons, the production of ordinary portland cement (OPC) accounts for approximately 3% of primary energy use and 9% of anthropogenic CO_2 emissions [1]. Such CO_2 release is attributed to factors including: (i) the combustion of fuel required for clinkering the raw materials (i.e., limestone and clay) at 1450 °C [2], and (ii) the release of CO_2 during the calcination of limestone in the cement kiln [3, 4]. As a result, around 0.9 tons of CO_2 are emitted per ton of OPC produced [3-5]. Due to the fact that OPC is currently used as the principle component in concrete formulations for construction of buildings and other infrastructure, and the booming modernization and retrofitting of infrastructure all around the world, the demand of energy consumption and CO_2 emission in the construction sector is expected to expand in the foreseeable future [6-8]. Therefore, there is great interest to reduce CO_2 footprint in concrete and to seek alternatives to OPC and traditional cementation [3].

While considerable efforts have been made to replace OPC in the binder fraction of concrete by supplementary cementitious materials (SCMs) such as fly ash, the extent of such utilization remains limited [9, 10]. For example, in spite of supportive frameworks in the U.S., only around 45% of all fly ash produced annually is beneficially utilized to replace OPC in the concrete [9, 11]. such limited use is due to factors including: (i) the presence of impurities including air-pollution control (APC) residues and unburnt carbon as a result of which some fly ashes are non-compliant (e.g., as per ASTM C618 [12]) for use in traditional OPC concrete, due to durability concerns [13, 14], and, (ii) increasing cement replacement (i.e., fly ash dosage) levels to greater than 25 mass %

1

is often associated with extended setting times and slow strength gain resulting in reduced constructability of the concrete [15, 16]. Clearly, there is an immediate need to valorize or beneficially utilize ("upcycle") vapor and solid wastes associated with coal power production. However, given the tremendous scale of waste production, there is a need to secure upcycling opportunities of some prominence; e.g., within the construction sector wherein large-scale utilization of upcycled materials can be achieved. This condition could be satisfied if the "upcycled solution" is able to serve as an alternative to OPC (and OPC-concrete) so long as it is able to fulfill the functional and performance requirements of construction. Mineral carbonation (i.e., conversion of vapor phase CO_2 into a carbonaceous mineral; e.g., CaCO3) has been proposed as a promising route to sequester CO_2 in alkaline minerals [17-26]. In such a process, CO_2 is sequestered by chemical reaction of CO_2 streams with light-metal oxides to form thermodynamically stable carbonates; thus enabling permanent and safe storage of CO_2 [10, 17, 19, 27-30]. While numerous studies have examined different alkaline waste streams to render cementation solutions – for example, coal combustion residues [18, 31-33], municipal incinerator wastes [29, 34], and wastes from iron and steel production [30, 35, 36] – the low production throughput, or severe operating conditions (i.e., high temperature and elevated CO_2 pressure) [5, 20, 28, 34] have made typical approaches difficult to implement at a practical scale [17].

On the other hand, concrete is a composite material that has relatively high thermal mass but low thermal resistance due to its high thermal conductivity [7, 37-39]. As a result, heat can easily flow into and out of buildings constructed by concrete envelopes subjected to changing outdoor air temperature [40, 41]. To maintain thermal comfort in buildings, space heating and air conditioning is constantly used in residential and commercial building operation, which consumes nearly 20%

of annual energy consumption in the United States [42]. Energy requirements for space heating and cooling in buildings are expected to increase with increasing demand for thermal comfort, especially in the context of climate change and global warming [43, 44]. Therefore, it is of great interest to develop novel building envelops that are able to reduce the energy required for heating and cooling and substantially improve building energy efficiency.

One strategy to minimize building loads involves using building envelope materials with thermal energy storage capacities. Thermal energy storage can be generally classified as sensible heat storage and latent heat storage according to the heat storage media [45-50]. As shown in Figure 1.1 [51], in sensible heat storage, heat is stored or released accompanied with temperature change of the storage media, whereas in the latent heat storage the heat is stored or released as heat of fusion/solidification during phase change processes of the storage media [46, 47, 52-57]. Phase change materials (PCM) transitioning between solid and liquid states near room temperature have been used to enhance the thermal storage capacity of traditional building materials [51, 57-64]. They store thermal energy in the form of latent heat when subjected to temperatures in excess of their melting point. Reversibly, PCM can release the thermal energy previously stored when the system temperature drops below their melting point. As such, using PCMs in the buildings can meet the demand for thermal comfort and energy conservation purpose, and great research interest is focused on the design and development of composite building materials integrated with PCMs [61, 65-71].
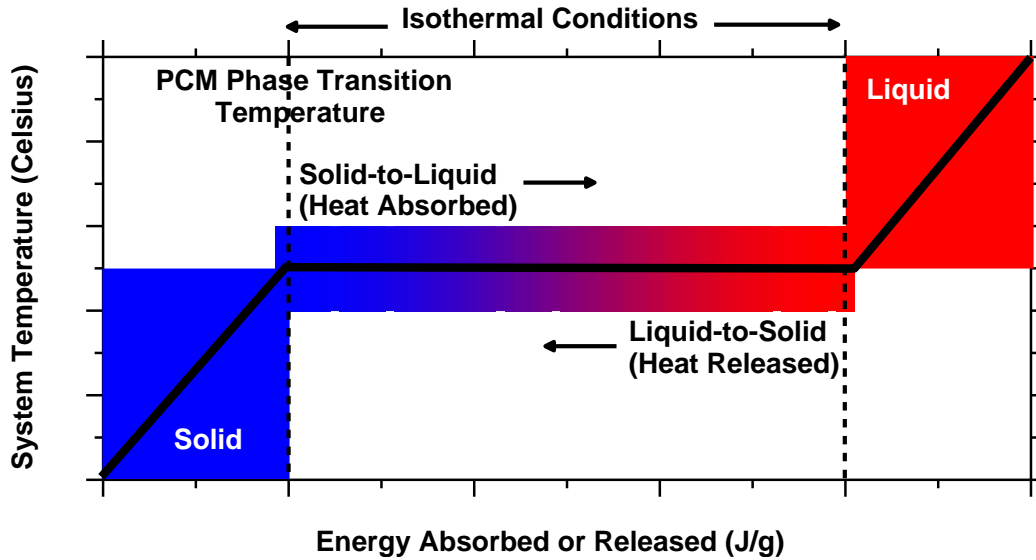
Figure 1.1: An illustration of the mechanism of PCMs in thermal energy storage [51]

Based on their components, PCMs can be divided into three groups: organic, inorganic, and eutectics. The most commonly known inorganic PCMs are hydrated salts [55, 56]. Inorganic PCM may have potential applications in some types of building elements because of their high volumetric heat storage capacity, good thermal conductivity, low cost, ready availability and non-flammable nature [56, 63]. However, they also show many unfavorable characteristics such as very high volume change and supercooling during solid-liquid transition, which is a problematic issue of inorganic PCMs because the liquid state can be cooled to below its freezing point whilst remaining a liquid which makes the associated phase change ineffective [63]. Another concern of the inorganic PCMs is their degradation and inoperative characteristic after repeated phase change cycles [72]. Eutectics are mixtures of two or more PCM and can be any combination of organic and inorganic constituents. Eutectics demonstrate several advantages such as sharp melting temperature and high volumetric thermal storage density, but there is a lack of currently available and reliable test data of thermo-physical properties of these materials, and their stability when used in a highly alkaline environment such as cement paste is still questionable [55]. These

4

disadvantages have led to the hydrated salts and eutectics not being considered as appropriate materials to be incorporated into building materials. Organic PCMs are mainly based on paraffin wax (hydrocarbons, which are a by-product of oil refining) and organic acids such as fatty acids [59, 73, 74]. Most of the organic PCMs are chemically stable, safe and non-reactive. Also, they have the ability to melt congruently without phase segregation and have self-nucleating properties that are compatible with traditional construction materials without any significant problems of supercooling [69, 75]. Organic PCMs are currently regarded as the most efficiently and commonly used type in building envelops as they have relatively large latent heat of fusion, and their phase change temperatures are often within the desired temperature range for building applications [51, 66, 70, 71, 76].

Methods of adding PCM into building materials generally fall into four categories: (i) direct incorporation, (ii) immersion, (iii) macroencapsulation, and (iv) microencapsulation [59]. Direct incorporation consists of adding PCM to supporting materials, such as wallboard or concrete, during the production process. The immersion method involves dipping a finished porous building material into melted PCM. Major drawbacks of these two methods include the lack of a barrier to protect the PCM against leakage during melting and against chemical reactions with the matrix material [56]. To address this issue, macroencapsulation of PCM in containers such as bags, tubes, or panels has been proposed before incorporating the encapsulated PCM into composite walls [60]. However, macroencapsulation suffers from a high temperature differential between the encapsulated PCM core and the boundary, which often leads to incomplete melting or solidification of the PCM [55, 56]. This can be addressed by containing PCM in microscopic capsules with thin walls and diameter ranging from 1 µm to 1 mm [71, 77]. The microencapsulated

PCM can easily be added to a building material such as concrete during production as long as the shell material is compatible with the supporting material [66, 76, 77]. A typical SEM morphology of microencapsulated PCMs is shown in Figure 1.2.

<div align="center">(a)   (b)</div>
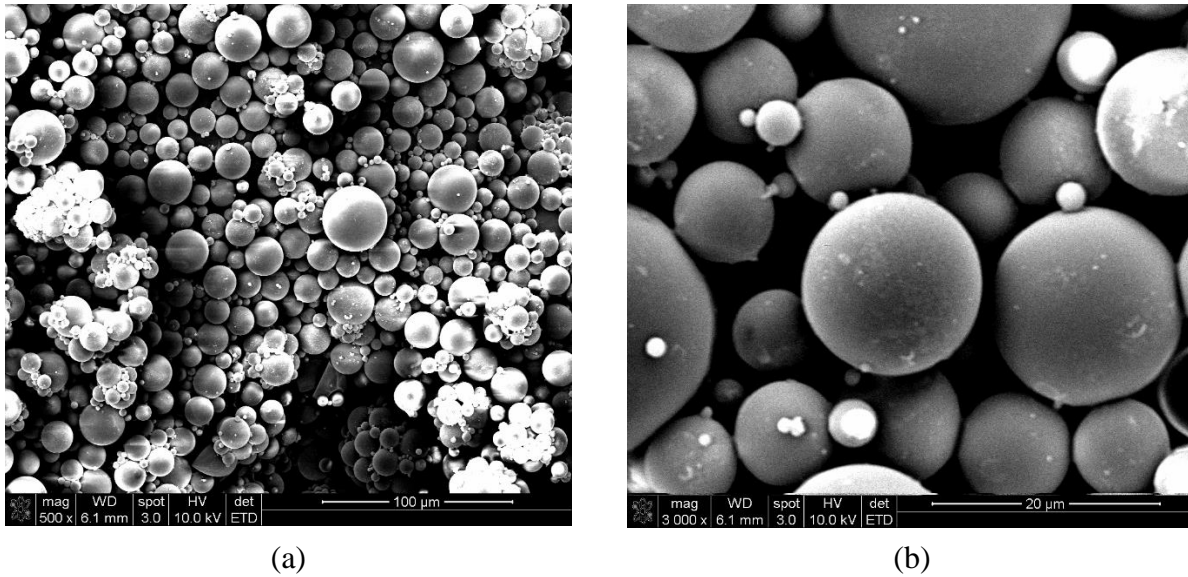
<div align="center">Figure 1.2: Typical SEM images of microencapsulated PCMs.</div>

Numerous studies have examined the ability of PCMs to reduce energy needs that are associated with heating/cooling buildings [57, 61, 65, 67, 70, 74, 78]. A smaller body of research has examined the ability of PCMs to mitigate early-age temperature rise in cementitious materials caused by exothermic cement hydration, and the resultant risk of thermal cracking [51, 78, 79]. In spite of extensive efforts, only a few studies have examined the durability of PCMs in the context of their chemical durability in alkaline cementitious environments [51, 74]. During hydration, cement particles dissolve, turning the pore solution into a caustic electrolyte [7, 80]. The pore solution contains alkalis, SO_4^{2-}, and Ca^{2+} species, presenting a pH typically greater than 13 [81]. When microencapsulated PCMs are embedded in such caustic systems, chemical reactions

between the pore solution and the capsule shell could result in damaging alterations, which could reduce the enthalpy of phase change [6, 80]. Thus, it is of great importance to investigate: (i) chemical durability of microencapsulated PCMs within cementitious environments, and (ii) the durability of the cementitious matrix containing PCM inclusions.

1.2 Objectives and scope

With the aforementioned considerations in mind, the overall goal of this dissertation is to elucidate how PCM addition in cementitious composites will affect the thermal energy storage capability and stability of microencapsulated PCMs, and how PCM addition will affect the durability of cementitious composites. This is of great significance as it provides an estimate of how long the thermal benefits of PCMs can last when they are embedded in cementitious environments. In addition, the feasibility of developing cement-free building material through carbonation of fly ash is investigated to explore sustainable alternative solutions for traditional cementation as required for building and infrastructure construction in the future. The specific objectives of this study are as follows:

- PCM survivability during fabrication of PCM-mortar composites with respect to damage and/or rupture of the PCM microcapsules that may occur during mechanical mixing, as well as chemical durability of PCM within cementitious matrices, and the potential interactions between the PCM and the pore-fluid that result in enthalpy alteration,

- Cementitious matrix durability, with emphasis on assessing how dosage of PCMs alters water absorption, drying shrinkage, and restrained shrinkage cracking behaviors of cementitious composites containing PCMs, and

- The feasibility of developing sustainable building material through clinkering-free

cementation by fly ash carbonation, with emphasis on the effects of CO_2 concentration and processing temperature on the progress of carbonation reaction, the development of microstructure, and the strength evolution of the material.

The dissertation is composed by 6 chapters, with the current chapter as an introduction explaining the motivations for the research work. Chapter 2 experimentally investigates how the dosage of microencapsulated PCMs influences the durability of cementitious materials. It is noted that while PCMs remain unaffected in alkaline solutions, they experience a significant enthalpy reduction, on the order of 25%, when exposed to sulfate-bearing environments. The mechanism of such enthalpy reduction has been identified as hydrolysis of the melamine-formaldehyde PCM capsule followed by its reaction with sulfate ions to form a melamine-sulfate supramolecular crystal. These reactions result in shell rupture following which the paraffinic PCM core contacts sulfate ions, resulting in enthalpy reduction. Analytical models have also been established based on experimental results to predict water absorption and drying shrinkage behaviors of cementitious composites containing microencapsulated PCMs.

Chapter 3 further explores the restrained shrinkage cracking behavior of cementitious composites containing microencapsulated PCMs, and reveals that the restrained shrinkage cracking behavior of cementitious composites is not a strength-controlled the addition of soft PCM inclusions does not alter the cracking sensitivity of the material. Rather, PCM addition extends the time to failure when cementitious composites are subjected to restrained shrinkage conditions.

Chapter 4 introduces a general method for retrieving deformation properties of microencapsulated PCMs or other particulate inclusions in cementitious composites. The effective thermal

deformation coefficient of cementitious composites with either microencapsulated PCM or quartz inclusions has been measured, which is used to retrieve the thermal deformation coefficients of the inclusions themselves. The thermal deformation coefficient of PCM microcapsules is estimated to be similar to that of the shell component due to partial filling of the microcapsules.

Chapter 5 has demonstrated an original means for clinkering free cementation by fly ash carbonation. Specifically, it is shown that Ca-rich fly ashes that host substantial quantities of Ca and Mg in the form of crystalline compounds, or in the glassy phases readily react with dilute concentrations of CO_2 in moist environments to produce cemented solids whose properties are sufficient for use in structural construction. Indeed, Ca-rich fly ash paste with water-to-solid ratio of 0.15 can take-up 9% CO_2 by mass of fly ash solids and achieve a compressive strength of 35 MPa following 7 days of exposure to CO_2 at 75 °C. The strength gain is linearly related to the extent of carbonation (CO_2 uptake). Detailed results from thermodynamic modeling, XRD analyses, and SEM observations suggest that fly ash carbonation results in the formation of a range of reaction products, namely calcite, hydrous silica, and potentially some C-S-H which collectively bond proximate particles into a cemented solid. Lastly, Chapter 6 summarizes the main contributions of this dissertation and presents recommendations for future work.

Chapter 2 Durability of cementitious composites containing microencapsulated PCMs

2.1 Background

The economic feasibility of employing cementitious composites containing microencapsulated PCMs (i.e., PCM-mortar composites) ultimately depends on their ability to reduce energy expenditure while embedded within a structural material [82]. That is, the PCM must retain its enthalpy of phase change during the service life of the PCM-mortar composite. This requires (i) physical durability of PCM capsules to prevent rupture during concrete mixing, (ii) form-stability of PCMs under diurnal thermal cycling (i.e., to prevent leakage over time) [50, 83, 84], and (iii) chemical stability of PCM microcapsules within the cement pore solution [85-87]. Additionally, the PCM microcapsules must not exhibit deleterious effects on the durability of mortar composites, which would reduce the service life of the material [88-90].

Many studies have demonstrated form-stability of microencapsulated PCMs following repeated heating-cooling cycles [91-100]. However, little attention has been paid to characterize the chemical stability of the PCMs upon embedment in cementitious environments [101-104]. During hydration, cement particles dissolve and release ions into the environment, turning the cement pore solution into a highly concentrated alkaline solution [7]. The pore solution is primarily composed of potassium and sulfate ions and saturated with calcium hydroxide ions, resulting in a pH in excess of 12.5 [80]. When microencapsulated PCMs are embedded in such caustic systems, chemical reactions between the pore solution and the polymeric microcapsule shell may potentially alter the

structure of the shell and lead to capsule rupture. This results in the release of the encapsulated paraffin and may reduce the phase change enthalpy of the composite due to loss and chemical degradation of paraffin in cementitious environment. Therefore, it is of great importance to investigate the extent to which exposure to caustic cementitious environments affects microencapsulated PCMs' thermal storage capability. To this end, the present study systematically investigates the stability of PCM phase change enthalpy following embedment within cementitious environments, focusing on the effects of mixing and immersion within alkaline and sulfate-containing solutions.

The durability of concrete subjected to aggressive environments depends largely on the water transport through the pore system [105-109]. Three mechanisms can be used to describe water transport in cementitious systems: permeability, diffusion, and absorption. Permeability is the measure of the flow of water under a pressure gradient, while diffusion is the transport of ions due to a concentration gradient [110]. Absorption can be described as the ability to take in water by means of capillary suction [111]. All three mechanisms are heavily influenced by the volume and connectivity of the concrete's porosity [112]. As a large fraction of concrete in service is only partly saturated, the initial ingress of water and dissolved salts is influenced by capillary absorption. As such, the rate of water absorption due to capillary suction is an important factor for quantifying the durability of cementitious systems [113-115]. The reverse process (i.e., drying) also affects the durability of the concrete, since the resulting stresses developed in restrained conditions result in drying shrinkage cracking, which allows further ingress of deleterious chemical species [116-119]. Aggregates influence the water absorption of cementitious composites by increasing the tortuosity of the porous network, and by reducing the volume fraction

11

of sorptive cement paste [120]. Drying shrinkage is influenced by these parameters as well, but is dominantly affected by the effective modulus of elasticity of the composite [121, 122]. While numerous studies have shown that the embedment of PCMs significantly decreases the mechanical properties (e.g., compressive strength, and modulus of elasticity) of cementitious composites [85, 86, 123], the influence of PCM inclusions on the water transport and durability of cementitious materials has been far less investigated.

This chapter investigates the durability of cementitious composites containing microencapsulated phase change materials (PCMs). First, the stability of the PCM's enthalpy of phase change was examined. A reduction of around 25% in the phase change enthalpy was observed, irrespective of PCM dosage and aging. Significantly, this reduction in enthalpy was not caused by mechanical damage that was induced during mixing, but rather by chemical interactions with dissolved SO_4^{2-} ions. Second, the influence of PCM additions on water absorption and drying shrinkage of PCM-mortar composites were examined. PCM microcapsules reduced the rate and extent of water sorption; the former was due to their non-sorptive nature which induces hindrances in moisture movement, and the latter was due to dilution, i.e., a reduction in the volume of sorptive cement paste. On the other hand, PCM inclusions did not influence the drying shrinkage of cementitious composites, due to their inability to restrain the shrinkage of the cement paste. The results suggest that PCMs exert no detrimental influences on, and, in specific cases, may even slightly improve the durability behavior of cementitious composites.

2.2 Materials and methods

2.2.1 Materials

Four different commercially available microencapsulated PCMs were used: MPCM6D, MPCM24D, MPCM43D (Microtek Laboratories) and Micronal DS 5008X (BASF Corporation). The relevant onset melting temperatures (indicative of Tpc) were 4.1 °C, 19.6 °C, 41.2 °C, and 22.8 °C, respectively, as measured by differential scanning calorimetry (DSC). The Microtek PCMs consisted of paraffin (alkane) cores that are encapsulated within melamine-formaldehyde (MF) shells, while the BASF PCM consisted of a paraffin/alkane core that was encapsulated within an acrylate polymer shell. In each case, variations in the phase change temperature are realized by altering the "chain length", i.e., the number of carbon atoms in an alkane of generic composition (C_nH_{2n+2}, where 'n' is the number of carbon atoms). The PCMs were received in the form of dry powders.

These four microencapsulated PCMs were selected for study since they encompass the range of phase change temperatures relevant for use in cementitious composites. Specifically, T_{pc} near 0 °C (e.g., MPCM6D) may be beneficial to mitigate freeze-thaw damage [124], T_{pc} close to room temperature (e.g., MPCM24D and Micronal DS 5008X) may be beneficial in reducing HVAC-related energy expenditures [37], and a higher T_{pc} (e.g., MPCM43D) may be used to mitigate early-age temperature rise caused by (exothermic) cement hydration. Each of the microencapsulated PCMs has been characterized in detail, e.g., in terms of: (i) their particle size distributions using static light scattering, (ii) their surface morphology using scanning electron microscopy (SEM), and (iii) their enthalpy of phase change using DSC; before and after immersion in alkaline solutions.

To more comprehensively assess chemical stability, MPCM24D was also immersed in sulfate-rich

solutions, and examined morphologically using SEM and for compositional changes using X-ray diffraction (XRD). Further, MPCM24D-mortar composites were examined in terms of both their drying shrinkage and water sorption behavior. Broadly, all other PCMs are expected to show similar behavior as MPCM24D based composites due to their similar shell/alkane-core compositions.

An ASTM C150 [125] compliant Type I/II ordinary Portland cement (OPC) was mixed with deionized (DI) water to prepare cement pastes and mortars in accordance with ASTM C192 [126]. The OPC had a nominal mass-based mineralogical composition of: 56.5% Ca_3SiO_5, 18.0% Ca_2SiO_4, 11.4% $Ca_4Al_2Fe_2O_{10}$, 6.3% $Ca_3Al_2O_6$, 4.6% $CaCO_3$, 1.2% $CaSO_4$, 1.1% $CaSO_4 \cdot 2H_2O$, 0.5% $CaSO_4 \cdot 0.5H_2O$, and 0.5% CaO. An ASTM C778 [127] compliant graded quartz sand (denoted as quartz hereafter) was used as a stiff, non-sorptive aggregate within the cement mortars.

Reference ("control") plain pastes with water-to-cement ratio (w/c, mass basis) of 0.35, 0.45, and 0.55 were prepared for water absorption measurements. For all other tests, cementitious mortars were prepared at a fixed w/c = 0.45 at various dosages of microencapsulated PCM and/or quartz inclusions. The inclusions were dosed as a percentage of the total composite volume at three levels (i.e., 10, 30 and 55 volume %). These mixtures are denoted by the volume percentage of the type of inclusion present preceded by "P" and/or "Q" corresponding to the PCM and quartz inclusions, respectively. To maintain workability (i.e., to enhance fluidity at high inclusion volume fractions), a commercially available water-reducing admixture (WRA; MasterGlenium 7500, BASF Corporation) was added. The WRA dosage for each mixture was as follows (% of cement mass):

P10 − 0.5%, P30 − 2.0%, P20+Q10 − 1.0%, P10+Q20 − 0.5%, P20+Q35 − 1.5%, P10 + Q45 − 1.0%, and Q55 − 0.5%. All other formulations contained no WRA.

2.2.2 Static Light Scattering

A Beckman Coulter Static Light Scattering (SLS) Particle Analyzer (LS13-320) was used to determine the particle size distributions (PSDs) of the OPC, PCM microcapsules, and graded quartz sand used in the specimen preparation, as presented in Figure 2.1. Each material was first dispersed into primary particles via ultrasonication in isopropanol that also served as the carrier fluid. The densities of OPC, quartz, Micronal DS 5008X and Microtek microencapsulated PCMs were taken as: 3150 kg/m3, 2650 kg/m3, 300 kg/m3, and 900 kg/m3, respectively. The complex refractive indices of the OPC, PCMs, and quartz were taken as $1.70 + i\,0.10$ [128], $1.53 + i\,0.00$ [129], and $1.54 + i\,0.00$ [130], respectively. The maximum uncertainty in the PSDs was about 6% based on 6 replicate measurements.
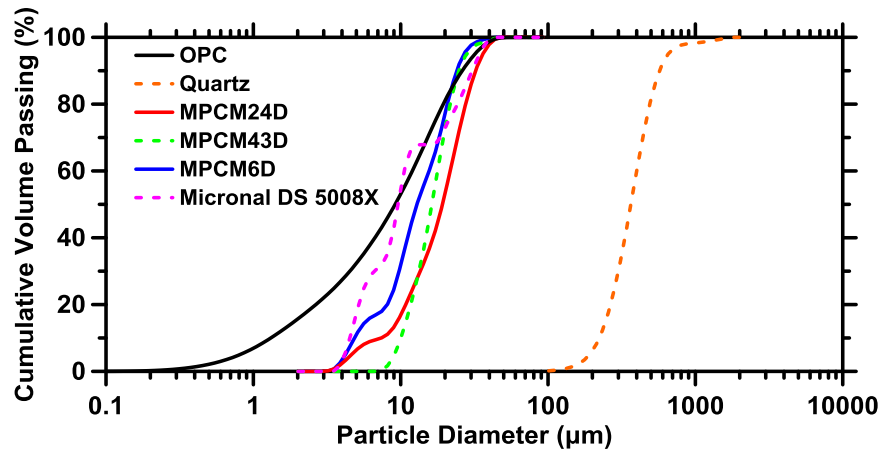
Figure 2.1 Particle size distributions of OPC, quartz, and the different microencapsulated PCMs measured using static light scattering (SLS).

2.2.3 Differential Scanning Calorimetry

The enthalpy of phase change (ΔH_{PC}), and the phase change temperature (TPC) of the PCMs was determined by differential scanning calorimetry (DSC 8500, Perkin Elmer). Prior to measurement, temperature and heat flow calibrations were performed using indium and zinc standards. Samples consisting of ≈10 mg of microencapsulated PCMs or PCM-mortar composites were placed in sealed aluminum pans and subjected to a temperature cycle ranging from -50-to-100 °C at a scan rate of 10 °C/min. The data reported is the average of three replicate specimens.

2.2.4 X-Ray Diffraction

Qualitative X-ray diffraction analysis was performed on PCM microcapsules before and after exposure to alkaline solutions. Samples were scanned from of 5-to-70° (2θ) using a Bruker-D8 Advance diffractometer in a θ-θ configuration with Cu-Kα radiation (λ=1.54 Å) and a VANTEC-1 detector. The diffractometer was run in continuous mode with an integrated step scan of 0.021° (2θ). A fixed divergence slit of 1.00° was used during X-ray data acquisition.

2.2.5 Scanning Electron Microscopy

SEM observations were performed on pristine PCMs and on PCM capsules before and after immersion in alkaline solutions for 6 hours. The microencapsulated PCMs were deposited on carbon adhesive and then gold-coated. Secondary electron (SE) images were obtained with an accelerating voltage of 10 kV and a beam current of 80 pA using an FEI Nova NanoSEM 230.

2.2.6 Water Absorption

A modified ASTM C1585 [113] procedure was used to characterize the rate and extent of water

sorption in PCM-mortar composites. Cylindrical specimens (d x h, 10 cm x 20 cm) were cast, then cured for 28 days in saturated limewater before being cut into 10 cm x 3.75 cm sections using a diamond-tipped masonry saw. The cylindrical slices were conditioned at 50 °C in a desiccator at relative humidity (RH) of 80% established using a saturated KBr solution for 3 days. Thereafter, each sample was stored in a sealed container for another 15 days to allow moisture redistribution. The sides and one face of the cylinder were sealed with aluminum tape, leaving only one open face exposed to water at 23 °C. The mass of water absorbed through this face was recorded over a time period of 8 days using a laboratory balance (ML1502E, Mettler Toledo) with a precision of $\pm\,0.01$ g. The data reported is the average of three replicate specimens prepared from the same mixing batch.

2.2.7 Drying Shrinkage

Unrestrained drying deformations of cementitious specimens were measured as per ASTM C157 [131]. Cement pastes and mortars were cast in prismatic molds (2.5 cm x 2.5 cm x 28.5 cm, w x h x l), cured for 24 hours above water in a sealed container, prior to curing in saturated limewater until an age of 28 days. The specimens were subsequently dried, sealed on two sides with aluminum tape to ensure 1D moisture diffusion, and stored at 25.0 ± 0.2 °C and $50.0 \pm 0.2\%$ RH in an environmental chamber (KB024-DA, Darwin Chambers Company). Changes in the prismatic samples' lengths were recorded at 1, 3, 7, 14, 28, 56, and 90 days from the start of the drying period. The data reported is the average of four replicate specimens prepared from the same mixing batch.

2.3 Results and discussion

2.3.1 Stability of PCMs' phase change enthalpy in cementitious environments

Figure 2.2 displays DSC heat flow curves showing the melting and solidification behavior of aforementioned four pristine microcapsules. The curves show small peaks attributed to impurities blended into the paraffin (the active PCM ingredient) to control its phase change temperature [56]. The peak temperature during the melting (heating) process was about 27.8 °C, while the peak temperature during the solidification (cooling) was about 16.6 °C for MPCM24D. The difference between observed peak temperatures for melting and solidification is indicative of supercooling, which is common in microencapsulated PCMs, due to the lack of heterogeneous nucleation sites for solidification to initiate within the microcapsules [71]. The enthalpies of phase change were 169.2 kJ/kg, 161.2 kJ/kg, 204.9 kJ/kg, and 136.6 kJ/kg for pristine MPCM6D, MPCM24D, MPCM43D, and Micronal DS 5008X, respectively. The data reported is the average of three replicates.

Figure 2.3(a) shows DSC heating curves for cement mortar specimens containing 0, 10, 20 and 30 volume % MPCM24D in the mixture. The temperature corresponding to the onset (24 ± 1°C) of phase change, and the temperature at the peak (27 ± 1°C) were similar regardless of the PCM dosage. No peaks were observed in the DSC curve of the plain cement paste, as expected. It is worth pointing out that the cooling curves show behavior similar to that of the heating curves, and the enthalpy of solidification is equal and opposite to that corresponding to melting. The microencapsulated PCM mass fraction in the composite dictates its "expected" phase change enthalpy ΔH_{calc} (in kJ/kg) expressed as,

$$\Delta H_{calc} = \frac{m_P h_{sf,P}}{m_P + m_m} \qquad\qquad \text{Eq. (2.1)}$$

where, $h_{sf,P}$ is the measured latent heat of fusion of the core-shell PCM microcapsules (e.g., 161.2 kJ/kg for MPCM24D), while m_P and m_m are the masses of core-shell PCM microcapsules and the cement paste in the composite, respectively. Figure 2.3(b) shows the correlation between the measured phase change enthalpy of PCM-containing cementitious composites, ΔH_{exp}, and that calculated using Equation (2.1), ΔH_{calc}. A linear relation is noted between ΔH_{exp} and ΔH_{calc}, but with a slope of 0.75. As such, the incorporation of PCM microcapsules within the cementitious paste results in a 25% enthalpy reduction, which was observed to be independent of both the PCM dosage and the age of the cementitious composite. A similar enthalpy reduction was observed previously when Micronal DS 5008X PCM microcapsules were added to cement pastes [51].

PCM capsule survivability during mechanical mixing: Mechanical mixing of the PCM-mortar composites, and the potential damage it causes to the PCM microcapsules, was investigated as the cause of the enthalpy reduction observed in Figure 2.3(b). As a comparison to PCM mortars that were fabricated by mixing the cement, microencapsulated PCM, and water in a planetary action mixer as per ASTM C305 [132], an additional set of PCM-mortar composites was created within a DSC pan (φ = 5 mm) by gently sprinkling onto an underlying paste layer, PCM particles, and then covering these particles with additional cement paste, forming a "sandwich", after which the pan was crimped shut.
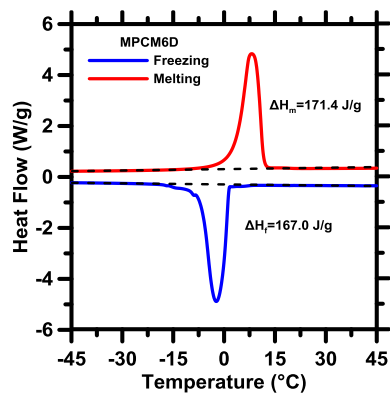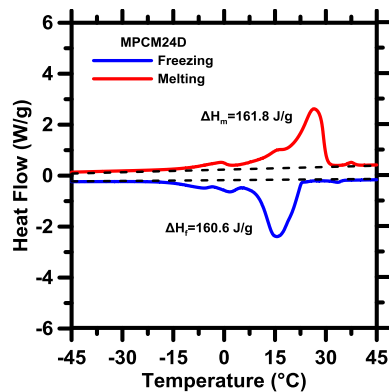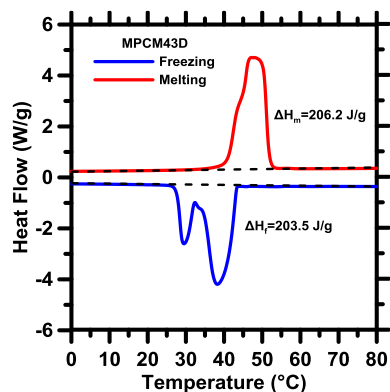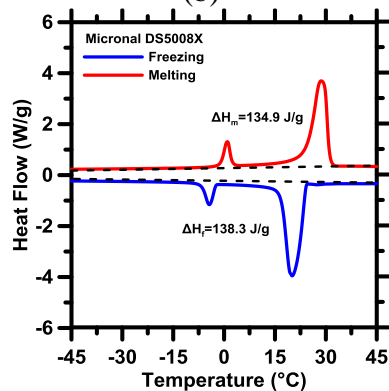
Figure 2.2: Representative DSC curves illustrating the enthalpies of phase change for pristine: (a) MPCM6D, (b) MPCM24D, (c) MPCM43D, and (d) Micronal DS5008X. The average of freezing and melting enthalpies denotes the "phase change enthalpy" noted herein.

20

(a)   (b)
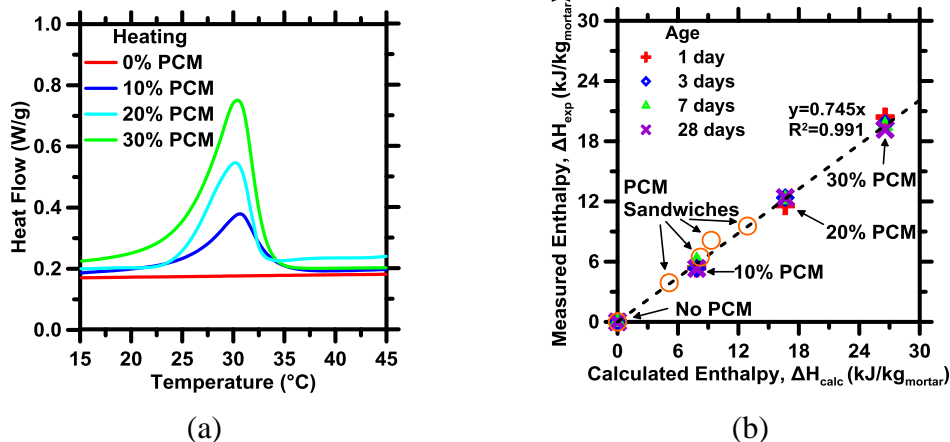
Figure 2.3: (a) Representative DSC curves for a PCM-mortar composites (w/c = 0.45) containing different volume fractions of MPCM24D. For clarity, only the endothermic (melting) peaks are shown, as the enthalpy of phase change measured during solidification is similar to that observed during melting. (b) The measured enthalpy of phase change for PCM-mortar composites (w/c = 0.45) as a function of the enthalpy that is expected based on the mass dosage of PCM in the composite (Equation 2.1). Even when mechanical mixing is avoided (e.g., see data for PCM "sandwiches"), an enthalpy reduction is noted, indicating that mixing and mechanical damage caused to the PCM capsules is not the cause of enthalpy reduction.

The resulting PCM sandwich specimens were cured for 3 days in a sealed condition prior to DSC characterization. This preparation procedure was used to avoid any damage that may be induced on the PCM microcapsules due to shear and frictional forces that may develop during mechanical mixing. As such, this procedure enables discrimination of the effects of mechanical mixing from those associated with the nature of the chemical environment. Figure 2.3(b) reveals the measured enthalpy of phase change of these PCM sandwich composites falls on the same trend line as those

subjected to mechanical mixing, indicating that mechanical mixing is not the cause of the observed enthalpy reduction. As such, this clarifies that a chemical rather than mechanical cause is at the origin of the enthalpy reduction observed in PCM containing cementitious composites.
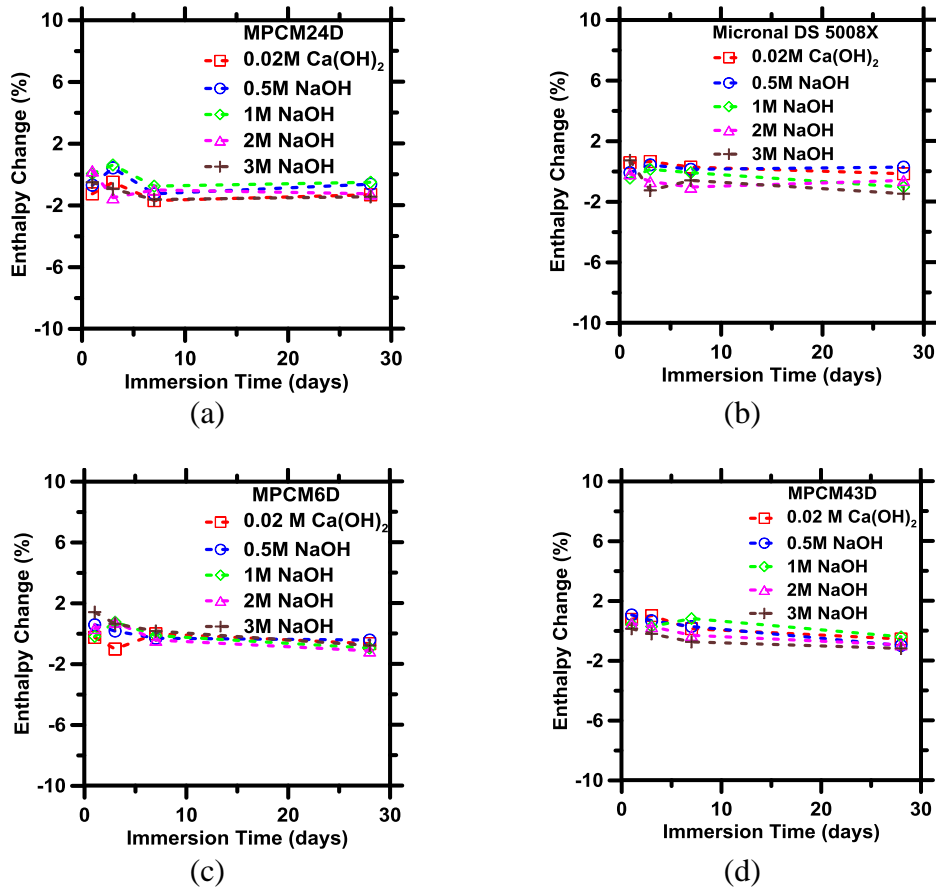
Figure 2.4: The relative change in the enthalpy of phase change for (a) MPCM24D, (b) Micronal DS 5008X, (c) MPCM6D, and (d) MPCM43D following immersion in alkaline (similar to pore fluid) solutions for 28 days. The highest uncertainty in each measured data point is on the order of ±1%.

22
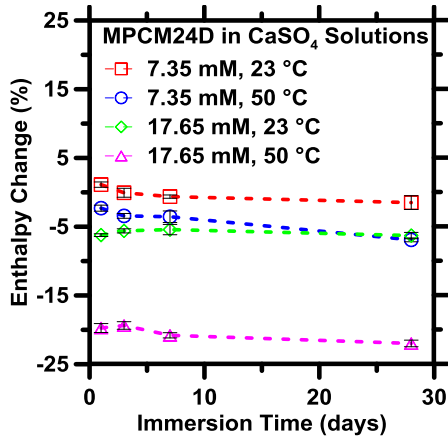
(a)
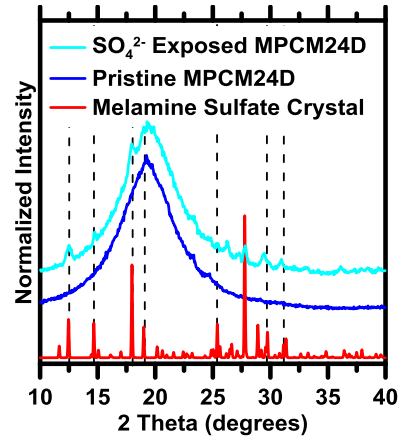
(b)
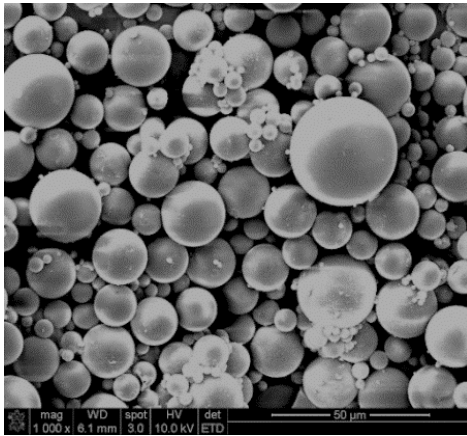
(c)
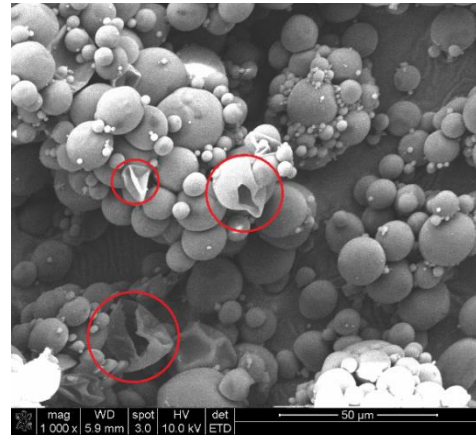
(d)

Figure 2.5: (a) The change in the phase change enthalpy of MPCM24D following immersion in gypsum solutions. (b) The XRD patterns of the MS supramolecular structure and of MPCM24D before and after immersion in saturated gypsum solutions for 28 days. SEM images of the MPCM24D microcapsules: (c) before exposure, and, (d) after 3 days exposure to saturated calcium sulfate solution at 50 °C, wherein ruptured capsules are highlighted by the red circular traces.

2.3.2 Chemical stability of PCM within model cementitious environments

To evaluate the chemical stability of microencapsulated PCMs in alkaline conditions similar to cement pore solutions, PCM microcapsules were immersed in solutions of the following

23

compositions: 0.02 M Ca(OH)$_2$, 0.5 M NaOH, 1 M NaOH, 2 M NaOH, and 3 M NaOH. Following 1, 3, 7, and 28 days of immersion, the enthalpy of phase change and the onset temperature of phase change of the PCM microcapsules were characterized via DSC.

Figure 2.4 shows the change in the enthalpy of phase change of four types of microcapsules as a function of immersion time, relative to that in their pristine condition. Over 28 days of immersion, the enthalpy of phase change of the microencapsulated PCMs decreased by $\leq 2\%$. This suggests that the PCM capsule is sufficiently stable in alkaline environments. These results were consistent across PCMs of various transition temperatures. While these results indicate that negligible enthalpy reduction occurred in alkaline solutions, regardless of the associated cation, these simplified solutions did not contain the diversity of potentially deleterious ions present in the cement pore solution. For example, gypsum (hydrated calcium sulfate, CaSO$_4$·H$_2$O) is commonly added to OPC to control the setting time. In this case, sulfate ions in the pore solution of cement paste may play an important role in deteriorating the PCM microcapsules' shell material, which requires further examination [7]. It should be noted that cement pore solution achieves gypsum saturation within the first few hours, and the concentration of sulfate ions progressively decreases in time [7].

Figure 2.5(a) shows the relative change in enthalpy of phase change for MPCM24D microcapsules exposed to CaSO$_4$·H$_2$O (gypsum) solutions having concentrations of 7.35 mM, and 17.65 mM, for up to 28 days at 23 °C and 50 °C. The higher concentration, 17.65 mM corresponds to the solubility limit of gypsum in water at 23 °C. Also, while the lower temperature corresponds to ambient conditions, the higher temperature (50 °C) corresponds to that which may be achieved in modestly

sized concrete sections due to the effects of self-insulation and the exothermic nature of cement + water reactions.

An immediate decrease in the PCM's enthalpy of phase change was observed (i.e., in ≤ 24 hours) upon immersion in sulfate solutions, especially at slightly elevated temperature. For example, the enthalpy reduction of MPCM24D immersed in saturated calcium sulfate solution at 50 °C after 28 days was around 23%. These findings suggested that sulfate ions play a significant role in inducing the observed 25% enthalpy reduction following embedment of PCM in cementitious composites (e.g., see Figure 2.3(b)). This is attributed to the fact that the shell material of the microencapsulated PCMs was a melamine-formaldehyde (MF) resin that is synthesized by crosslinking melamine with formaldehyde under alkaline conditions. Since the crosslinking reactions are reversible, the crosslinks in MF's structure may breakdown in aqueous environments [133]. Following reversible breakdown, melamine co-crystallizes with sulfate ions to form a melamine-sulfate (MS)-like supramolecular structure of molecular formula: $[(C_3H_7N_6^+)_2(SO_4^{2-})]\cdot 2H_2O$ [134]. It is worth pointing out that the observed PCM enthalpy reduction occurred immediately after exposure to sulfate ions – but after this initial reduction, no further change in the enthalpy of phase change was observed.

Figure 2.5(b) shows XRD of MPCM24D samples before and following their immersion in saturated gypsum solutions for 28 days, and those for the melamine-sulfate (MS) supramolecular structure [134]. The X-ray patterns confirm the presence of supramolecular crystal compounds following immersion of PCM microcapsules in a saturated sulfate solution. It is postulated that hydrolysis of the MF crosslinks occurs within the shell of PCM microcapsules exposed to sulfate

25

solutions. This process releases melamine, which then reacts with sulfate ions in solution to form the MS supramolecule with a 3D microporous structure that is linked by intermolecular hydrogen-bonds and aromatic π-π interactions [134]. These reactions deform and degrade the PCM's shell causing its rupture; after which the paraffinic core contacts the alkaline cementitious pore-fluid. This is confirmed by the SEM images presented in Figures 2.5(c-d) which show capsule rupture following exposure to gypsum solutions. The reduction in the enthalpy of phase change is thus attributed to the contact of the PCM core material with the high pH cementitious environment. To confirm this hypothesis, the paraffinic core material of MPCM24D was directly dispersed into gypsum solutions and stirred at 50 °C over a 28-day exposure period. Before exposure, the enthalpy of phase change of MPCM24D's core material was 199.8 kJ/kg; which indicated that following its encapsulation, the core accounted for 81 mass % of the MPCM24D microcapsules. Upon exposure to saturated gypsum solutions, the enthalpy of phase change of the core material decreased to 166.1 kJ/kg, a 17% reduction. Since the MF shell has no latent heat capacity, and the enthalpy reduction of MPCM24D immersed in at 50 °C after 28 days was ≈ 23% (e.g., see Figure 2.5a), it was estimated that around 30% of the core material has been released (degraded) from the capsules. These results indicate that chemical reactions between the PCM core and SO42- are primarily responsible for the observed enthalpy reduction (Figure 2.3b). This pathway of the PCM's enthalpy reduction resulting from chemical interactions is summarized in Figure 2.6.

MF: Melamine-Formaldehyde   M: Melamine   S: Sulfate   MS: Melamine Sulfate
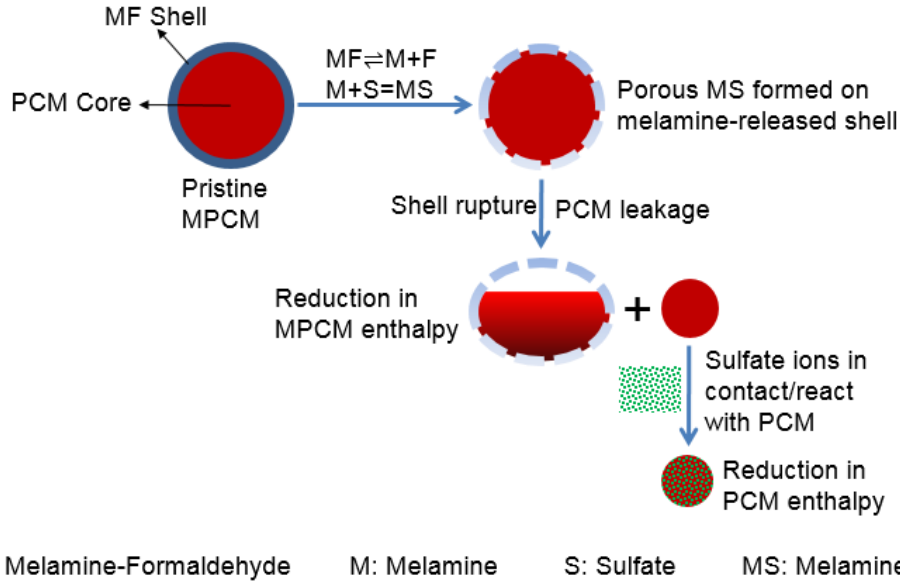
Figure 2.6: The proposed chemical interaction pathway which results in enthalpy reduction (reduction) of the PCMs following exposure to caustic solutions containing sulfate ions.

2.3.3 Moisture transport behavior of PCM-containing cementitious composites

The water absorption response of PCM-mortars was quantified as per ASTM C1585. This involved measuring incremental mass change (increase) of the samples after 1 min, 5 min, 10 min, 20 min, 30 min, 60 min, 120 min, 180 min, 240 min, 300 min, 360 min, and then every day for up to 8 days following their contact with water. The origin of time was taken at the moment when the specimen was first placed in contact with water. The cumulative volume of absorbed water per unit area of inflow surface I (in mm), was calculated as,

$$I = \frac{\Delta m_t}{\rho_w A} \qquad \text{Eq. (2.2)}$$

where Δm_t (g) is the cumulative change in specimen mass at time t (seconds), A (mm^2) is the area of the specimen exposed to water, and ρ_w is the density of water (0.001 g/mm^3 at 23 °C). As per

Hall [135], single-phase flow by capillary sorption in an unsaturated porous media can be expressed in the form of a diffusion equation – thus, from theory, I scales to $t^{1/2}$. But, in practice a finite positive intercept, k (mm), is noted as a result of the filling of surface porosity on the inflow surface [135]. As such, the sorptivity S can be determined from the slope of the best-fit line [136],

$$I = k + St^{1/2}$$
Eq. (2.3)

where S is the sorptivity of the material, i.e., the rate of absorption (in mm/h$^{1/2}$) and t is the time (in h). As per ASTM C1585, Equation (2.3) was fitted to the measured absorption data $I(t)$ within the first 6 hours, and between 1 and 8 days, to calculate the initial sorptivity (S_1, in mm/h$^{1/2}$) and secondary sorptivity (S_2, in mm/h$^{1/2}$), respectively.

Figure 2.7(a) shows representative water absorption data for a plain cement paste (w/c = 0.45) [135]. Neithalath [137] proposed that water sorption data can be described by a combination of an exponential term for sorption and a solution of Fick's second law for diffusion to predict time-dependent moisture ingress such that,

$$I = \frac{\Delta m_t}{\rho_w A} = B\left[1 - \exp\left(\frac{-S_1 t^{1/2}}{B}\right)\right] + \frac{C_0 L}{\rho_w}\left\{1 - \sum_{n=0}^{\infty}\frac{8}{(2n+1)^2 \pi^2}\exp\left[\frac{-D_m(2n+1)^2 \pi^2 t}{4L^2}\right]\right\}$$
Eq. (2.4)

where B describes the penetration depth when capillary pores dominate initial sorption (mm), C_0 is the concentration of moisture at the specimen's surface (kg/m^3), D_m is the moisture diffusion coefficient (m^2/h), and L is the length of the specimen (m). Experimental data of I estimated using Equation (2), and S_1 obtained via Equation (2.3) were used to fit Equation (2.4), thus revealing the constants B, C_0, and D_m. Figure 2.7(b) displays a representative fit of the Equation (2.4) for the plain paste (w/c = 0.45) including the separated contributions of capillary sorption and of diffusion, respectively. As expected, the contribution of capillary sorption to moisture intake was dominant

28

at early times, and vanished over time, while the diffusion term represented long-term moisture transport involving the smaller gel pores [138]. The fitting of Equation (2.4) to the experimental water intake of the cement mortars (for w/c = 0.45) containing various dosages of PCM's and/or quartz inclusions were determined, as shown in Figure 2.8. Note that, based on Equation (2.4), after an infinite amount of time, the cumulative water absorbed in the specimen is equal to $B+C_0L/\rho_w$.
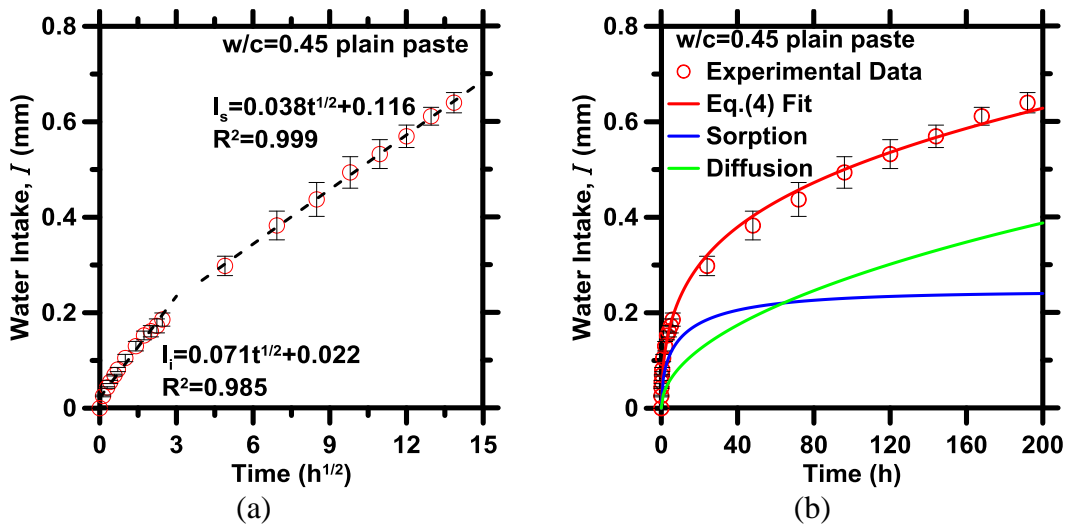
Figure 2.7: (a) Water sorption as a function of the square root of time ($h^{1/2}$) for a plain cement (w/c = 0.45), and (b) Representative fits of the sorption-diffusion equation (Eq. 2.4) to the plain cement paste's water sorption response.
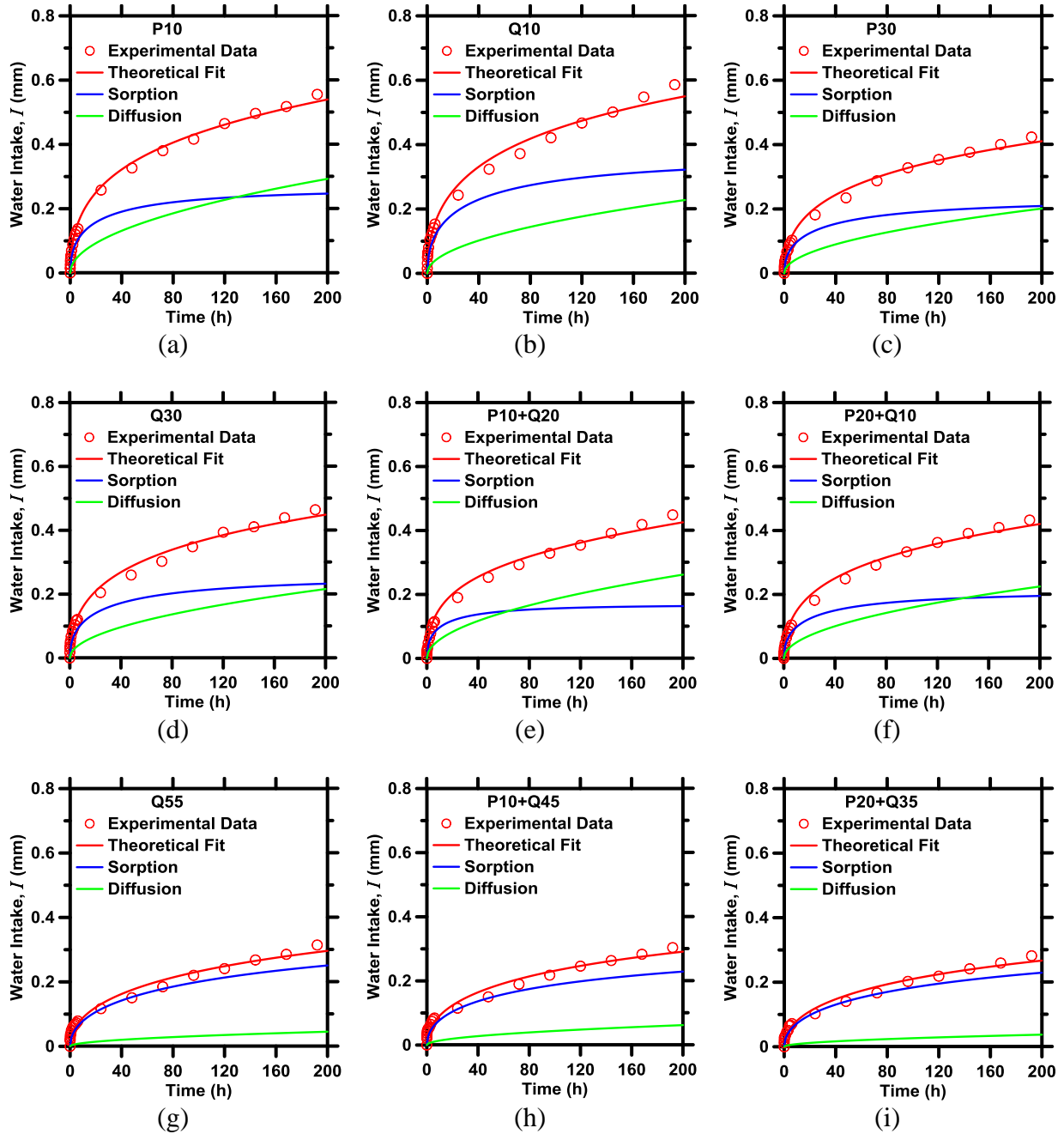
Figure 2.8: Fits of the sorption-diffusion equation (Equation 2.4) to experimental water sorption data of cement mortars containing various dosages of microencapsulated PCM and/or quartz inclusions. The highest uncertainty in each measured data point is on the order of ± 0.04 mm.

Figure 2.9(a) displays the initial S_1 and secondary S_2 sorptivities measured for all mixtures (for

w/c = 0.45) as functions of inclusion volume fraction ϕ_{P+Q}. It is noted that regardless of the nature

of inclusions present (i.e., PCM or quartz), both initial S_1 and secondary S_2 sorptivities decreased

linearly with increasing total inclusion volume fraction. This is because both quartz and PCM serve

as non-sorptive inclusions [120]. As the volume fraction of non-sorptive inclusions increases,

capillary flow is redirected around inclusion particles, increasing the tortuosity of the transport

path. As a result, moisture penetration rates diminish. Further, the initial sorptivity decreased faster

than the secondary sorptivity, indicating a greater relative importance of diffusive moisture

transport with increasing inclusion dosage. In addition, the effective moisture diffusion coefficient

D_m (Figure 2.9b) decreased systematically with inclusion dosage since both PCM and quartz were

non-porous inclusions, far less permeable than the cement paste. In turn, the total amount of water

absorbed by the composites diminished with inclusion dosage due to the dilution of the content of

porous cement paste, which is the main water-sorbing component in the composite (see Figure

2.9c).

(a)   (b)   (c)
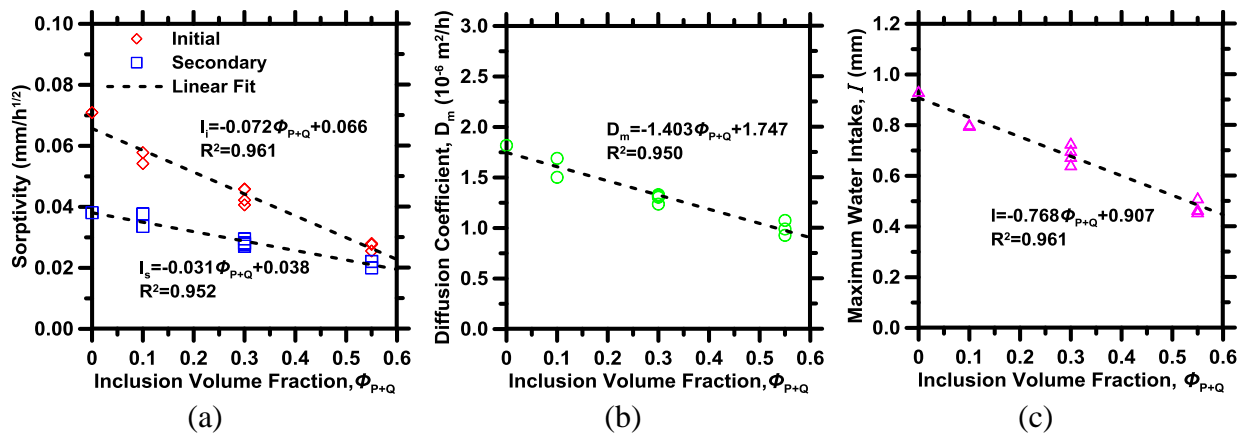
Figure 2.9: (a) Water sorptivity, (b) Moisture diffusion coefficients of cementitious composites

containing PCM and/or quartz inclusions, and (c) The cumulative amount of water absorbed by

cementitious composites containing PCM and/or quartz inclusions after infinite time.

31
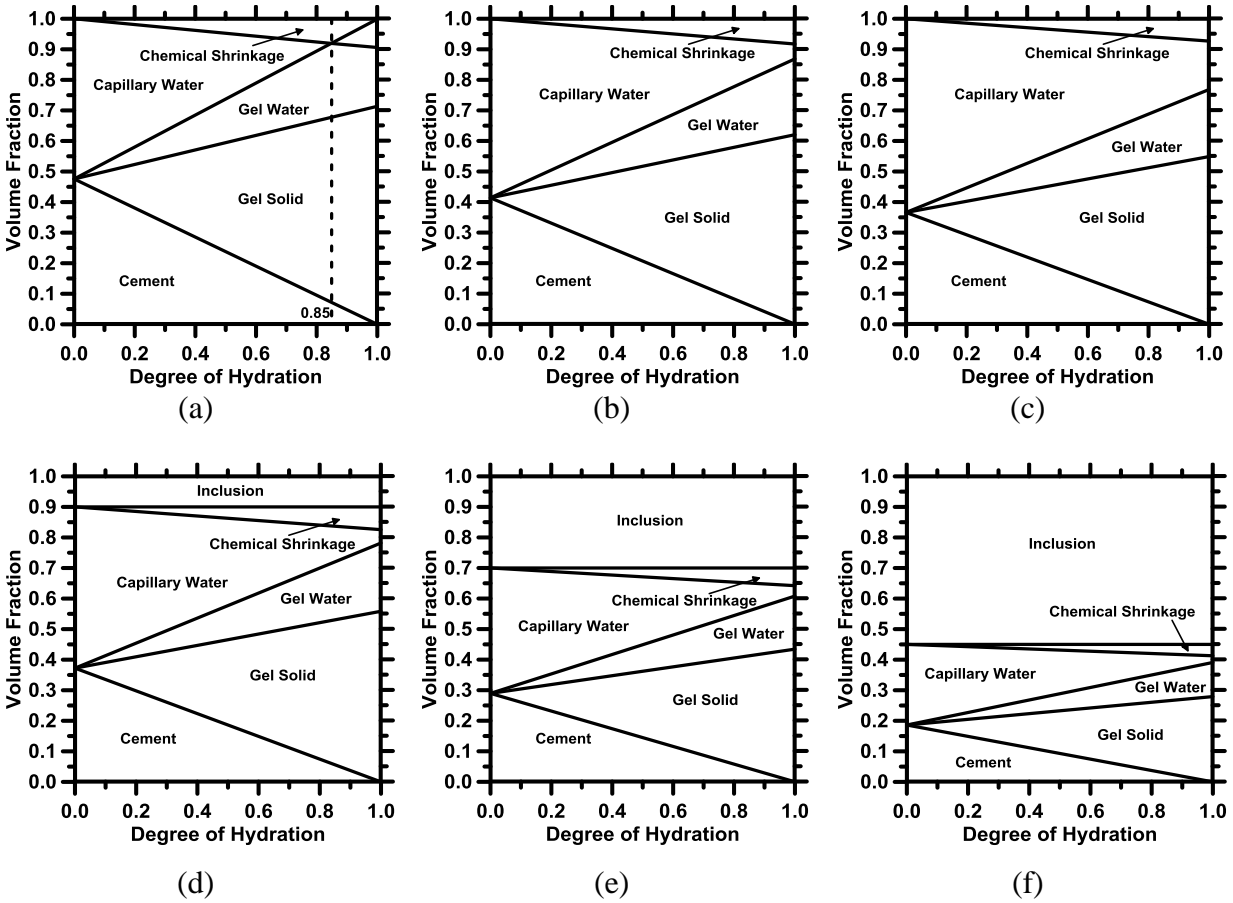
Figure 2.10: Powers model showing phase distributions for (a) plain paste with w/c=0.35, (b) plain paste with w/c=0.45, (c) plain paste with w/c=0.55, (d) w/c=0.45 cementitious composite containing 10% inclusions, (e) w/c=0.45 cementitious composite containing 30% inclusions, (f) w/c=0.45 cementitious composite containing 55% inclusions

As water absorption appeared relatively insensitive to the type of inclusion, a model was sought to capture both the effects of *w/c* and inclusion volume (i.e., reduction in paste content) on water absorption. Simply, water absorption depends on the unsaturated and interconnected porosity of the system, i.e., the volume available to be filled with water. The total porosity, composed of capillary porosity (V_{cw}), the gel porosity (V_{gw}), and chemical shrinkage (V_{cs}) in a cement paste can be determined by Powers' model which estimates the volume relationships among constituents

32

and porosity of the mixtures during the hydration process [114, 139] at a given degree of cement reaction, here taken to be 80% after 28 days [140]. The calculated phase distributions for cementitious composites with different w/c and volume fractions of inclusions as a function of degree of hydration are shown in Figure 2.10.

Since both PCM and quartz were non-sorptive and non-reactive inclusions, and assuming that no volume expansion occurs during wetting, the total porosity of the mixture can be calculated as a function of w/c, degree of reaction (α, unitless), and the inclusion dosage. Indeed, isothermal calorimetry has indicated that PCM microcapsules and quartz inclusions exert no appreciable effect on the degree of hydration [51]. As such, Figure 2.11 shows the maximum long-term water uptake of a range of cementitious composites (i.e., both with, and without inclusions) as a function of their total porosity calculated by Powers model. Across all compositions, an empirical logarithmic expression described the relationship between the maximum water uptake I_{max} and the total porosity V_{tot} (i.e., the sum of the capillary and gel pores, and void spaces created by chemical shrinkage):

$$I_{max} = 0.50 \ln V_{tot} + 1.36$$
<div align="right">Eq. (2.5)</div>
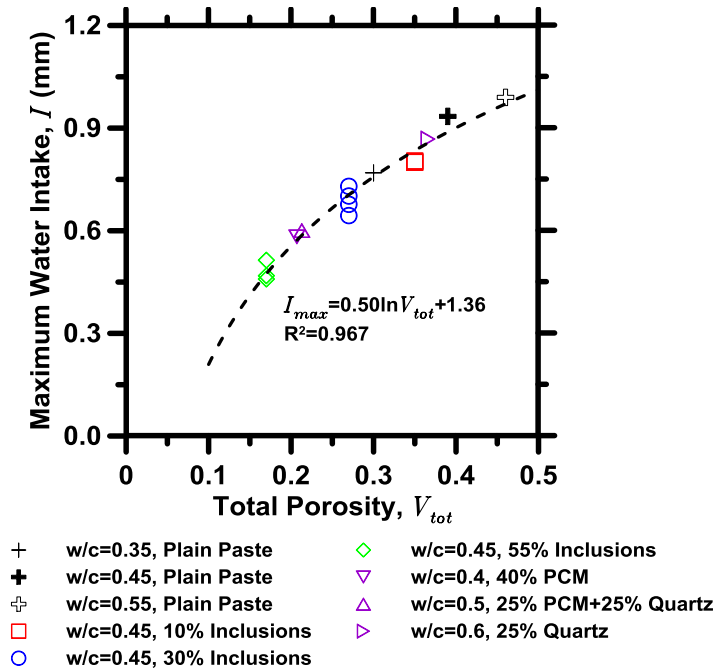
Figure 2. 11: The maximum water intake at infinite time (I_{max}) as a function of total porosity, V_{tot} calculated using Powers model.

To ascertain the predictive power of this approach, water sorption experiments were carried out on three additional mixtures having different w/c and volume fractions of PCM and quartz: (i) w/c = 0.40 mortar containing 40 volume % PCM, (ii) w/c = 0.50 mortar containing 25 volume % PCM and 25 volume % quartz, and (iii) w/c = 0.60 mortar containing 25 volume % quartz. The empirical expression shown in Equation (2.5) was able to robustly capture the terminal amount of water absorbed by these mixtures, simply from knowledge of the mixture proportions, and the degree of reaction (see Figure 2.11). It should be noted that Equation (2.5) accounts for differences in porosity (volume fraction) based only on the initial w/c of the cement paste. The addition of non-sorptive inclusions dilutes the volume fraction of the porous cement paste, thereby reducing the volume of porosity in the cementitious composite. Therefore, the present expression only accounts for the effects of non-sorptive (or negligibly sorptive) inclusions. While Equation (2.5) could

indeed be modified to represent the effects of porous aggregates, i.e., by taking aggregate porosity into account in the porosity volume fraction parameter V_{tot} – this approach was not implemented here. As such, it is possible to estimate terminal water sorption from the porosity of the material. Of course, the results indicate that PCMs diminish water sorption similar to other non-porous inclusions, an effect that is caused on account of dilution of the cement paste content.

2.3.4 Unrestrained drying shrinkage of cementitious composites containing PCMs

Figure 2.12 shows the drying shrinkage strain (S, µε) of cementitious composites containing PCM and/or quartz inclusions as a function of time, with a fixed w/c = 0.45. For both quartz mortars and mixed mortars (i.e., those containing both quartz and PCM inclusions), increasing the quartz volume fraction reduced drying shrinkage, since stiff inclusions restrain the shrinkage of the paste [51]. The dosage of microencapsulated PCM inclusions resulted in no change in shrinkage, *vis-à-vis* the plain cement paste. This is because the soft PCM inclusions, due to their compliant nature, are unable to restrain the shrinkage of the cement paste upon drying. This is supported by the observation that, when PCM and quartz inclusions were dosed together, the measured shrinkage response was equal to that expected for a mixture containing only quartz inclusions.
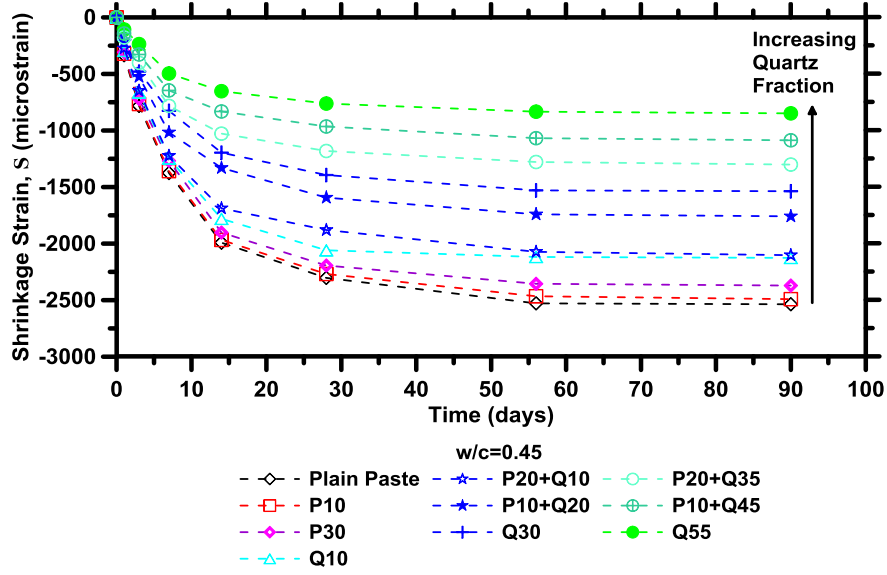
Figure 2.12: Shrinkage plotted against the drying time for samples containing different volume fractions of PCM and/or quartz.

To better understand the trends in shrinkage, and the influence of the inclusion properties, the model of Hobbs developed for two-component composites (i.e., matrix + inclusion) was applied to predict the shrinkage of the composite [122, 141]. This model is expressed as,

$$S_{m+i} = S_m - \frac{2K_i(S_m - S_i)\phi_i}{K_i + K_m + (K_i - K_m)\phi_i} \quad \text{with} \quad K_j = \frac{E_j}{3(1 - 2\upsilon_j)} \qquad \text{Eq. (2.6)}$$

where S_j, K_j, E_j, and υ_j are the shrinkage strain, bulk modulus, modulus of elasticity, and Poisson's ratio of component j of volume fraction ϕ_j, respectively. Here, the subscripts $m+i$, m, and i refer to the two-component composite, the matrix (cement paste), and the inclusions (PCM or quartz), respectively. The shrinkage of PCM microcapsules was assumed to be near-equivalent to that of the cement paste, and quartz was assumed to be non-shrinking, Therefore the shrinkage ratio of quartz and PCM inclusions in relation to cement paste are taken as: $S_Q/S_m = 0.01$ and $S_P/S_m = 0.99$. The bulk modulus of the cement paste was calculated: (i) from measured data of its modulus of

36

elasticity E_m = 9.58 GPa, 13.48 GPa, 15.65 GPa, and 16.75 GPa [123] at ages of 1, 3, 7, and 28 days, respectively and (ii) assuming its Poisson's ratio to be v_m = 0.2 [142]. The modulus of elasticity and Poisson's ratio of the microencapsulated PCM and quartz inclusions were estimated based on literature data as: E_P = 0.0557 GPa, v_P = 0.499 [143], and E_Q = 72 GPa, v_Q = 0.22 [144], respectively. The Hobbs model assumes the following: (i) the cementitious composites consist of only two phases (i.e., inclusion particles dispersed in a continuous cement paste matrix), (ii) the inclusions and cement paste matrix are elastic, and (iii) the elastic properties of the components do not change with shrinkage.

For three-component systems (i.e., PCM microcapsules + quartz + cement paste), a two-step approach was applied to calculate the shrinkage strain via the Hobbs model. In this approach, the PCM and cement paste were treated as a homogeneous matrix into which quartz inclusions were embedded. The effective modulus of elasticity of the cement paste embedded with PCMs was computed using Hobbs model (for modulus of elasticity) as [29],

$$E_{m+P} = \frac{\left(1 - 2v_{m+P}\right)\left(1 - \dfrac{\phi_P}{1 - \phi_Q}\right)E_m}{\left(1 - 2v_m\right)\left(1 + \dfrac{\phi_P}{1 - \phi_Q}\right)}$$

Eq. (2.7)

where E_{m+P} is the effective modulus of elasticity of the paste + PCM composite, and E_m and E_P are the moduli of elasticity of the cement paste matrix and microencapsulated PCM, respectively. The corresponding effective Poisson's ratio of the composite, v_{m+P} was calculated based on the Reuss-Voigt-Hill average [145] as,

$$\upsilon_{m+P} = \left[\left(\upsilon_P \frac{\phi_P}{1-\phi_Q} + \upsilon_m \frac{\phi_m}{1-\phi_Q} \right) + \left(\frac{\upsilon_P \upsilon_m}{\upsilon_P \frac{\phi_m}{1-\phi_Q} + \upsilon_m \frac{\phi_P}{1-\phi_Q}} \right) \right] / 2 \qquad \text{Eq. (2.8)}$$

It should be noted that Hobbs model noted in Equation (2.7) was derived for a case of considerable mismatch between the Poisson's ratios of the components, and assumed that inclusions had a negligible modulus of elasticity compared to that of the matrix (such that $E_i \approx 0$, and $S_i/S_m \approx 1$). As such, instead of homogenizing quartz and cement paste as the matrix, quartz was treated as inclusion and embedded into a matrix composed of PCM microcapsules and cement paste. The effective modulus of elasticity E_{m+P} and Poisson's ratio υ_{m+P} of the homogenized PCM + cement paste composite were used to calculate its effective bulk modulus (K_{m+P}). This served as an input in Equation (2.6) for K_m while the quartz particles were treated as rigid inclusions. Based on these guidelines, the drying shrinkage of a three-component composite, S_{m+P+Q}, was predicted as,

$$\frac{S_{m+P+Q}}{S_{m+P}} = 1 - \frac{\frac{2E_Q\phi_Q}{1-2\upsilon_Q}(1-\frac{S_Q}{S_{m+P}})}{\frac{E_Q}{1-2\upsilon_Q} + \frac{E_{m+P}}{1-2\upsilon_{m+P}} + (\frac{E_Q}{1-2\upsilon_Q} - \frac{E_{m+P}}{1-2\upsilon_{m+P}})\phi_Q} \qquad \text{Eq. (2.9)}$$

where S_{m+P} was obtained as a function of Sm by Equation (2.6). Figure 2.13 shows the measured and predicted shrinkage strains of PCM and/or quartz containing composites normalized by that of plain paste shrinkage, S_m, after 28 days of drying. It is noted that Hobbs model can accurately predict the shrinkage of composites containing both stiff, and/or compliant inclusions. The results indicate that, broadly, PCMs do not restrain paste shrinkage, and fulfill a role similar to air-voids (i.e., in the context of shrinkage) in the system. This is significant as while PCM microcapsules do not reduce shrinkage, in spite of the effects of dilution (i.e., a reduction in paste content), when dosed with quartz inclusions, the latter serve as a shrinkage restraining agent. Nevertheless, since

PCMs are expected to be dosed as replacement of fine mineral aggregates, the overall shrinkage that develops can be adjusted by the dosage of stiff inclusions present in the mixture.
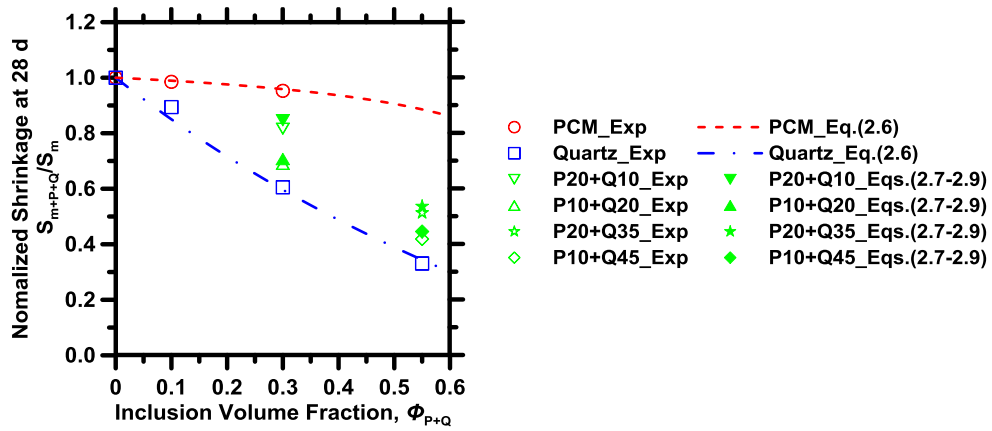
(a)
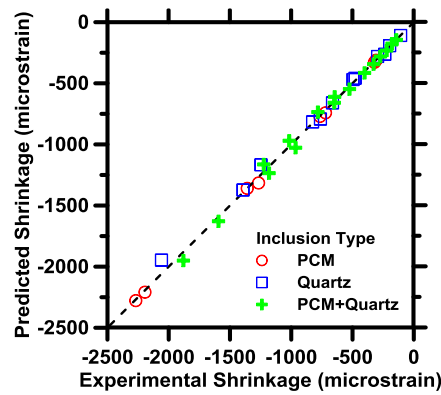
(b)

Figure 2.13: (a) A comparison of measured and modeled drying shrinkage data of all cementitious mixtures after 28 days of drying, normalized by shrinkage of plain paste with w/c = 0.45, (b) modeled drying shrinkage data plotted as a function of experimental shrinkage data.

It is worth pointing out that in practical applications the effect of temperature cycling on the expansion and shrinkage of the PCM capsules may be relevant. While it is well known that thermal

expansion and shrinkage of the PCM's paraffin core is much higher than that of the MF shell, typically, the PCM capsules are only partially filled with core material to account for the thermal expansion mismatch of the core and shell components. In fact, the effective coefficient of thermal expansion of the PCM microcapsules (core + shell) is similar to that of the encapsulation (shell) material, as will be discussed in Chapter 4. Since the coefficient of thermal expansion of the shell is on the same order as that of the cement paste matrix, this ensures that no damage would occur at the interface between the cement paste and the microcapsules when temperature changes – more so since the shell is around an order of magnitude less stiff than the cement paste matrix. As such, the addition of microencapsulated PCMs is expected to exert no detrimental effect on volume changes of cementitious composites.

2.4 Conclusion

This chapter has investigated how the dosage of microencapsulated PCMs influences the durability of cementitious materials. It is noted that, while PCMs remain unaffected in alkaline solutions, they experience a significant enthalpy reduction, on the order of 25%, when exposed to sulfate-bearing environments. The mechanism of such enthalpy reduction was identified as hydrolysis of the melamine-formaldehyde PCM capsule followed by its reaction with sulfate ions to form a melamine-sulfate supramolecular crystal. These reactions result in shell rupture following which the paraffinic PCM core too contacts sulfate ions, resulting in enthalpy reduction. With regards to water sorption, PCMs serve as a non-sorptive inclusion similar to graded quartz sand. Therefore, increasing the volume fraction of either inclusion reduced the volume of water sorbed, and the rate of water sorption. These effects, especially the extent of terminal water sorption, can be estimated for the case of non-sorptive inclusions using Powers' model. Furthermore, the drying shrinkage of

cementitious composites was essentially unaltered by the presence of PCMs, as such compliant inclusions are unable to offer any resistance to the cement paste's shrinkage. On the other hand, stiff quartz inclusions reduced shrinkage significantly – due to the effects of aggregate restraint. The model of Hobbs is able to properly capture the effects of both, inclusion stiffness and volume fraction, providing a means to estimate the shrinkage of cementitious composites containing such inclusions. In general, it is noted that, while PCMs may themselves be detrimentally impacted in sulfate-containing cementitious environments, they do not in any way detrimentally impact the durability of cementitious composites in which they are embedded.

Chapter 3 Restrained shrinkage cracking of cementitious composites containing microencapsulated PCM Inclusions

3.1 Background

Microencapsulated PCMs have been proposed as a means to: (i) reduce the risk of thermal cracking in restrained concretes [37, 51, 123], and, (ii) reduce the energy consumption associated with heating and cooling buildings [60, 61, 63, 69]. The success of PCMs in these applications is ensured by their ability to absorb heat from their surroundings at temperatures in excess of their phase change temperature, and release such heat at temperatures below their phase change temperature. Such temperature-dependent absorption and release of heat is often achieved by an organic phase change material ("core"), which for reasons of shape-stabilization, and to ensure its chemical passivity, is enclosed within a polymer encasement ("shell"); e.g., see Figure 3.1(a).

Expectedly, on account of their soft nature (e.g., typically, the paraffin-based core and polymer shell materials display an elastic modulus on the order of 50 MPa, and 600 MPa, respectively [143, 146]) – the dosage of PCMs into cementitious materials has been shown to result in reductions in the effective compressive strength of the composite (e.g., see Figure 3.1b [123]). If such "strength reductions" are considered in terms of their implications on cracking risk; from a strength of materials perspective (i.e., cracking occurs when the strength of the material is exceeded) – it may be suspected that PCM additions may result in concretes being at a higher risk of cracking.

Therefore, despite their advantage of serving as a sink/source for early-age hydration, and environmental heat – the dosage of PCMs into cementitious materials may be counterproductive due to the strength loss, and amplified concrete cracking risk that results.
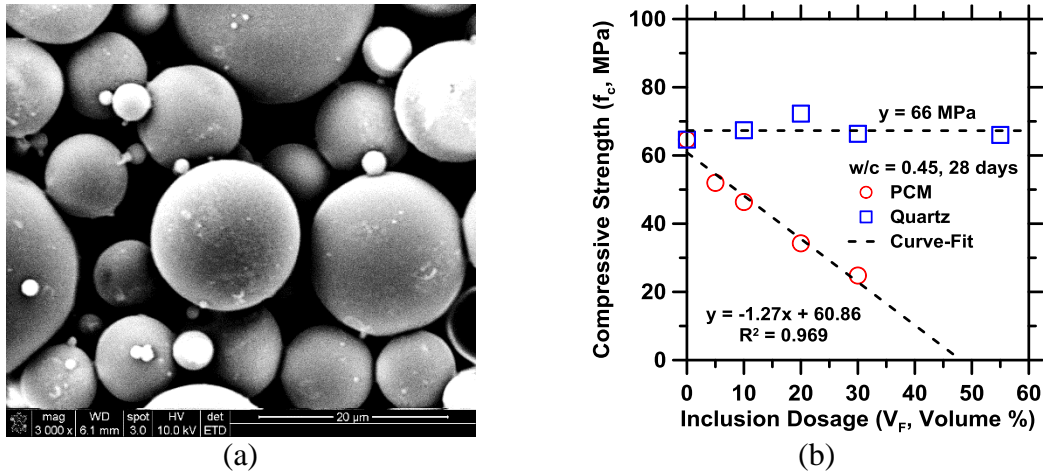
Figure 3.1: (a) A scanning electron micrograph of "core-shell" microencapsulated phase change materials (PCMs) wherein the core is the active phase change component (e.g., often alkanes of composition C_nH_{2n+2}) and the shell is a polymer structure often comprised of melamine-formaldehyde (MF), and, (b) The compressive strength, f_c, of cementitious mixtures containing quartz or microencapsulated PCM inclusions after 28 days of aging as a function of the inclusion volume fraction (V_F) [123].

While the previous chapter has examined aspects of the durability of mature cementitious composites containing PCMs – but not restrained cracking behavior – to definitively answer the question "Does the addition of microencapsulated PCMs render cementitious materials more sensitive to cracking?" a comprehensive assessment of the mechanical properties and cracking sensitivity is undertaken to contrast the cracking behavior of formulations containing stiff (quartz) inclusions and soft (PCM) inclusions. It is shown that PCM inclusions do not amplify the risk of

cracking, but rather, reduce the risk of cracking vis-à-vis stiff inclusion systems. Similar to other soft inclusions (e.g., elastomers, expanded polystyrene, etc. [147, 148]), this outcome is attributed to crack blunting and deflection effects, and the improved stress relaxation [149-151] resulting from PCM dosage, separate from any heat absorption and release related effects.

3.2 Materials and methods

3.2.1 Materials

An ASTM C150 [125] compliant Type I/II ordinary portland cement (OPC) was mixed with deionized (DI) water to prepare cement pastes and mortars as per ASTM C305 [132]. The OPC used had a nominal composition (in terms of mass %) of: 56.5% C3S, 18.0% C2S, 11.4% C4AF and 6.3% C3A. An ASTM C778 [127] compliant graded quartz sand was used as stiff inclusions. The soft inclusions comprised a microencapsulated phase change material (MPCM-24D, Microtek Laboratories Inc.) which consisted of a paraffinous core encapsulated within a MF shell. The PCM was supplied in the form of a powder, and had a phase change temperature around 24°C and a latent heat capacity around 162 kJ/kg (see Figure 2.2). The densities of the OPC, quartz, and microencapsulated PCM were estimated as 3150 kg/m^3, 2650 kg/m^3, and 900 kg/m^3, respectively.

All cementitious mixtures were prepared at a fixed w/c (water-to-cement ratio, mass basis) of w/c = 0.45. The cementitious mixtures formulated consisted of neat cement paste, and mortars containing 10 volume % and 20 volume % of quartz or PCM inclusions. Due to their small particle size, it was difficult to formulate suitably fluid ("nearly pourable") microencapsulated PCM-containing mixtures at higher inclusion volume fractions without the addition of high-dosages of superplasticizer which substantially alters early-age reaction kinetics. Therefore, higher inclusion

dosages were not considered. Herein, each mortar contained only a single type of inclusion (i.e., either quartz sand or microencapsulated PCM), in order to distinguish their influences on restrained cracking behavior. However, in the case of practical concrete proportioning which is carried out on a volumetric basis – the aggregate content is specified as a volume percentage of the overall volume. In circumstances such as these, where the ratio of coarse and fine aggregate in the mixture is defined (fixed), it is expected that PCM inclusions would be dosed by replacing a portion of the fine aggregate by PCM inclusions, volumetrically. Such dosage could be carried out to ensure a particular level of heat absorption and release, or to reduce the cracking risk.

3.2.2 Experimental methods

3.2.2.1 Particle Size Distributions

The particle size distributions (PSDs, Figure 3.2) of the OPC, quartz, and PCM were measured using Static Light Scattering (SLS) using a Beckman Coulter LS13-320 particle sizing apparatus fitted with a 750 nm light-source. Each solid was dispersed into primary particles via ultrasonication in isopropanol (IPA), which was also used as the carrier fluid. The complex refractive indices of the OPC, quartz, and PCMs were taken as $1.70 + 0.10i$, $1.53 + 0.00i$, and $1.54 + 0.00i$, respectively (see Section 2.2.2). The maximum uncertainty in the PSDs was around 6% based on six replicate measurements.
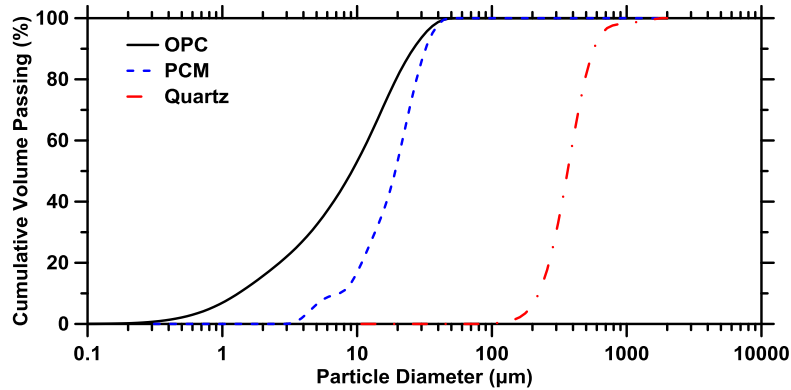
Figure 3.2: The particle size distributions of the OPC, quartz, and microencapsulated PCM particulates as measured using static light scattering (SLS).

3.2.2.2 Splitting Tensile Strength

The splitting tensile strength (f_t, MPa) of all specimens was measured as per ASTM C496 [152]. The strength measurements were carried out after 1, 3, 7, and 28 days of curing for cylindrical specimens (diameter x height: 101.6 mm x 203.2 mm) maintained at 25 ± 3 °C in saturated limewater. A compressive force was applied along the length of the cylindrical specimen at a rate of 10 kN/s until failure occurred. A thin plywood strip was used to uniformly distribute the load along the length of the cylinder and the maximum load borne by the specimen was used to obtain the splitting tensile strength. The tensile strength represents the average of three specimens cast from the same mixing batch.

Static (Compressive) Elastic Modulus: The elastic (or Young's) modulus (E_C, GPa; N.B.: this represents the chord modulus of elasticity [123]) of all specimens was measured as per ASTM C469 [153]. The elastic modulus measurements were carried out after 1, 3, 7, and 28 days of curing for cylindrical specimens (diameter x height: 101.2 mm x 203.2 mm) maintained at 25 ± 3 °C in

46

saturated limewater using a MTS 311.31 closed-loop servo-hydraulic instrument. A quick-setting gypsum plaster "Hydrostone" was used for capping the specimens to ensure uniform compression at the ends of each cylinder. The reported elastic modulus represents the average of three specimens cast from the same mixing batch.

3.2.2.3 Unrestrained Shrinkage

Unrestrained deformations of cementitious specimens were measured as described in ASTM C157 [131]. Free shrinkage (ε_{FS}) was measured using prismatic specimens (25.4 mm x 25.4 mm x 285 mm). After saturated curing for the first 24 hours, the prismatic specimens were demolded, double-bagged in Ziploc© bags - to ensure partially sealed conditions, and limit water loss - and then stored in an environmental chamber (Darwin KB024) at 25 ± 0.1 °C and 87 ± 0.1 % RH for an additional 6 days. The condition of partial sealing was implemented to mimic conditions of the restrained ring setup – which could only be sealed by "double bagging" (see below). After 6 additional days of "partially sealed" (i.e., since the double bagging did not allow perfect sealing) curing, the samples were properly sealed on 4 sides using two-layers of aluminum tape such that only two (long) parallel faces remained unsealed to ensure symmetric (1D) drying – analogous to the conditions of the restrained ring setup. After this time, the samples were stored at 50 ± 0.1 % RH and 75 ± 0.1 % RH (relative humidity) for an additional three days. Shrinkage and mass loss were measured after 1, 3, 5, 7, 8, 9, and 10 days from the time of casting. The shrinkage and mass loss data shown represent the average of four specimens cast from the same mixing batch. The unrestrained shrinkage thus measured enabled calculation of the elastic stress that would develop – following Hooke's Law – which upon comparison with the measured residual stress allows quantification of the extent of stress relaxation (see below) [154-157].

3.2.2.4 Restrained Shrinkage

The dual ring test was used to assess the cracking tendency of the cementitious mixtures [51, 155-158]. The apparatus consists of two rings (i.e., an inner ring and an outer ring) made of Invar 36 to minimize the influence of temperature on the results. The coefficient of thermal expansion of the Invar 36 is around 2.5 $\mu\varepsilon$/°C [51]. The inner Invar ring had an outer radius $R_{I,o}$ of 50.8 mm and an inner radius $R_{I,i}$ of 44.5 mm. The inner ring was instrumented with four strain gauges (CEA-00-350Ω; ε_I) placed at 90° from each other at the mid-height on the inner circumference. The outer invar ring had an outer radius $R_{O,o}$ of 82.6 mm and an inner radius $R_{O,i}$ of 76.2 mm. The outer ring was also instrumented with four strain gauges (CEA-00-350Ω; ε_O) placed at 90° from each another at the mid-height on the outer circumference. Both the inner and outer rings had a height of 25.4 mm. Strains were measured at 5 minute intervals, starting about 30 minutes after mixing until the test was terminated. The instrumented rings were placed at the center of an acrylic base that was coated with a form release agent to minimize bonding. The rings were also coated with a form release agent to prevent restraint due to bonding with the cementitious mixtures. The elastic modulus and Poisson's ratio of the Invar rings were taken as E_{inv} = 141 GPa, and v_{inv} = 0.28, respectively [51].

The fresh cementitious mixture was cast between the two rings and vibrated to ensure consistent filling. The setup was double-bagged in Ziploc© bags and then maintained in a programmable environmental chamber (Darwin KB024) at 25 ± 0.1 °C and 87 ± 0.1 % RH to limit moisture loss over the first 7 days. A PVC coversheet formed as an annulus was additionally used to seal the top-surface of the rings to minimize the potential for drying. After 7 days of "partially sealed" curing, the rings were placed on an elevated wire-mesh platform with their top and bottom surfaces

48

exposed, and dried symmetrically at 50 ± 0.1 % RH or 75 ± 0.1 % RH until cracking occurred. Restrained shrinkage was monitored on duplicate ring specimens cast from the same mixing batch.

The analytical expressions required to assess the incremental elastic stress developed $\Delta\sigma_{el}$, and the maximum residual stress developed σ_θ (at $r = R_{I,o}$) are noted in [51, 155-158]:

$$\Delta\sigma_{el} = -\Delta\varepsilon_{FS}\left[\frac{\left(1+\upsilon_{inv}\right)R_{I,i}^2 + \left(1-\upsilon_{inv}\right)R_{I,o}^2}{\left(R_{I,o}^2 - R_{I,i}^2\right)E_{inv}} + \frac{\left(1-\upsilon_c\right)R_{I,o}^2 + \left(1+\upsilon_c\right)R_{O,i}^2}{\left(R_{O,i}^2 - R_{I,o}^2\right)E_c}\right]^{-1}\frac{R_{I,o}^2 + R_{O,i}^2}{R_{O,i}^2 - R_{I,o}^2} \quad \text{Eq. (3.1)}$$

$$\sigma_\theta\left(r = R_{I,o}\right) = -\varepsilon_I E_{inv}\left[\frac{R_{O,i}^2 + R_{I,o}^2}{R_{O,i}^2 - R_{I,o}^2}\frac{R_{I,o}^2 - R_{I,i}^2}{2R_{I,o}^2}\right] - \varepsilon_O E_{inv}\left[\frac{R_{O,o}^2 - R_{O,i}^2}{2R_{O,i}^2}\frac{2R_{O,i}^2}{R_{O,i}^2 - R_{I,o}^2}\right] \quad \text{Eq. (3.2)}$$

Further details regarding the analytical expressions and their derivation can be found elsewhere [117, 154, 158]. The ratio of the residual stress over the elastic stress at any given time yields the stress relaxation ratio σ_R (unitless), i.e.,

$$\sigma_R(t) = \sigma_\theta(t)/\sigma_{el}(t) \quad \text{Eq. (3.3)}$$

The stress relaxation ratio indicates the effects of viscoelastic (stress) relaxation as a result of which the residual stress is substantially lower than the elastic stress (i.e., the stress developed following Hooke's law for the ring geometry). It should be noted that the stress relaxation ratio was "zeroed" to 1 day since measurements of free shrinkage were initiated at this time.

3.3 Results and discussion

3.3.1 Strength behavior: Contrasting the effects of soft and stiff inclusions

Figure 3.3(a) shows the measured splitting tensile strength (f_t) for the neat cement paste, and mortars containing PCM and quartz inclusions. Interestingly, all specimens show similar tensile strengths independent of the presence of, and type of inclusions present. This indicates that the splitting tensile strength of the mixtures is "paste controlled". As such, for the inclusions present; i.e., PCM (weaker than the paste matrix), and quartz (stronger than the paste matrix), in both cases the failure of the paste, and hence its tenensile strength dictates the failure of the overall composite. Often the splitting tensile strength of cementitious mixtures is assumed to be on the order of 10% of the compressive strength (f_c), e.g., see Figure 1(b) [7, 159]. While this rule-of-thumb remains valid for both the neat cement paste, and quartz containing mixtures (e.g., herein, $f_t \approx 0.12 f_c$ at an age of 28 days) – it is violated in the case of the PCM-containing mixtures wherein reductions in the compressive strength do not correlate with reductions in the tensile strength. This is an important observation which indicates that: (i) compressive-to-tensile strength correlations should not be applied "as is" to mixtures containing soft inclusions, in general, and, (ii) while in the case of compressive loading PCM inclusions act as a strength-reducing defect in the system – as elaborated below, in the case of tensile loading, their high compliance, and low modulus ensures that only the paste matrix transfers, and resists stresses (albeit for the range of PCM volume fractions considered) – as a result of which the tensile strength of all formulations is similar to that of the neat paste.

It should furthermore be noted that in the case of compressive loading, when the inclusions are stiffer than the paste, assuming near-perfect bond between the inclusions and matrix, stresses concentrate within the inclusions. For this reason, in the case of the quartz inclusions, the compressive strength is similar across all dosages – as failure only occurs when the stress capacity

of the paste is exceeded (i.e., since the paste is weaker than the quartz inclusions, see Figure 3.1b). On the other hand, when the inclusions are compliant, stresses concentrate at the matrix (paste)-inclusion interface – in increasing proportion as the stiffness contrast between the matrix and inclusions enhances. Therefore, even if the interface regions (often referred to as the interfacial transition zone, ITZ, in cementitious systems [160-162]) are considered to demonstrate similar strengths independent of the type of inclusion present – in the event of compressive loading, PCM inclusions induce strength reductions (see Figure 3.1b) on account of a risk of interfacial failure that amplifies with an increase in soft (PCM) inclusion dosage [86, 87].

Coming back to the case of tensile loading, irrespective of the inclusion stiffness, failure initiates at the apex of the inclusion followed by progressive debonding (i.e., due to dilatation) along the matrix-inclusion interface. As a result, failure is interface-dominated independent of the nature of inclusions present [163]; so long as the inclusions are broadly, similar in size. Therefore, for PCM and quartz inclusions which are assumed to feature similar ITZ properties (i.e., similar to the neat cement paste matrix; see similar strengths of inclusion-containing and inclusion-free mixtures in Figure 3.3a) – the measured tensile strength is similar over the entire range of inclusion dosages considered herein (see Figure 3.3a) [86]. It should be noted however, that the size of the ITZ surrounding the quartz and PCM inclusions is substantially different, i.e., due to the differences in their sizes; e.g., the quartz inclusions are > 10 times larger than the PCM inclusions (see Figure 3.1). Of course, this reasoning anticipates that all the inclusions, whether PCM or quartz, are similarly dispersed within the paste matrix. Furthermore, even if the ITZ were slightly weaker at some, but not all interfacial locations (i.e., for a given inclusion type, and volume fraction) this would not result in noticeable strength alterations as this would require a percolated series of

nearest neighbor inclusions – all of which feature similarly weak(er) interfacial zones.
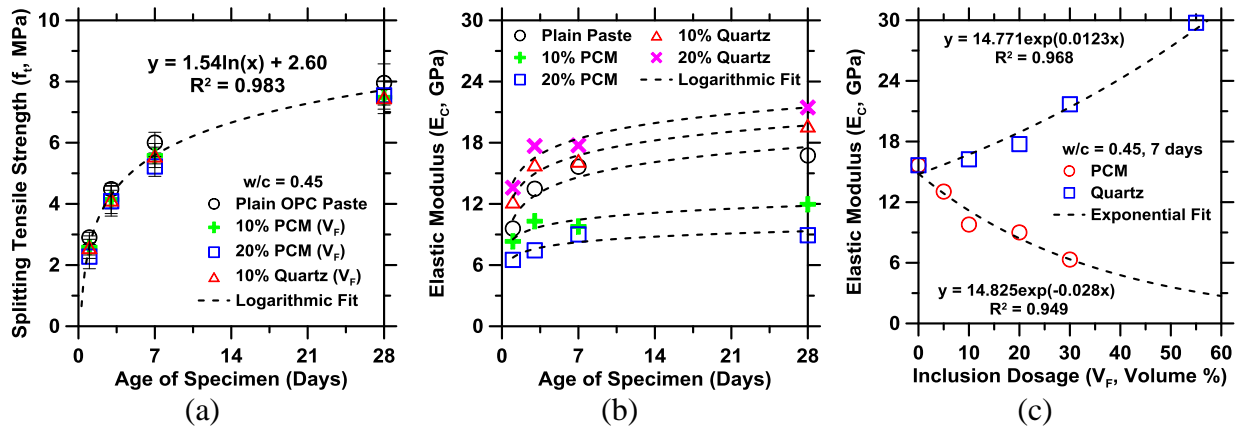
Figure 3.3: (a) The splitting tensile strength as a function of specimen age, (b) The static (compressive) elastic modulus as a function of specimen age for the plain cement paste, and quartz and PCM inclusion dosed mixtures, and, (c) The static (compressive) elastic modulus as a function of inclusion dosage after 7 days of curing for quartz and PCM dosed mixtures.

Even in the case of the failure of neat cement paste, although there is no ITZ formed in absence of inclusions, plain paste formulations are expected to feature initial flaws ranging in size from a few microns to 100 µm (i.e., the size of a large cement particle) [118]. These flaws which control tensile (opening) failure, are expected to produce macroscopic behavior similar to that induced by the weaker nature of the ITZ that forms when inclusions are present. Therefore, upon tensile loading, whether inclusions are present or not, the cementitious systems shown in Figure 3.3(a) show similar tensile resistance (strength). It should be noted however, the cement paste matrix that surrounds PCM inclusions is likely to experience higher tensile stresses at the matrix-inclusion interface as compared to the paste matrix surrounding quartz inclusions – for the same externally applied strain level. This response emanates from the higher compliance of the PCM inclusions as

compared to quartz inclusions. However, this effect is not very significant at low inclusion dosages (i.e., ≤ 20 volume %) in which the inclusions are reasonably well-dispersed, as their interfacial zones, and the stresses that develop therein are not expected to percolate in the microstructure.

Figures 3.3(b-c) show the compressive elastic modulus Ec of the different cementitious mixtures as a function of time and inclusion dosage. Expectedly, the addition of soft PCM inclusions was found to reduce the elastic modulus, while the dosage of quartz inclusions that are stiffer and stronger than the cement paste increases the elastic modulus. The resulting decrease (PCM) or increase in modulus (quartz) scales as a function of the inclusion dosage in the system – as shown in Figure 3(c) – and can be reliably estimated using the models of Hobbs [141] and Garboczi and Berryman [164] as shown by Young et al. [165] and Falzone et al. [123]. It should be noted that the data shown in Figures 3.3(b-c) is acquired in compression – as such, while the elastic modulus of PCM-containing mixtures is noted to degrade with their increasing dosage, further work is needed to quantify changes in the tensile modulus of such systems, and any changes therein as a function of the stiffness of inclusions present due to complexities including interface debonding (N.B.: For typical cementitious formulations, the tensile and compressive elastic modulus are often within ± 30% of each other [166-169])

3.2 Unrestrained and restrained volume changes: Shrinkage and cracking behavior

Figure 3.4 shows the shrinkage response of the plain and inclusion-containing cementitious mixtures as a function of time for two drying regimes, i.e., partially sealed over the first 7 days, followed by: (i) drying at 50% RH (Figure 4a), and, (ii) 75% RH (Figure 4b) over the subsequent

3 days. Expectedly, both series of mixtures show a similar extent of free shrinkage and mass loss over the first 7 days. After 7 days, expectedly, mixtures exposed to 50% RH lose more mass and shrink at a higher rate than mixtures dried at 75% RH. It is important to note that while both the quartz and PCM mixtures show a similar extent of mass loss (i.e., when normalized by the mass of paste in the system) – in the case of shrinkage, quartz-containing mixtures shrink slightly less than those containing PCM, or the plain paste mixture due to the restraint to paste shrinkage offered by the stiff quartz inclusions [116].

The PCM inclusions on the other hand, due to their compliant nature are unable to restrain the shrinkage of the paste – as a result, the plain and PCM-containing mixtures shrink equivalently; in terms of their rate and extent of shrinkage. Such behavior was also observed by Egan et al. [116] who noted that when the inclusions are impermeable (or less permeable than the cement paste) – moisture loss, but not shrinkage, can be simply described by normalizing the mass loss data by the mass fraction of cement paste in the composite. The shrinkage data shown in Figure 4 serves as an input into Equation (3.1) to calculate the elastic stress developed (and hence infer the extent of stress relaxation) in the PCM and quartz mixtures as a function of time.
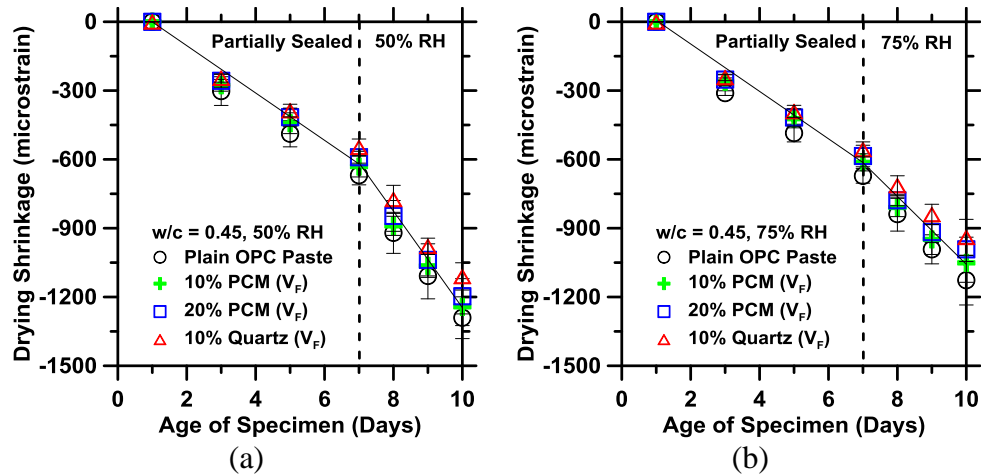
Figure 3.4: (a) Free shrinkage as a function of time for plain cement paste, and quartz and PCM inclusion dosed mixtures. The rate of shrinkage in the partially sealed and 50% RH drying periods is on the order of -100 µε/day and -200 µε/day, respectively. The mass loss from 1-to-7 days, and from 7-to-10 days is on the order of 0.35% and 2.15%, respectively (by mass of cement paste), and, (b) Drying shrinkage as a function of time for plain cement paste, and quartz and PCM inclusion dosed mixtures. The rate of shrinkage in the sealed and 75% RH drying periods is on the order of -100 µε/day, and, -145 µε/day, respectively. The mass loss from 1-to-7 days, and from 7-to-10 days is on the order of 0.35% and 1.80%, respectively (by mass of cement paste). The solid black lines show the general trend of the dataset.

Figure 3.5(a-b) shows the residual stress developed in the plain paste, and PCM- and quartz-containing specimens as a function of time. Residual stress development over the first 7 days, i.e., when the ring setup is double-bagged to ensure partially sealed conditions – is noted to scale in the order: 10% quartz > neat paste > 10% PCM > 20% PCM. Given that these mixtures all show similar levels of shrinkage over the first 7 days (in fact, the 10% quartz mixture shrinks slightly

55

less than the other compositions; see Figure 3.4a) – the scaling in (tensile) residual stresses appears to follow the magnitude of the elastic modulus of these materials; which also scales in the same order (e.g., see Figure 3.3c). When the cementitious mixtures are exposed to drying – the rate of stress development increases dramatically until the specimen cracks. It is important to note that the rate of stress development is similar across all mixtures whether drying occurs at 50% RH or 75% RH (see Figure 3.5c).

(a)   (b)   (c)
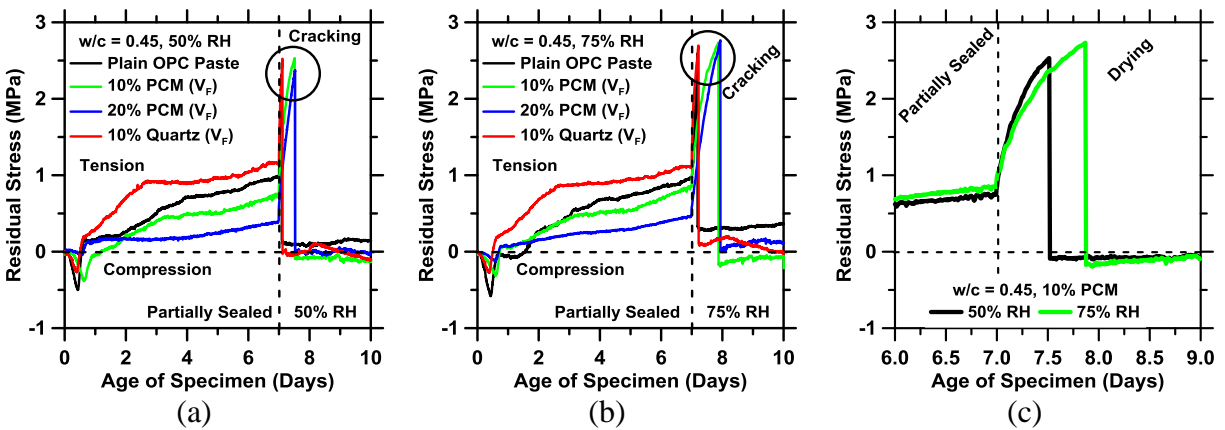
Figure 3.5: Residual stress development measured using the dual ring setup as a function of time for plain cement paste, and quartz and PCM inclusion dosed mixtures. After 7 days of partially sealed curing the specimens were dried symmetrically, i.e., from their top and bottom surfaces at: (a) 50% RH, and, (b) 75% RH. The time at which the stress drops sharply indicates macroscopic damage localization (cracking), when a single-crack formed in the ring samples. (c) A comparison of residual stress development in the 10% PCM mixture upon drying at 50% RH and 75% RH. The stress development curves show near-overlap with each other. The measured stresses represent the average of duplicate ring specimens.

In fact, the stress curves for drying at different RHs trace the same envelope – with cracking

occurring at a slightly lower stress level for mixtures dried at 50% RH – as compared to mixtures dried at 75% RH (see also Figure 6a). This is because up on exposure to an ambient RH that is lower than the internal RH, cementitious mixtures rapidly lose moisture. The rate of such moisture loss depends upon the diffusion coefficient of moisture within the cement paste (on the order of 10-12 m^2/s for a cement paste with w/c = 0.45 [137, 170]); as a result a steeper moisture gradient manifests in a material dried at a lower RH, than a material dried at a higher RH [170]. The presence of a steeper moisture and shrinkage gradient would result in a larger level of shrinkage-induced microcracking in the paste dried at 50% RH as compared to that dried at 75% RH. Therefore, due to the faster, and amplified accumulation of damage in the former (see Figure 3.5c), and a shorter time interval for stress relaxation (i.e., on account of a faster rate and extent of loading upon drying), formulations dried at 50% RH experience accelerated macroscopic damage localization (cracking) as compared to formulations dried at 75% RH. This suggests that cracking in these materials manifests as a fracture (i.e., crack growth) controlled rather than a stress (i.e., strength of materials) controlled circumstance.

Significantly, all specimens including the PCM-containing specimens fail at similar stresses – indicative of their similar strengths (see also Figure 3.3a). Nevertheless, it is important to note that all the cementitious mixtures fail at tensile stresses substantially (around 50%) lower than the tensile strength of the material around 7 days (see Figure 3.6a). This is postulated to be on the account of the formation and sub-critical growth of microcracks in the ring specimens over the first 7 days at sub-critical stresses (e.g., at 3 days, the residual stress developed is $\leq 0.25ft$ across all mixtures). As a result, when the ring specimens are exposed to aggressive drying beyond 7 days, the microcracks (flaws, defects) that are initially present rapidly grow until they coalesce.

Thus, the materials fail at stress levels lower than their pristine tensile strength. Therefore, the failure process is dictated by the evolution of incremental and accumulative damage resulting in the degradation of the tensile capacity of the material as compared to a "pristine" cementitious material that would typically fail only in the vicinity of a major flaw, or at a stress level similar to or greater than its tensile strength (i.e., due to the inherent distribution and variability in the material properties) [171-173].
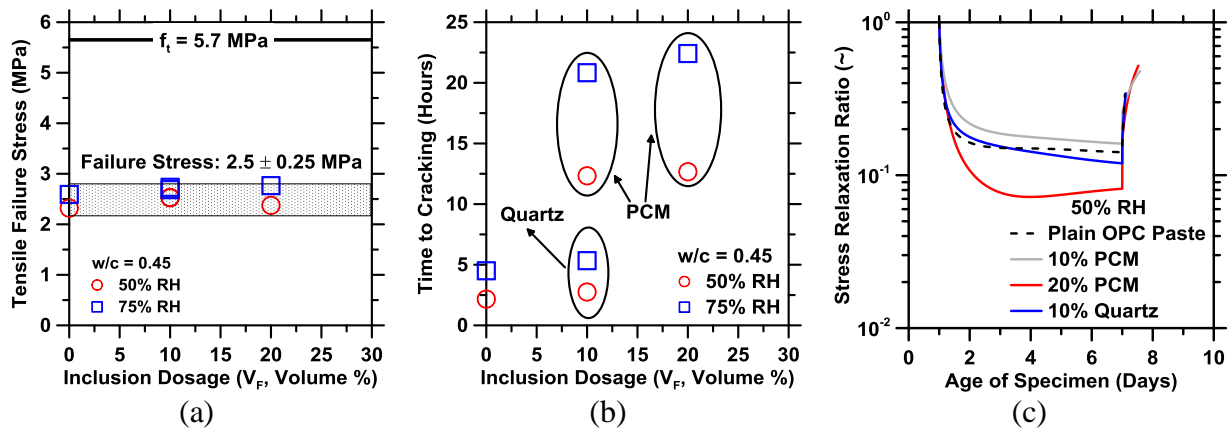
Figure 3.6: (a) The stress at failure, and, (b) the time to failure from when drying was initiated at 7 days as a function of the inclusion volume fraction VF (volume %) for the plain cement paste, and quartz- and PCM-containing specimens. The failure stress and the time to failure represent the average of duplicate ring specimens, and, (c) The stress relaxation ratio (σ_R, unitless) calculated for the plain cement paste, and quartz and PCM inclusion dosed mixtures.

Coming back to the time of cracking (i.e., from when drying at 50% RH or 75% RH is initiated until the specimen fails), expectedly, the time to cracking is extended when drying is carried out at 75% RH rather than 50% RH; due to the slower rate of damage accumulation, and the extended time period available for stress relaxation. It is furthermore important to note that while all the

cementitious formulations fail at similar stresses, PCM-containing cementitious materials show a significantly extended time to cracking (e.g., see Figure 3.6b). For example, up on exposure at both 50% RH and 75% RH, and for an inclusion dosage of 10 volume % PCM-containing mixtures demonstrate a ≥ 4.5x increase in the time to cracking as compared to quartz-containing mixtures. Close examination of the stress relaxation ratio shown in Figure 3.6(c) reveals that the extent of stress relaxation is broadly similar for the plain cement paste, and mixtures containing 10 volume % of either quartz or microencapsulated PCM inclusions. However, the extent of stresses relaxed is substantially enhanced in the mixture containing 20 volume % PCM. When considered in the context of the time to cracking – this suggests that the addition of PCMs at low dosages ensures benefits associated with crack deflection and blunting (i.e., which increases the crack tortuosity and necessitates a higher driving force for crack propagation), such that in spite of the similar levels of stress relaxation, an increase in time to cracking is observed (see Figure 3.6b) [174]. As the PCM inclusion volume fraction is increased yet further – the improved compliance (enhanced stress relaxation) offered by PCM-containing mixtures superimposes on top of the effects of crack blunting and deflection such that the time to cracking enhances further – although only slightly so as compared to the 10 volume % PCM formulations. It is important to note that other soft inclusions with a compliance similar to that of the PCM microcapsules (e.g., elastomers, expanded polystyrene) are expected to offer similar benefits in cementitious composites, i.e., in terms of increasing the time to cracking [117, 149, 175]. However, if controlling early- or later-age temperature rise and gradients is specifically desired, the latent heat storage offered by PCM inclusions makes their use mandatory [51].

The beneficial effects of PCM additions were also observed by Fernandes et al. [51] who noted

that the critical crack tip opening displacement (CTOD$_c$, in mm) of PCM-containing mixtures, which accounts for interlock effects of the microstructural components, was higher than that of formulations devoid of compliant PCM inclusions. Furthermore, the fracture toughness K$_{IC}$ of PCM-dosed mortars was also found to be similar to or slightly higher than that of neat cement paste; for PCM dosages of ≤ 20 volume % [51]. Therefore, it appears as though a reduction in material stiffness in the vicinity of a crack (i.e., due to the incorporation of compliant PCM particulates) results in the material being able to undergo larger inelastic deformations in the direction of crack-opening prior to the formation (coalescence) of a macro-crack, as a result of which the CTOD$_c$ increases. Indeed, close examination of the strain energy release rates GR determined via notched beam fracture tests indicated that, in the case of PCM containing mixtures, the inelastic component of G$_R$ is dominant – indicating that more energy is being dissipated via inelastic deformations. This increase in inelastic deformations as compared to those of neat (or quartz-containing) cementitious mixtures is thought to induce crack blunting and deflection which enhance the tortuosity of the crack-path; resulting in a heightened resistance to crack propagation. Taken together, these results indicate that the extension in the time to cracking provided by the addition of PCM inclusions is in large part due to the effects of crack blunting and deflection (i.e., which results in a lower rate of microcrack accumulation, coalescence, and propagation), and to a smaller extent on account of an improved ability for stress relaxation (i.e., higher compliance). These results substantiate the premise that the dosage of soft inclusions does not amplify the risk of cracking – rather, dosage of compliant microscale inclusions is noted to valuably enhance the cracking-resistance of cementitious composites. The outcomes of this research provide useful inputs for modeling of the influences of soft inclusions on the cracking behavior of matrix-inclusion composites. First, it demonstrates that the often assumed scaling relation (X:Y, where X

often takes a value of 1, and y often takes a value of 10 [159]) that the tensile strength (X) reduces in fixed proportion with the compressive strength (Y) of cementitious is invalid when soft inclusions may be present. As a result, rather than remaining fixed, the ratio (X:Y) can take values ranging from 1:12 to 1:4.5 as the dosage of soft (PCM) inclusions elevates from 0 volume % to 20 volume % in cementitious composites. Second, the coupled effects of viscoelasticity, and crack blunting/deflection on reducing cracking risks have been quantified by the stress relaxation ratio (σ_R), which can be used as a critical input for modelling the cracking behavior of cementitious composites containing soft inclusions.

3.4 Conclusion

By carefully combining measurements of (indirect) tensile strength, and restrained and unrestrained shrinkage, this chapter has comprehensively examined the influences of compliant, microscale PCM inclusions on the cracking resistance of cementitious composites. Significantly, it is noted that in spite of inducing substantial reductions in the compressive strength of cementitious composites, the dosage of PCM inclusions induces no change in the tensile capacity (strength) of the material; compared with neat cementitious mixtures, or those containing inclusions stiffer than the paste matrix. This is because tensile failure is an interface-controlled process − which being similar across all formulations, for the volume fractions considered − ensures that the tensile strength remains unchanged and independent of the type of inclusions present. Furthermore, PCM-containing specimens show a substantial delay in their time to cracking (e.g., by ≥ 4.5x for the inclusion dosages considered) as compared to neat, or quartz-containing cementitious mixtures. Such extensions in the time to cracking were attributed dominantly to the effects of crack-blunting and deflection induced by the PCM inclusions; and to

61

a lesser extent on account of enhanced stress relaxation. Taken together, these results indicate that in contrast to the (intuitive) expectation of an amplified cracking risk – the addition of compliant, microscale PCM (and other soft) inclusions in fact reduces the risk of and time to cracking in cementitious composites.

Chapter 4 Determination of thermal deformation properties of microencapsulated phase change materials in cementitious composites

4.1 Background

PCM particulates with a median diameter on the order of 10 to 20 µm are often produced by an interfacial polymerization process wherein a polymer shell (e.g., of melamine-formaldehyde) is used to encapsulate a core material (e.g., alkanes such as paraffin wax). To provide stress relief over multiple phase change cycles, typically, the PCM microcapsules are only partially filled. As a result, they contain some internal porosity [56]. Due to the presence of this internal porosity, and their small size, it is challenging to characterize the material properties of these core-shell structures. This is especially so in the context of thermal deformation behavior when both the core and the shell would expand (or contract), albeit to different extents. This is an issue in applications such as concrete pavements, where it is important to know the thermal deformation coefficients of inclusions that are embedded in the cementitious matrix so as to quantify their influences on the volume stability of the overall solid. This chapter aims to assess the influences of PCM microcapsules on the effective thermal deformation coefficient of cementitious composites by effective medium approximation (EMA) and measurements of linear thermal deformation of prismatic composite specimens. By identifying an EMA capable of accurately estimating the effective thermal deformation coefficient of multicomponent composites consisting of a matrix and core-shell inclusions, a general approach is highlighted for retrieving the thermal deformation properties of core-shell microcapsules or other particulate inclusions embedded in a continuous

matrix, and for designing cementitious composites containing microencapsulated PCMs.

4.2 Materials and methods

4.2.1 Materials

An ASTM C150 [125] compliant Type I/II ordinary portland cement (OPC) was mixed with deionized (DI) water to prepare cement pastes (matrix only) and mortars (matrix + inclusions) in accordance with ASTM C192 [126]. The OPC had a nominal mass-based mineralogical composition of: 56.5% Ca_3SiO_5, 18.0% Ca_2SiO_4, 11.4% $Ca_4Al_2Fe_2O_{10}$, 6.3% $Ca_3Al_2O_6$, 4.6% $CaCO_3$, and 1.1% $CaSO_4.2H_2O$. ASTM C778 [127] compliant graded quartz sand and microencapsulated PCM inclusions (MPCM24D, Microtek Laboratories) were used as inclusions within the cement mortars. The microencapsulated PCMs consisted of a paraffin core encapsulated within a melamine-formaldehyde (MF) shell. The microencapsulated PCMs were received in the form of dry powders. The corresponding peak melting temperature and enthalpy of phase change of microencapsulated PCMs were 27.8°C and 161.2 ± 0.5 kJ/kg representing the average value over three melting and solidification cycles.

Cementitious mortars were prepared with various volume fractions (i.e., dosages) of microencapsulated PCM and/or quartz inclusions at a water-to-cement ratio (w/c, mass basis) of 0.45. For mortars containing microencapsulated PCM inclusions only, the inclusions were dosed for three different volume fractions, namely, 5, 10 and 20 vol.%. For mortars containing quartz inclusions only, the quartz dosages were 10, 20, and 50 vol.%. For mortars containing mixed inclusions, the total inclusion volume fraction was fixed at 50 vol.%, where the microencapsulated PCM inclusions comprised 10, 15, or 20 vol.%. The microencapsulated PCMs were mixed with

64

the anhydrous OPC by hand prior to the addition of DI water to ensure random and uniform distribution in the mortar. To enhance the fluidity of the fresh mixtures, a commercially available water-reducing admixture (MasterGlenium 7500, BASF Corporation) was added at a dosage on the order of 0-to-1.5 wt.% by mass of cement, depending on the type and dosage of inclusions present.

4.2.2 Experimental methods

Thermal deformation coefficient measurements were carried out using prismatic specimens with various mixture proportions, as described above. The specimens were cast in 2.54 cm x 2.54 cm x 28.50 cm molds in accordance with ASTM C157 [131] and cured under 100% relative humidity for the first 24 h at 25°C. Following demolding after 24 h, the specimens were sealed with aluminum tape and cured in sealed bags at 25°C for 28 days. Then, the length of each specimen was measured at 25°C and the specimens were transferred to an environmental chamber (KB024-DA, Darwin Chambers Company) at 45°C, and stored for 2 h until they reached thermal equilibrium. The fractional length change (i.e., the linear thermal strain) $\Delta L/L0$ due to temperature change $\Delta T = 45°C - 25°C$ was measured with a length comparator. Then, the thermal deformation coefficient of the specimens was calculated according to,

$$\alpha_{eff} = \frac{\Delta L}{L_0 \Delta T}$$
(Eq. 4.1)

In addition, elastic thermal strain within the specimens was verified by also calculating α_{eff} based on a temperature change from 5°C to 45°C and verifying that the measured α_{eff} was independent of the imposed temperature change. It was also confirmed that the specimens recovered their initial length when returned to their initial temperature of 25°C. Such elastic stress-strain behavior implies that the thermal deformation coefficient of cementitious composites would remain constant

65

across the range of diurnal temperature variations that would

be experienced by a concrete pavement. However, when the concrete's temperature falls below 0°

C, its thermomechanical behavior is complicated by melting and freezing of water within its pores

and thus cannot be treated as simple elastic deformation.

4.2.3 Effective medium approximation

This study has considered three simple effective medium approximations that can be applied to

predict the effective thermal deformation coefficient α_{eff} of composites consisting of two or more

constituents, and has found that an EMA derived by Schapery [176] which gave upper and lower

bounds for the effective thermal deformation coefficient α_{eff} of composites with N components

based on energy conservation considerations gives the best predictions. In this case, α_{eff} was

expressed as an average of upper and lower bounds such that

$$\alpha_{eff} = \overline{\alpha} + (\frac{\overline{K\alpha}}{\overline{K}} - \overline{\alpha})\frac{\frac{1}{K_L} - \frac{1}{K_{eff}}}{\frac{1}{K_L} - \frac{1}{\overline{K}}} \pm \Delta\alpha \qquad \text{(Eq. 4.2)}$$

Here, the overline denotes a volume-weighted average over the constituents, i.e. [176],

$$\overline{\alpha} = \sum_{n=1}^{N} \phi_n \alpha_n, \quad \overline{K} = \sum_{n=1}^{N} \phi_n K_n, \quad \text{and} \quad \overline{K\alpha} = \sum_{n=1}^{N} \phi_n K_n \alpha_n \qquad \text{(Eq. 4.3)}$$

In addition, K_L is given by,

$$K_L = (\sum_{n=1}^{N} \frac{\phi_n}{K_n})^{-1} \qquad \text{(Eq. 4.4)}$$

and the effective bulk modulus K_{eff} can be estimated as the average of K_L and $\overline{K}$, i.e.,

$$K_{eff} = \frac{K_L + \overline{K}}{2} \qquad \text{(Eq. 4.5)}$$

66

Finally, the deviation $\Delta\alpha$ in α_{eff} from the average was expressed as [176],

$$\Delta\alpha = \frac{(\frac{1}{K_L} - \frac{1}{K_{eff}})^{1/2}(\frac{1}{K_{eff}} - \frac{1}{\overline{K}})^{1/2}}{\frac{1}{K_L} - \frac{1}{\overline{K}}}[(\frac{1}{K_L} - \frac{1}{\overline{K}})(\overline{K\alpha^2} - \frac{(\overline{K\alpha})^2}{\overline{K}}) - (\frac{\overline{K\alpha}}{\overline{K}} - \overline{\alpha})^2]^{1/2} \quad \text{(Eq. 4.6)}$$

Note that the aforementioned EMA was developed for a linearly elastic composite featuring isotropic constituent materials with arbitrary geometry. The effective thermal deformation coefficient predicted depends only on the volume fractions and thermomechanical properties of the constituent materials but is independent of their spatial distribution. They can also be extended to a composite made of any number of constituents. As such, the EMA is easily applied to cementitious and other composite materials with more than one type inclusion, including both fine aggregates (e.g., quartz sand) and soft inclusions (e.g., microencapsulated PCM) as well as coarse aggregates that would be present in a typical concrete pavement. In addition, several other EMAs have been developed specifically for two-component composites, with further details can be found in [177]. This study presents a general method to retrieve the thermal deformation coefficient of particulate inclusions that are difficult to measure directly by combining Schapery's model with measured effective thermal deformation coefficient. Here, the thermal deformation coefficient of the inclusions were retrieved by least-square fitting the experimentally measured effective thermal deformation coefficient for M different inclusion volume fractions ϕ_i to Schapery's model by minimizing the sum-of-squares error given by,

$$\delta = \sum_{i=1}^{M}[\alpha_{eff,\exp}(\phi_i) - \alpha_{eff,Schapery}(\phi_i)]^2 \quad \text{(Eq. 4.7)}$$
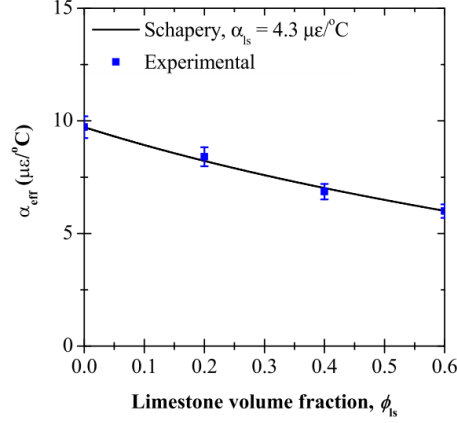
Figure 4.1: Effective thermal deformation coefficient α eff of cement pastes with crushed limestone inclusions as a function of limestone volume fraction ϕ ls ranging from 0 to 0.6 measured by Walker et al. [178] and predicted by Schapery's model using the retrieved value of $\alpha_{ls} = 4.3$ με/°C.

4.3 Results and discussion

The suggested method for retrieving the inclusion thermal deformation coefficient was validated by demonstrating its use on experimental data presented by Walker et al. [178] for cement pastes with crushed limestone inclusions with volume fraction ϕ ls ranging from 0 to 0.6. Additionally, the authors directly measured the thermal deformation coefficient of the cement paste alone as α_m = 9.72 με/°C, and that of the limestone as $\alpha_{ls} = 4.4$ με/°C by sawing specimens from the parent stone [178]. Here, the elastic modulus and Poisson's ratio of the limestone were taken as 31 GPa and 0.25, respectively [179]. Fig. 6 plots the experimentally measured effective thermal deformation coefficient α eff as a function of limestone volume fraction ϕ_{ls} [178]. The error bars correspond to an uncertainty of ± 5%. Fig. 6 also shows the best fit obtained with the Schapery model, corresponding to a retrieved value of $\alpha_{ls} = 4.3$ με/°C. This value of α ls agrees very well with that measured directly by the authors, thus demonstrating that our suggested approach can be

used to obtain accurate estimates of inclusion thermal expansion coefficients.
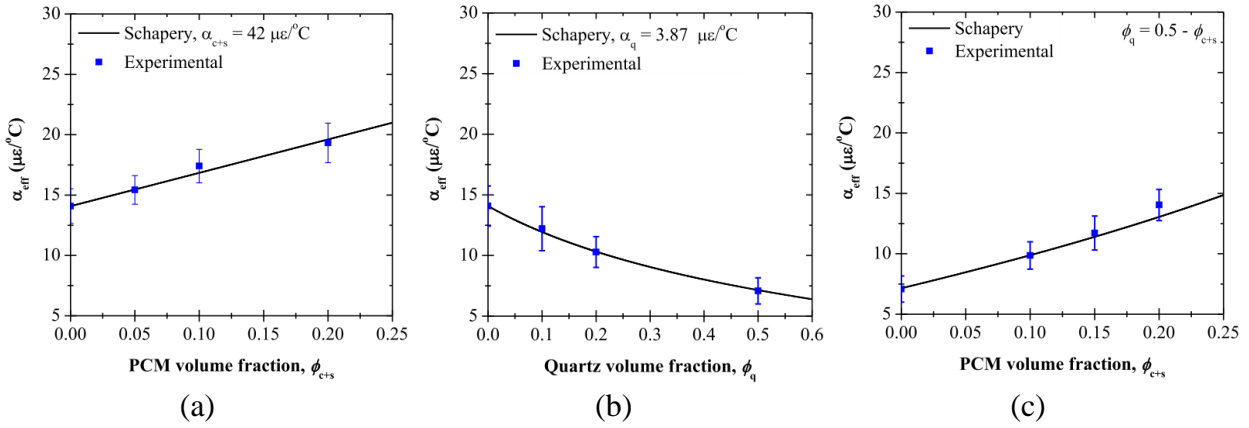
Figure 4.2: Experimentally measured thermal deformation coefficient α eff of cement pastes containing (a) microencapsulated PCM with ϕ_{c+s} ranging from 0 to 0.25, (b) quartz sand with ϕ_q ranging from 0 to 0.6, or (c) both microencapsulated PCM and quartz sand with ϕ_{c+s} ranging from 0 to 0.25 and $\phi_q + \phi_{c+s} = 0.5$.

4.3.1 Thermal deformation coefficient of PCM microcapsules

Figure 4.2(a) shows the experimentally measured effective deformation coefficient α eff of cement paste with microencapsulated PCM specimens as a function of microencapsulated PCM volume fraction ϕ_{c+s} ranging from 0 to 0.3. The error bars correspond to one standard deviation or 68% confidence interval of three measurements. Figure 4.2(a) also shows that α eff slightly increased with increasing ϕ_{c+s}, confirming that the thermal deformation coefficient of the PCM microcapsules was indeed larger than that of the cementitious matrix. The latter was measured to be $\alpha_m = 14.1$ µε/°C, corresponding to $\phi_{c+s} = 0$. The thermal deformation coefficient α_{c+s} of the PCM microcapsules was retrieved by least-square fitting the experimental measurements of α eff with Schapery's model, as outlined previously. In this case, the retrieved value of α_{c+s} was 42 µε/°C.

69

Interestingly, this value was similar to the thermal deformation coefficient of the MF shell, reported in the literature as $\alpha_s = 50$ µε/°C [180].

The PCM microencapsulation process is often carried out at elevated temperatures around 100 °C [181]. During subsequent cooling, the paraffinous core contracts more than the shell, i.e., $\alpha_c >> \alpha_s$, leaving some empty space in the PCM microcapsules at room temperature. Then, upon subsequent heating, the thermal deformation coefficient α_c of the core material has negligible impact on the thermal deformation coefficient α_{c+s} of the core-shell microcapsule, as the core is allowed to expand freely without exerting any stress on the shell. Therefore, the thermal deformation coefficient of the PCM microcapsule α_{c+s} is expected to be similar to that of the shell material for temperatures below 100 °C.

4.3.2 Thermal deformation coefficient of quartz sand inclusions

Figure 4.2(b) plots the experimentally measured effective thermal deformation coefficient α eff of cement mortar (i.e., cement paste with quartz sand inclusions) as a function of quartz inclusion volume fraction ϕ q ranging from 0 to 0.5. In this case, the low thermal deformation coefficient of the quartz sand caused α_{eff} to decrease with increasing quartz volume fraction ϕ_q. Here again, the thermal deformation coefficient of the quartz inclusions α_q was determined by least-square fitting the experimental measurements to the Schapery model. The elastic modulus E_q and Poisson's ratio v_q of quartz were taken, from the literature, as 73 GPa and 0.17, respectively [182]. Here, the resulting value of α_q was 3.9 µε/°C. Note that a wide range of thermal deformation coefficient values for quartz are reported in the literature, ranging from 0.5 µε/°C for silica (amorphous) [183] to 9.3 µε/°C for quartzite [184].
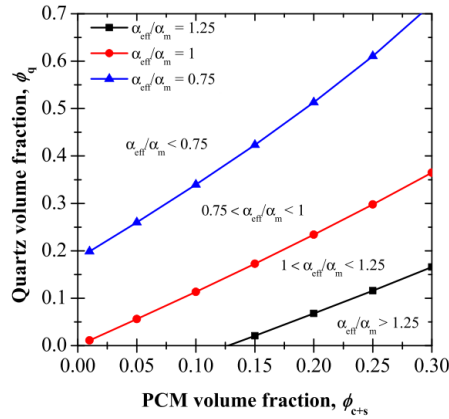
Figure 4.3: Required quartz sand volume fraction ϕ_q to ensure that the ratio α_{eff}/α_m of a PCM-mortar composite remains equal to 1.25, 1, or 0.75, plotted as a function of microencapsulated PCM volume fraction ϕ_{c+s} ranging from 0 to 0.3.

4.2.3 Mixed inclusion measurements

Figure 4.2(c) plots the experimentally measured effective thermal deformation coefficient α eff of microencapsulated PCM-mortar composite specimens with both PCM and quartz sand inclusions as a function of PCM volume fraction ϕ_{c+s} ranging from 0 to 0.5. Here, the total inclusion volume fraction was kept constant for all specimens such that $\phi_q + \phi_{c+s}$ =0.5. In particular, note that α eff for a specimen with ϕ_{c+s} =0.2 and ϕ_q =0.3 was measured to be 14.0 µε/°C while that of the cementitious matrix was measured earlier as α_m = 14.1 µε/°C. Thus, the effect of adding 20 vol.% microencapsulated PCM was "offset" by the addition of 30 vol.% quartz. Finally, Figure 4.2(c) shows the predictions of α eff by Schapery's model using the values of α_{c+s} and α_q retrieved from previous experiments (Figure 4.2a–b). Excellent agreement was found between α_{eff} predicted by the Schapery model and measured experimentally. These results demonstrate the ability of Schapery's model to account for the combined, independent effects of both inclusions on the effective thermal deformation coefficient of the mortars.

71

4.2.4 Design rule for thermal deformation equivalence in PCM-mortar composites

As shown in Figure 4.2, the addition of PCM microcapsules tends to increase the effective thermal deformation coefficient of the composite while the addition of quartz sand tends to decrease it. Therefore, one could "compensate" for the increase in α_{eff} caused by the addition of PCM microcapsules by adding an appropriate amount of quartz sand to maintain the ratio α_{eff}/α_m below some threshold. Figure 4.3 plots the required quartz sand volume fraction ϕ_q corresponding to a ratio α_{eff}/α_m equal to 1.25, 1, or 0.75, as a function of microencapsulated PCM volume fraction ϕ_{c+s} ranging from 0 to 0.3. Here, Schapery's model was used with the retrieved values of α_{c+s} and α_q to determine ϕ_q for each α_{eff}/α_m and ϕ_{c+s}. Note that for a desired ratio $\alpha_{eff}/\alpha_m < 0.75$, PCM volume fractions above ~0.25 are not feasible as they require a minimum total inclusion volume fraction $\phi_{c+s} + \phi_q$ of 0.85 or higher. Also, for an allowable ratio of $\alpha_{eff}/\alpha_m = 1.25$, no quartz sand is required for PCM volume fraction ϕ_{c+s} below 0.125.

4.3 Conclusion

This chapter examined the effect of microencapsulated PCMs and other particulate inclusions on the thermal deformation behavior of cementitious composites, and presented a convenient approach to estimate the thermal deformation coefficient of inclusions based on measured effective properties. The effective thermal deformation coefficient of cementitious microencapsulated PCM-composites was measured experimentally for cement paste and cement mortar with various volume fractions of quartz sand and microencapsulated PCM. The experimental measurements were used in conjunction with Schapery's model to retrieve the thermal deformation coefficient of PCM microcapsules and of quartz sand grains. The thermal deformation coefficient of the PCM

microcapsules was found to be near that of the shell material, due to the fact that the capsules might not be completely filled with PCM, thus leaving space inside for the PCM core to expand. Schapery's model was shown to predict accurately the effective thermal deformation coefficient of cementitious composite samples with a mixture of microencapsulated PCM and quartz sand inclusions based on the previously retrieved properties. Finally, a design rule was suggested for determining the amount of quartz sand required to offset the effect of the PCM microcapsules in increasing the thermal deformation coefficient of PCM-mortar composites. These results could be useful in modeling the thermal deformation behavior of pavement sections featuring microencapsulated PCMs for crack resistance.

Chapter 5 Clinkering-free cementation by fly ash carbonation

5.1 Background

Over the last century, for reasons of its low-cost and the widespread geographical abundance of its raw materials, ordinary portland cement (OPC) concrete has been used as the primary material for the construction of buildings and other infrastructure [4]. However, the production of OPC is a highly energy- and CO_2-intensive process. For example, at a production level of 4.2 billion tons annually [1] (equivalent to > 30 billion tons of concrete produced), OPC production accounts for approximately 3% of primary energy use and results in 9% of anthropogenic CO_2 emissions, globally [3]. Such CO_2 release is attributed to factors including: (i) the combustion of fuel required for clinkering the raw materials (i.e., limestone and clay) at 1450 °C, and, (ii) the release of CO_2 during the calcination of limestone in the cement kiln. As a result, around 0.9 tons of CO_2 are emitted per ton of OPC produced. Therefore, there is great need to reduce the CO_2 footprint of cement, and secure alternative solutions for 'cementation' as required for building and infrastructure construction.

Furthermore, there exist unique challenges associated with the production of electricity using coal (or natural gas) as the fuel source. For example, coal power is not only associated with significant CO_2 emissions (i.e., 30% of anthropogenic CO_2 emissions worldwide [185]), but also results in the accumulation of significant quantities of solid wastes such as fly ash (600 million tons annually; worldwide [10]). While considerable efforts have been made to replace OPC in the binder fraction of concrete by supplementary cementitious materials (SCMs) such as fly ash, the

extent of such utilization remains limited. For example, in the U.S., only around 45% of all fly ash produced annually is beneficially utilized to replace OPC in the concrete [11]. In spite of supportive frameworks [13], such limited use is due to factors including: (i) the presence of impurities including air-pollution control (APC) residues and unburnt carbon as a result of which some fly ashes are non-compliant (e.g., as per ASTM C618 [12]) for use in traditional OPC concrete, due to durability concerns [14], and, (ii) increasing cement replacement (i.e., fly ash dosage) levels to greater than 25 mass % is often associated with extended setting times and slow strength gain resulting in reduced constructability of the concrete [16].

Clearly, there is an immediate need to valorize or beneficially utilize ("upcycle") vapor and solid wastes associated with coal power production. However, given the tremendous scale of waste production, there is a need to secure upcycling opportunities of some prominence; e.g., within the construction sector wherein large-scale utilization of upcycled materials can be achieved. This condition could be satisfied if the "upcycled solution" is able to serve as an alternative to OPC (and OPC-concrete) so long as it is able to fulfill the functional and performance requirements of construction. Mineral carbonation (i.e., conversion of vapor phase CO_2 into a carbonaceous mineral; e.g., $CaCO_3$) has been proposed as a promising route to sequester CO_2 in alkaline minerals [17, 18]. In such a process, CO_2 is sequestered by chemical reaction of CO_2 streams with light-metal oxides to form thermodynamically stable carbonates; thus enabling permanent and safe storage of CO_2 [19]. While numerous studies have examined different alkaline waste streams to render cementation solutions – for example, coal combustion residues [31], municipal incinerator wastes [34], and wastes from iron and steel production [35] – the low production throughput, or severe operating conditions (i.e., high temperature and elevated CO_2 pressure) have made typical

75

approaches difficult to implement at a practical scale. Therefore, to synergize the utilization of two abundant by-products from coal-fired power plants (i.e., fly ash and CO_2 in flue gas), this study demonstrates clinkering-free cementation via fly ash carbonation. It is shown that Ca-rich fly ashes react readily with CO_2 under moist conditions, at atmospheric pressure and at sub-boiling temperatures. The influences of Ca availability in the fly ash, CO_2 concentration, and processing temperature on reaction kinetics and strength gain are discussed. Taken together, the outcomes create new opportunities for simultaneous valorization of solid wastes and CO_2, in an integrated process.

Table 5.1: The simple oxide composition of the fly ashes and OPC as determined using X-ray fluorescence (XRF).

Simple Oxide	Mass (%)		
	Ca-rich Fly Ash	Ca-poor Fly Ash	Type I/II OPC
SiO_2	35.44	53.97	20.57
Al_2O_3	17.40	20.45	5.19
Fe_2O_3	7.15	5.62	3.44
SO_3	2.34	0.52	2.63
CaO	26.45	12.71	65.99
Na_2O	1.90	0.57	0.17
MgO	5.73	2.84	1.37
K_2O	0.53	1.11	0.31
P_2O_5	0.95	0.30	0.08
TiO_2	1.19	1.29	0.26
Density (kg/m^3)	2760	2470	3150
Specific surface area (SSA, m^2/kg)	4292.6	616.8	442.6

Table 5.2: The mineralogical composition of the fly ashes and OPC as determined using quantitative X-ray diffraction (XRD) and Rietveld refinement.

Composition	Mass (%)		
	Ca-rich Fly Ash	Ca-poor Fly Ash	Type I/II OPC
Lime (CaO)	1.16	-	0.5
Periclase (MgO)	3.81	0.30	-
Quartz (SiO_2)	10.06	16.64	-
Calcite ($CaCO_3$)	0	0	4.60
Mullite ($Al_6Si_2O_{13}$)	0.86	5.08	-
Anhydrite ($CaSO_4$)	2.80	0.97	1.2
Gypsum($CaSO_4 \cdot 2H_2O$)	-	-	1.1
Magnetite (Fe_3O_4)	1.66	1.76	-
Merwinite ($Ca_3Mg(SiO_4)_2$)	6.98	-	-
Gehlenite ($Ca_2Al_2SiO_7$)	4.45	-	-
Ca_2SiO_4 (C2S)	4.93	-	18.00
$Ca_4Al_2Fe_2O_{10}$ (C4AF)	-	-	11.40
$Ca_3Al_2O_6$ (C3A)	8.03	-	6.30
Ca_3SiO_5 (C3S)	-	-	56.50
Amorphous	55.26	75.25	-

5.2. Materials and methods

5.2.1 Materials

A Class C (Ca-rich) fly ash and a Class F (Ca-poor) fly ash compliant with ASTM C618 [12] were used. An ASTM C150 [125] compliant Type I/II ordinary Portland cement (OPC) was used as a cementation reference. The bulk oxide compositions of the fly ashes and OPC as determined by X-ray fluorescence (XRF) are shown in Table 5.1. The crystalline compositions of the Ca-rich and Ca-poor fly ashes as determined using X-ray diffraction (XRD) are shown in Table 5.2. It should be noted that these two fly ashes were used since they represent typical Ca-rich and Ca-poor variants in the U.S., and since Ca content is expected to strongly influence the extent of CO_2 uptake and strength development of carbonated fly ash formulations.

5.2.2 Experimental methods

5.2.2.1. Particle size distribution and specific surface area

The particle size distribution (PSD) of OPC was measured using static light scattering (SLS) using a Beckman Coulter LS13-320 particle sizing apparatus fitted with a 750 nm light source. The solid was dispersed into primary particles via ultrasonication in isopropanol (IPA), which was also used as the carrier fluid. The complex refractive index of OPC was taken as $1.70 + 0.10i$ [186]. The highest uncertainty in the PSDs was around 6% based on six replicate measurements. From the PSD, the specific surface area (SSA, units of m2/kg) of OPC was calculated by factoring in its density of 3150 kg/m^3, whereas the SSAs of the fly ashes were determined by N_2-BET measurements, as previously reported (see Table 1) [187]. The surface area of the Ca-rich (Class C) fly ash is significantly overestimated by N_2 adsorption due to the presence of unburnt carbon [187]. However, based on kinetic analysis of reaction rates in OPC + fly ash + water systems, it can be inferred that the reactive surface areas of both the Ca-rich and Ca-poor fly ashes are similar to each other, and that of OPC. Further discussion regarding the surface areas of these materials can be found elsewhere [187].

5.2.2.2 Carbonation processing

Fly ash particulates were mixed with deionized (DI) water in a planetary mixer to prepare dense suspensions – i.e., pastes having w/s = 0.20 (w/s, water-to-solids ratio, mass basis) which offered sufficient fluidity such that they could be poured – following ASTM C192 [126]. The pastes were cast into molds to prepare cubic specimens with a dimension of 50 mm on each side. Following 2 hours of curing in the molds at temperature, $T = 45 \pm 0.2°C$ and relative humidity, $RH = 50 \pm 1\%$,

the specimens were demolded after which on account of evaporation they featured a reduced water content, i.e., w/s = 0.15, but were able to hold form; that is, they were "shape stabilized". At this time, the cubes were placed in a carbonation reactor, a schematic of which is shown in Figure 5.1.

Gas-phase CO_2 at atmospheric pressure with a purity of 99.5% ("pure CO_2") was used for carbonation. On the other hand, 99% pure N2 at atmospheric pressure was used as a control vapor that simulated ambient air (i.e., with a CO_2 abundance of around 400 ppm [188]). In addition, a simulated flue gas was created by mixing the pure N_2 and pure CO_2 streams to yield a vapor with 12% CO_2 (v/v) as confirmed using an Inficon F0818 gas chromatography (GC) instrument. Prior to contacting the samples, all vapor streams were bubbled into an open, water-filled container to produce a condensing environment in the reactor (i.e., as shown in Figure 5.1). Each of the vapors were contacted with the cubical samples at temperatures of $45 \pm 0.2°C$, $60 \pm 0.2°C$, and $75 \pm 0.2°C$.
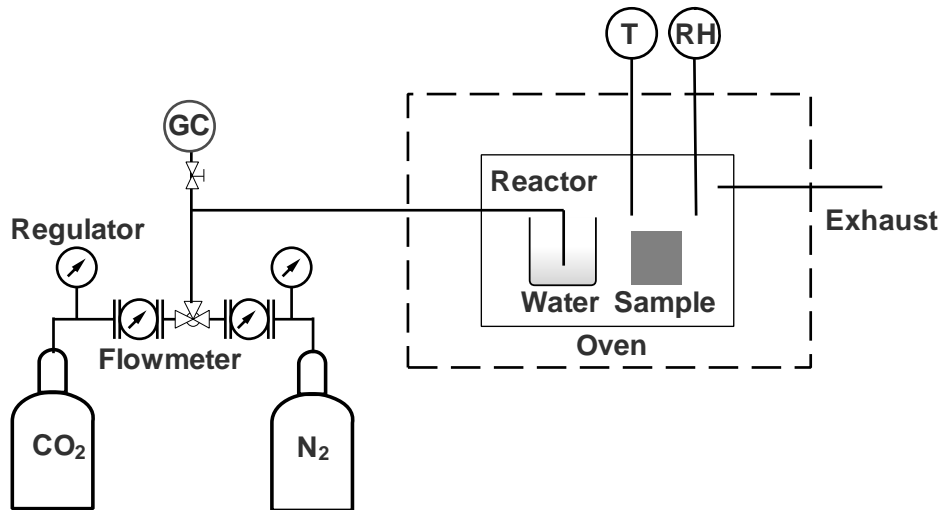
Figure 5.1: A schematic of the carbonation reactor showing the vapor streams, sample placement, and monitoring and control units (e.g., flow-meters, pressure regulators, temperature/relative humidity [T/RH] meters, and gas chromatograph (GC)).

5.2.2.3 Compressive strength

The compressive strengths of the fly ash cubes (i.e., both control samples, and those exposed to CO_2) were measured at 1 day intervals following ASTM C109 [189] for up to 10 days. All strength data reported herein are the average of three replicate specimens cast from the same mixing batch. For comparison, the compressive strengths of neat OPC pastes prepared at w/s = 0.30, 0.40, 0.50, and 0.60 were measured after 1, 3, 7, and 28 days of immersion and curing in a $Ca(OH)_2$-saturated solution ("limewater") at $23 \pm 1°C$.

5.2.2.4 CO_2 uptake by fly ash formulations

CO_2 uptake due to carbonation of the fly ashes was quantified by two methods: (i) a mass-gain method, and, (ii) thermogravimetric analysis (TGA). The mass-gain method was used to estimate the average CO_2 uptake of the bulk cubic specimen from the mass gain of three replicate cubes following CO_2 contact as given by Equation (5.1),

$$W = \frac{m_t - m_i}{m_a} \qquad \text{Eq. (5.1)}$$

where, w (g/g) is the CO_2 uptake of a given cube, m_t (g) is the mass of the specimen following CO_2 contact over a period of time t (days), m_i (g) is the initial mass of the specimen, and m_a (g) is the mass of dry fly ash contained in the specimen (i.e., estimated from the mixture proportions). It should be noted that carbonation is an exothermic reaction; thus it could result in the evaporation of water from the sample. However, since herein, curing was carried out in a near-condensing atmosphere, mass measurements before and after carbonation revealed no mass loss due to (moisture) evaporation. The ratio of CO_2 uptake at time t to that assessed at the end of the experiment (i.e., CO_2 uptake fraction, α) is given by Equation (5.2),

$$\alpha = \frac{m_t - m_i}{m_f - m_i} \qquad\qquad \text{Eq. (5.2)}$$

where, m_f (g) is the final mass of a given cubical specimen following 10 days of CO_2 exposure.

TGA was used to determine the extent of CO_2 uptake at different depths in the fly ash cubes, from the surface to the center in 5 mm increments. To accomplish so, cubes were sectioned longitudinally using a hand saw. Then, samples were taken from the newly exposed surface along a mid-line using a drill at a sampling resolution of around ± 1 mm. The dust and debris obtained during drilling, at defined locations along the center-line, were collected and pulverized for thermal analysis in a PerkinElmer STA 6000 simultaneous thermal analyzer (TGA/DTG/DTA) provided with a Pyris data acquisition interface. Herein, ≈ 30 mg of the powdered sample that passed a 53 µm sieve was heated under UHP-N_2 gas purge at a flow rate of 20 mL/min and heating rate of 10 °C/min in pure aluminum oxide crucibles over a temperature range of 35-to-980 °C. The mass loss (TG) and differential weight loss (DTG) patterns acquired were used to quantify the CO_2 uptake by assessing the mass loss associated with calcium carbonate decomposition in the temperature range 550 °C $\leq$ T $\leq$ 900 °C [3]. The mass-based method of assessing the extent of carbonation and the spatially resolved TGA method indicate, on average, similar levels of carbonation, as noted below. In addition, to visually check for carbonation in the fly ash paste, and the depth at which it reaches over time, the commonly used phenolphthalein test was carried out [190, 191]. Specifically, fly ash cubes after carbonation for different times were cut at the middle cross-section, and 1% phenolphthalein ($C_{20}H_{14}O_4$) solution was sprayed on the exposed surface to see if there is any change in color.

5.2.2.5 X-ray diffraction (XRD)

To qualitatively examine the effects of carbonation, the mineralogical compositions of fly ash mixtures before and after CO_2 exposure were assessed using X-ray diffraction. Here, entire fly ash cubes were crushed and ground into fine powders, which were scanned from 5-to-70° (2θ) using a Bruker-D8 Advance diffractometer in a θ-θ configuration with Cu-Kα radiation (λ=1.54 Å) fitted with a VANTEC-1 detector. Representative powder samples were examined to obtain averaged data over the whole cube. The diffractometer was run in continuous mode with an integrated step scan of 0.021° (2θ). A fixed divergence slit of 1.00° was used during X-ray data acquisition. To minimize artifacts resulting from preferred orientation and to acquire statistically relevant data, the (powder) sample surface was slightly textured and a rotating sample stage was used.

5.2.2.6 Scanning electron microscopy (SEM)

The morphology and microstructure of the non-carbonated and carbonated fly ash mixtures were examined using a field emission scanning electron microscope provisioned with an energy dispersive X-ray spectroscopy detector (SEM-EDS; FEI NanoSEM 230). First, hardened samples were sectioned using a hand saw. Then, these freshly exposed sections were taped onto a conductive carbon adhesive and then gold-coated to facilitate electron conduction and minimize charge accumulation on the (otherwise) non-conducting surfaces. Secondary electron (SE) images were acquired at an accelerating voltage of 10 kV and a beam current of 80 pA.

5.2.3 Thermodynamic simulations of phase equilibria and CO_2 uptake

To better understand the effects of carbonation on the mineralogy and mechanical property development of carbonated fly ashes, thermodynamic calculations were carried out using GEM-

Selektor, version 2.3 (GEMS, see Kulik et al. [192-194]). GEMS is a broad-purpose geochemical modeling code which uses Gibbs energy minimization criteria to compute equilibrium phase assemblages and ionic speciation in a complex chemical system from its total bulk elemental composition. Chemical interactions involving solid phases, solid solutions, and the aqueous electrolyte(s) are considered simultaneously. The thermodynamic properties of all the solid and the aqueous species were sourced from the GEMS-PSI database, with additional data for the cement hydrates sourced from elsewhere [192, 193]. The Truesdell-Jones modification of the extended Debye-Hückel equation (see Eq. 5.3) was used to account for the effects of solution non-ideality:

$$\log \gamma_j = \frac{-Az_j^2 \sqrt{I}}{1+B\alpha_j \sqrt{I}} + bI + \log_{10} \frac{x_{jw}}{X_w} \qquad \text{Eq. (5.3)}$$

where, γ_j is the activity coefficient of jth ion (unitless); z_j is the charge of jth ion, α_j is the ion-size parameter (i.e., effective hydrated diameter of jth ion, Å), A ($kg^{1/2} \cdot mol^{-1/2}$) and B ($kg^{1/2} \cdot mol^{-1/2} \cdot m^{-1}$) are pressure, p- and T-dependent Debye-Hückel electrostatic parameters [192], b is a semi-empirical parameter that describes short-range interactions between charged aqueous species in an electrolyte, I is the molal ionic strength of the solution (mol/kg), x_{jw} is the molar quantity of water, and X_w is the total molar amount of the aqueous phase. It should be noted that this solution phase model is suitable for $I \leq 2.0$ mol/kg beyond which, its accuracy is reduced [195]. In the simulations, Ca-rich and Ca-poor fly ashes were reacted with water in the presence of a vapor phase consisting of: (a) air (≈ 400 ppm CO_2), (b) 12 % CO_2 (88 % N_2, v/v), and, (c) 100 % CO_2 (v/v), respectively. The calculations were carried out at T = 75 °C and p = 1 bar. The solid phase balance was calculated as a function of degree of reaction of the fly ash, until either the pore solution is exhausted (i.e., constraints on water availability) or the fly ash is fully reacted.

5.3. Results and discussion

5.3.1. Carbonation strengthening

Figure 5.2(a) shows the compressive strength development as a function of time for Class C (Ca-rich) and Class F (Ca-poor) fly ash pastes carbonated in pure CO_2 at 75 °C. The Ca-rich fly ash formulations show rapid strength gain following exposure to CO_2, especially during the first 6 days. For example, after only 3 days of CO_2 exposure, the carbonated formulation achieves a strength of 25 MPa, whereas a strength on the order of 35 MPa is produced after 7 days of CO_2 exposure. On the other hand, as also seen in Figure 5.2(a), when the Ca-rich formulation was exposed to N_2 at the same temperature, RH, and gas flow rate (i.e., serving as a "control" system), a strength of only 15 MPa develops after 7 days, due to limited reaction of a small quantity of readily soluble Ca-compounds with any available silica, water, and ambient CO_2. As such, the level of strength developed in the control system is less than half of that of the carbonated (Ca-rich) fly ash formulation. As a reference, more than 65% of all concretes produced globally (i.e., primarily using OPC as the cementitious reactant) feature a compressive strength of 30 MPa or less. The extent of strength development noted in the carbonated system is significant as it suggests that carbonated binders can fulfill code-based (strength) criteria relevant to structural construction (i.e., $\geq$ 30 MPa as per ACI 318 [159]).
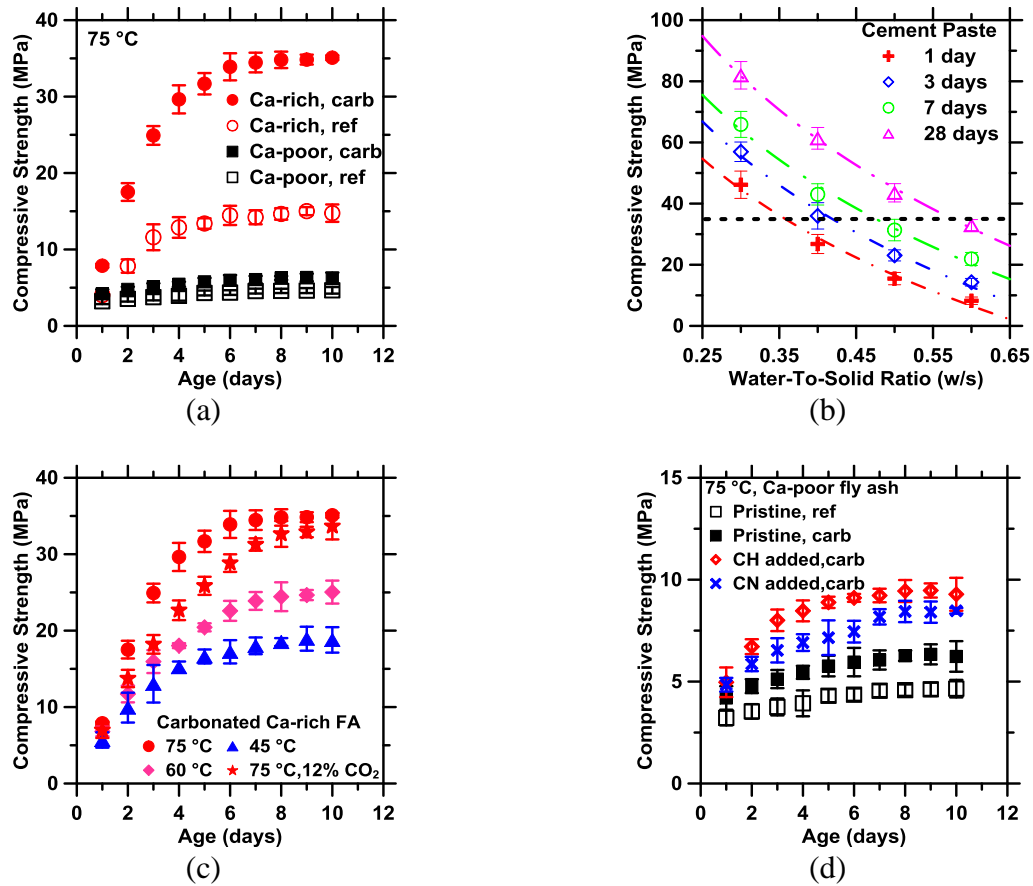
Figure 5.2: The evolution of compressive strengths of: (a) Ca-rich and Ca-poor fly ash pastes following CO_2 exposure at 75 °C, and the control samples (i.e., exposed to pure N2) for comparison, as a function of (carbonation) time, (b) hydrated OPC pastes at different ages after curing in saturated limewater at 23°C, as a function of w/s. The dashed black line shows the compressive strength of a Ca-rich fly ash formulation following its exposure to CO_2 at 75 °C for 7 days, (c) Ca-rich fly ash pastes carbonated at different temperatures following exposure to 99.5 % CO_2 (v/v), and simulated flue gas (12 % CO_2, v/v), as a function of time, and, (d) Ca-enriched (i.e., with added $Ca(OH)_2$, or dissolved $Ca(NO_3)_2$) Ca-poor (i.e., Class F) fly ash pastes following CO_2 exposure at 75 °C, as a function of time. The compressive strengths of the pristine Ca-poor fly ash with and without carbonation are also shown for comparison.

To provide a point of reference, the compressive strengths of neat-OPC formulations were measured across a range of w/s. For example, Figure 5.2(b) shows that the compressive strength of a Ca-rich fly ash formulation following exposure to CO_2 for 7 days at 75°C – around 35 MPa – is equivalent to that of an OPC formulation prepared at w/s ≈ 0.50 and cured in saturated limewater at 23 °C over the same time period. It is important to note, however, that the fly ash formulations show a significantly reduced rate of strength gain after 7 days – likely due to the consumption of readily available species (Ca, Mg) that can form carbonate compounds. On the other hand, OPC systems show a strength increase on the order of 30% from 7 days to 28 days (i.e., a common aging period that is noted in building codes [159]) of maturation across all w/s.

Furthermore, Figure 5.2(a) also indicates that, unlike the "carbonation strengthening" seen in Ca-rich fly ash formulations, Ca-poor fly ash systems showed a strength of ≤ 7 MPa even after 10 days of carbonation, a gain of only ≤ 2 MPa following CO_2 exposure vis-à-vis a system cured in a N_2 atmosphere. This suggests that, in general, Ca-poor fly ashes feature little potential for CO_2 mineralization or strength gain following CO_2 exposure because the [Ca, Mg] available therein is either insufficient or not easily available for reaction (e.g., see Figure 5.4). This suggests that carbonation strengthening is dominantly on account of the presence of reactive, alkaline compounds, i.e., Ca- and Mg-bearing compounds (e.g., CaO, MgO, etc.), and Ca present in the fly ash glass (see Tables 5.1 and 5.2), that can react with CO_2. It should also be noted that Ca-rich fly ashes contain cementitious phases such as Ca_2SiO_4, $Ca_2Al_2SiO_7$, and $Ca_3Al_2O_6$ (see Table 5.2), which upon hydration (and carbonation) form cementitious compounds such as the calcium-silicate-hydrates (C-S-H), or in a CO_2 enriched atmosphere, calcite and hydrous silica (e.g., see Figures 5.3-5.4). As a result, when such Ca-rich fly ash reacts with CO_2 in a moist, super-ambient

(i.e., but sub-boiling) environment, carbonate compounds such as calcite ($CaCO_3$) and magnesite ($MgCO_3$) are formed as shown in Figures 5.3-5.4. This is not observed in the Ca-poor fly ash due to both its much lower total [Ca+Mg] content and their lower reactivity [196] (e.g., see Figures 5.3-5.4, which shows little if any formation of carbonate minerals following CO_2 exposure in the Ca-poor fly ash formulation). It should be noted that while the extents of reaction of the fly ashes (i.e., Ca-rich or Ca-poor) were not explicitly assessed, it is expected that their degree of reaction is ≤ 25 % for the short reaction times and over the temperature conditions of relevance to this study [197].

In general, upon contact with water, the reactive crystalline compounds (e.g., CaO, $Ca_3Al_2O_6$, etc.) present in a Ca-rich fly ash are expected to rapidly dissolve in the first few minutes. As the pH systematically increases, with continuing dissolution, alkaline species including Na, K, Ca are expected to be released progressively from the glassy compounds [198]. This is expected to result in the development of a silica-rich rim on the surfaces of fly ash particles [199]. Pending the presence of sufficient solubilized Ca, and in the presence of dissolved CO_2, calcite is expected to form rapidly on the surfaces of leached (and other) particles, thereby helping proximate particles to adhere to each other as the mechanism of carbonation strengthening [200] (e.g., see Figures 5.3-5.5). This is additionally helped by the liberation of Ca, and Si from the anhydrous fly ash, whose reaction with water results in the formation of hydrated calcium silicates (see Figures 5.3-5.4), calcite and hydrous silica. This is significant as the hydrated calcium silicates and calcite are known to feature a mutual affinity for attachment and growth [22, 23, 26].
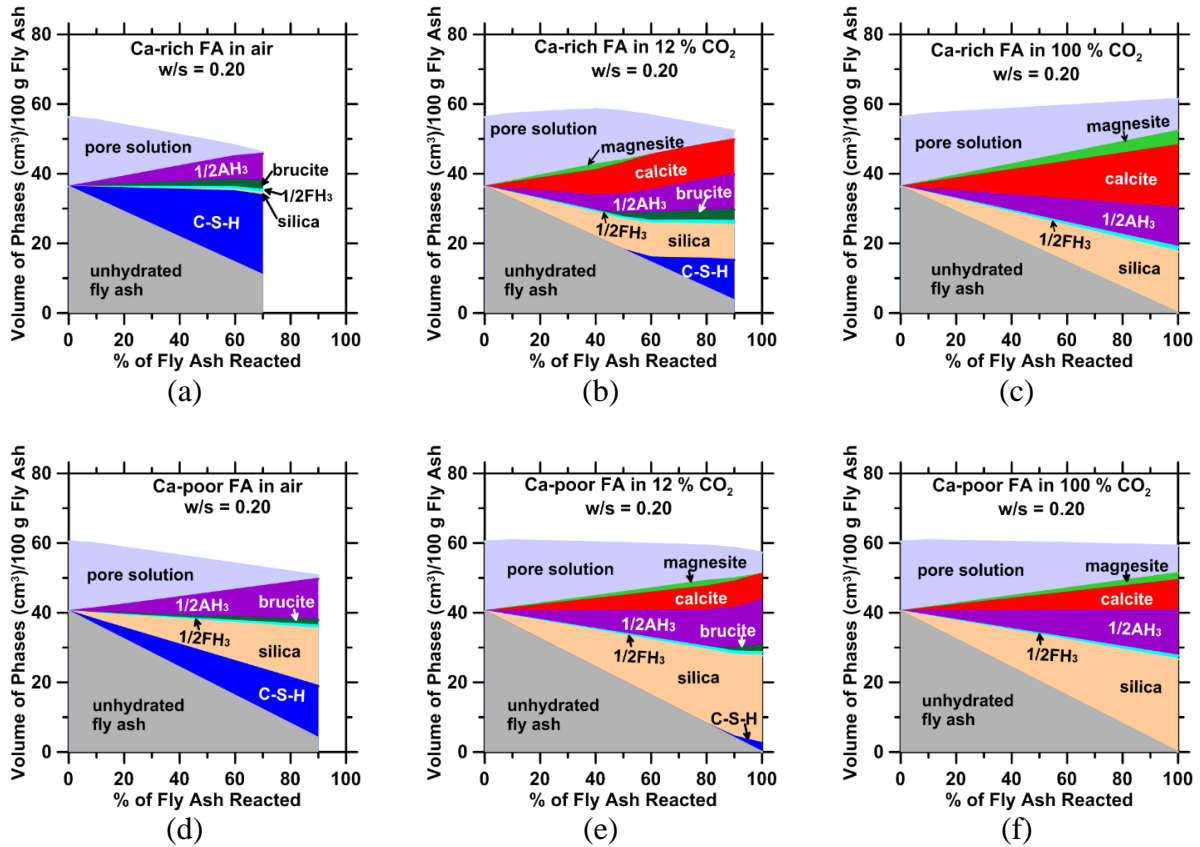
Figure 5.3: The GEMS-calculated solid phase balances as a function of the extent of fly ash reaction for Ca-rich and Ca-poor fly ash in the presence of a gas-phase consisting of: (a, d) air, (b, e) 12 % CO_2 (i.e., simulated flue gas environment), and (c, f) 100 % CO_2 at T = 75 °C and p = 1 bar for w/s = 0.20. Here, $1/2FH_3$ = $Fe(OH)_3$, $1/2AH_3$ = $Al(OH)_3$, and C-S-H= calcium silicate hydrate. The solid phase balance is calculated until the pore solution is exhausted, or the fly ash reactant is completely consumed.

Of course, up on extended exposure to CO_2, the hydrated calcium silicates would decompose to form calcite, and hydrous silica (as shown in Figure 5.3) which have themselves been noted to offer cementation [201]. Similar mechanisms of carbonation strengthening have been noted following the reaction of low-rank, synthetic calcium silicates with CO_2 [202-204]. The systematic

formation of mineral carbonates in this fashion induces: (i) cementation, e.g., in a manner analogous to that observed in mollusks, and sea-shells, that binds proximate particles to each other via a carbonate network, or carbonate formation which ensures the cementation of sandstones [205, 206], and, (ii) an increase in the total volume of solids formed which results in a densification of microstructure, while ensuring CO_2 uptake (e.g., see Vance et al. [5] and Figure 5.3 for scenarios wherein reaction with CO_2 results in an increase in solid volume).
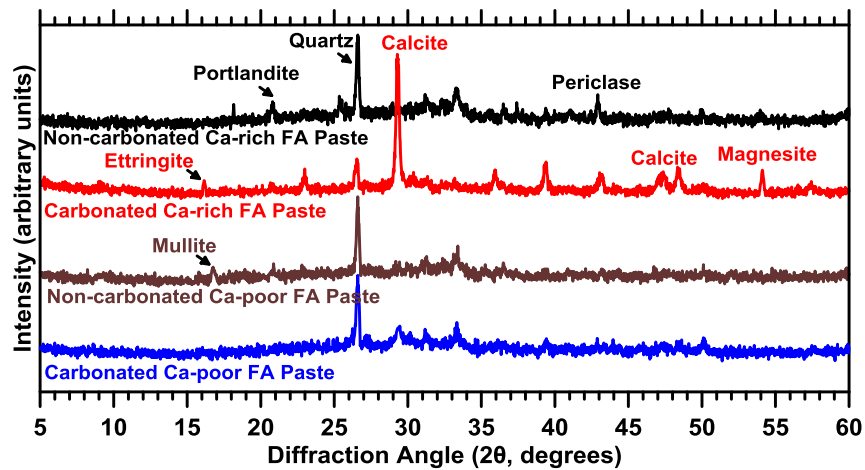
Figure 5.4: Representative XRD patterns of Ca-rich and Ca-poor fly ash formulations before and after exposure to CO_2 at 75 °C for 10 days. The Ca-poor fly ash shows no change in the nature of compounds present following exposure to CO_2.

Coming back to ascertaining the ability of flue gas from coal-fired power plants, as is, to carbonate fly ash, the Ca-rich fly ash was carbonated in a 12% CO_2 atmosphere (v/v) at 75°C. As noted in Figure 5.2(c) and Figure 5.3(b, e), CO_2 present in flue gas at relevant concentrations can readily carbonate fly ash and ensure strength gain, albeit at a slightly reduced rate vis-à-vis pure CO_2 exposure. This reduced rate of strength gain (and carbonation) is on account of the lower abundance of dissolved CO_2 in the vapor phase, and hence in the liquid water following Henry's

89

law [206]. However, it should be noted that after 10 days of exposure to simulated flue gas, the strength of the Ca-rich fly ash formulation was equivalent to those cured in a pure-CO_2 atmosphere (Figure 5.2c). This is significant, as it demonstrates a pathway for clinkering-free cementation by synergistic use of both fly ash and untreated flue gas of dilute CO_2 concentrations sourced from coal-fired power plants.

To better assess the potential for valorization of diverse industrial waste streams of CO_2, the effects of reaction temperature on carbonation and strength gain were further examined. As an example, flue gas emitted from coal-fired power plants features an exit temperature (T_E) on the order of $50°C \leq TE \leq 140°C$ to minimize fouling and corrosion, and to provide a buoyant force to assist in the evacuation of flue gas through the stack [207]. Since heat secured from the flue gas is the primary means of thermal activation of reactions, the carbonation of Ca-rich fly ash formulations and their rate of strength gain were examined across a range of temperatures as shown in Figure 5.2(c). Expectedly, the rate of strength gain increases with temperature. This is on account of two factors: (i) elevated temperatures facilitate the dissolution of the fly ash solids, and the leaching of the fly ash glass, and, (ii) elevated temperatures favor the drying of the fly ash formulation, thereby easing the transport of CO_2 into the pore structure which facilitates carbonation. It should however be noted that the solubility of CO_2 in water decreases rapidly at temperatures in excess of 60°C. While in a closed system this may suppress the rate of carbonation, the continuous supply of CO_2 provisioned herein, in a condensing atmosphere ensures that no retardation in carbonation kinetics is observed despite an increase in temperature. It should also be noted that carbonation reactions are exothermic. Therefore, increasing the reaction temperature is expected to retard reaction kinetics (i.e., following Le Chatelier's principle); unless heat were to be carried away from the

carbonating material. Of course, such exothermic heat release would further decrease the solubility of CO_2 in water by enhancing the local temperature in the vicinity of the reaction zone. As such, several processes including the dissolution of the fly ash solids, leaching of the fly ash glass, and the transport of solubilized CO_2 through the vapor phase and water present in the pore structure influence the rate of fly ash carbonation.

To more precisely isolate the role of Ca content of the fly ash, further experiments were carried out wherein $Ca(OH)_2$ or $Ca(NO_3)_2$ were added to the Ca-poor fly ash in order to produce equivalent bulk Ca contents to the Ca-rich fly ash. Here, it should be noted that while $Ca(OH)_2$ was added as a solid that was homogenized with the fly ash, $Ca(NO_3)_2$ was solubilized in the mixing water. The results shown in Figure 5.2(d) highlight that although the $Ca(OH)_2$- and $Ca(NO_3)_2$-enriched Ca-poor fly ash experienced substantial strength increases (≈ 35 %) following carbonation as compared to the pristine Ca-poor fly ash, the strengths were still far lower than that of the Ca-rich fly ash (see Figure 5.2a). Nevertheless, the enhancement in strength observed in the Ca-poor formulations is postulated to be on the account of both: (a) the pozzolanic reaction between the added Ca source and silica liberated from the fly ash resulting in the formation of calcium silicate hydrates (C-S-H), and, (b) the formation of calcite and (hydrous) silica gel by the carbonation-decomposition of C-S-H, and by direct reaction of solubilized Ca with aqueous carbonate species [208]. The carbonation of C-S-H has been observed to result in the release of free water and the formation of a silica gel with reduced water content [208-210], as is also predicted by simulations (see Figure 5.3). However, such water release (i.e., an increase in the porosity) does not appear to be the cause of the reduced strengths obtained in the Ca-poor fly ash formulations. Rather, it appears as though the presence of reactive Ca intrinsic to the fly ash (glass), and the formation of a silica-rich surface

91

layer to which $CaCO_3$ can robustly adhere results in higher strength development in Ca-rich fly ash formations. Given the inability of Ca-poor fly ashes to offer substantial carbonation-induced strength gain, the remainder of the study focuses on better assessing the effects of CO_2 exposure on Ca-rich fly ash formulations.

Indeed, the electron micrographs shown in Figure 5.5 offer additional insights into morphology and microstructure development in Ca-rich fly ash formulations following exposure to N_2 and CO_2 at 75 °C for 10 days. First, it is noted that the uncarbonated fly ash formulations show a loosely packed microstructure with substantial porosity (Figure 5.5a). Close examination of a fly ash particle shows a "smooth" surface (e.g., see Figure 5.5b), although alkaline species might have been leached from the particle's surface. In contrast, Figures 5.5(c-d) reveal the formation of a range of crystals that resemble "blocks and peanut-like aggregates" on the surfaces of Ca-rich fly ash particles – post-carbonation. XRD (Figure 5.4) and SEM-EDS analyses of these structures confirm their composition as that of calcium carbonate (calcite: $CaCO_3$). These observations are in agreement with those of Fernandez-Diaz at al. [211] and Vance et al. [5], who reported such altered morphologies of calcite crystals. Nevertheless, the role of calcite and silica gel that forms in these systems is significant in that such gels serve to reduce the porosity, and effectively bind the otherwise loosely packed fly ash particles (Figure 5.5a), thereby ensuring "carbonation strengthening". Expectedly, Ca-poor fly ash particles do not show the formation of carbonation products on their surfaces, in spite of CO_2 exposure (see Figure 5.5e). Furthermore, the addition of supplemental portlandite to Ca-poor systems results in only a marginal level of carbonation product formation on fly ash particle surfaces (see Figure 5.5f). These observations highlight the critical role of not only the Ca (and Mg)-content, but also potentially their spatial distribution on

microstructure and strength development in carbonated fly ash systems.

(a)　　　　　　　　　　　(b)　　　　　　　　　　　(c)

(d)　　　　　　　　　　　(e)　　　　　　　　　　　(f)
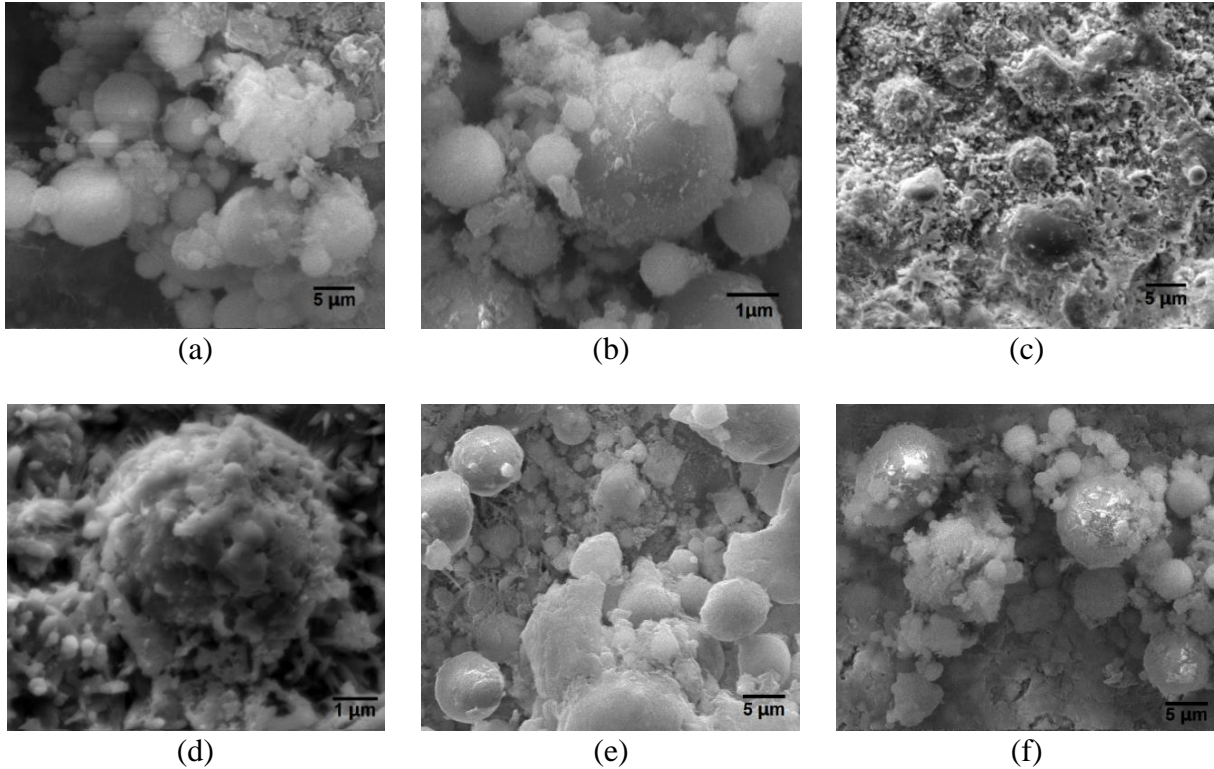
Figure 5.5: Representative SEM micrographs of: (a) a Ca-rich fly ash formulation following exposure to N_2 at 75 °C for 10 days; a magnified image highlighting the surface of a fly ash particle is shown in (b), (c) a Ca-rich fly ash formulation following exposure to pure CO_2 at 75 °C for 10 days; a magnified image highlighting the surface of a carbonated fly ash particle wherein carbonation products in the form of calcite are clearly visible on the particle surface is shown in (d), (e) a Ca-poor fly ash formulation following exposure to pure CO_2 at 75 °C for 10 days, and (f) $Ca(OH)_2$-enriched Ca-poor fly ash formulation following exposure to pure CO_2 at 75 °C for 10 days wherein the limited formation of calcite is noted on particle surfaces.

5.3.2. Carbonation kinetics

Figure 5.6(a) shows CO_2 uptake by the Ca-rich fly ash formulation as determined by thermal analysis (i.e., by tracking the decomposition of $CaCO_3$) as a function of time across a range of

93

curing temperatures. Expectedly, both the rate and extent of CO_2 uptake, at a given time, increase with temperature. Although the terminal CO_2 uptake (i.e., which is a function of chemical composition) is expected to be similar across all conditions, this was not observed over the course of these experiments – likely due to kinetic limitations on dissolution, and the subsequent carbonation of the fly ash solids. Nevertheless, a linear correlation between compressive strength evolution and the CO_2 uptake of a given mixture is noted (see Figure 5.6b) – for both Ca-rich and Ca-poor fly ash formulations. Significantly, a strength gain on the order of 3.2 MPa per unit mass of fly ash carbonated is realized. It should be noted that the Ca-rich fly ash composition examined herein – in theory – has the potential to take-up around 27.1 mass % CO_2 assuming that all the CaO and MgO therein would carbonate (e.g., see XRF composition in Table 5.1). Based on the correlation noted in Figure 5.6(b), realizing the highest possible maximum carbonation level – i.e., at thermodynamic equilibrium would produce a terminal strength on the order of 86 MPa independent of the prevailing reaction conditions (i.e., CO_2 concentration, and temperature). It should be noted however that achieving this terminal level of CO_2 uptake is unlikely due to the time-dependent: (i) formation of carbonate films of increasing thickness which hinders access to the reactants, and, (ii) formation of a dense microstructure that hinders the transport of CO_2 through the liquid phase to reactive sites.

Broadly, mineral carbonation, i.e., the formation of calcite and/or magnesite, takes the form of irreversible heterogeneous solid-liquid-gas reactions [212-215]. In the case of Ca-rich fly ashes, it includes the processes of dissolution and hydration of the Ca-rich compounds including β-Ca_2SiO_4, Ca-rich glasses, CaO, $Mg(OH)_2$, $Ca(OH)_2$, etc., and the subsequent precipitation of $CaCO_3$ and $MgCO_3$ from aqueous solution; e.g., see Table 5.2, Figure 5.3 and the following

reactions:

$$CO_2(g) + H_2O(l) \leftrightarrow H_2CO_3(aq) \leftrightarrow H^+(aq) + HCO_3^-(aq)$$ Eq. (5.4)

$$HCO_3^-(aq) \leftrightarrow H^+(aq) + CO_3^{2-}(aq)$$ Eq. (5.5)

$$XO(s) + H_2O(l) \rightarrow X(OH)_2(s) \rightarrow X^{2+}(aq) + 2OH^-(aq), where\ X = Ca, Mg$$ Eq. (5.6)

$$X_2SiO_4(s) + 4H^+(aq) \rightarrow 2X^{2+}(aq) + SiO_2(s) + 2H_2O(l)$$ Eq. (5.7)

$$X^{2+}(aq) + CO_3^{2-}(aq) \rightarrow XCO_3(s)$$ Eq. (5.8)
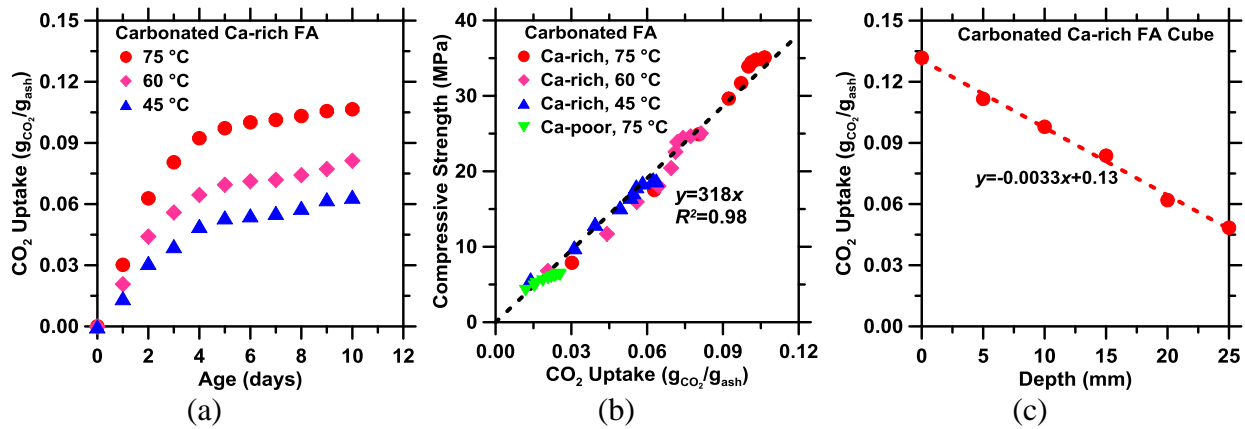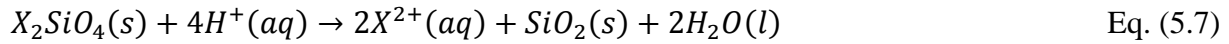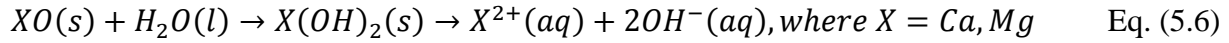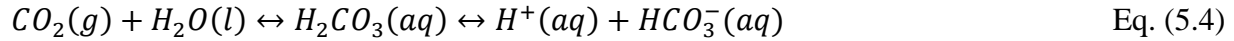
Figure 5.6: (a) The CO_2 uptake (normalized by the mass of Ca-rich fly ash in the formulation) as a function of time for samples exposed to pure CO_2 at different isothermal temperatures. The amount of CO_2 uptake was estimated using the mass-based method. (b) The compressive strength of the Ca-rich and Ca-poor fly ash samples as a function of their CO_2 uptake following exposure to pure CO_2 at different temperatures for 10 days. The data reveals a strength gain rate of 3.2 MPa per unit mass of fly ash that has reacted (carbonated). CO_2 uptake was estimated using the mass-based method. (c) The CO_2 uptake of a Ca-rich fly ash formulation as a function of depth. The macroscopic sample consisted of a cube (50 mm x 50 mm x 50 mm) that was exposed to pure CO_2 at 75°C for 10 days. Herein, CO_2 uptake was assessed by thermal analysis (TGA).

Simultaneous to the dissolution and hydration of the solids, vapor phase CO_2 will dissolve in water, as dictated by its equilibrium solubility (i.e., as described by Henry's law [206]) at the relevant pH and temperature [29]. As ionized species from the reactants and dissolved CO_2 accumulate in the liquid phase, up on achieving supersaturation – often described by the ratio of the ion activity product to the solubility product for a given compound, e.g., calcite – precipitation occurs thereby reducing the supersaturation level. Ca- or Mg-bearing compounds in the fly ash would continue to dissolve as the solution remains under-saturated with respect to these phases due to the precipitation of carbonates, ensuring calcite and/or magnesite formation until the readily available quantity of these reactant compounds is exhausted and the system reaches equilibrium. It should be noted that in fly ash mixtures, wherein the abundance of alkaline compounds is substantial, i.e., a large Ca/alkaline-buffer exists, the dissolution of gas-phase CO_2 whose dissolution would otherwise acidify the pore solution has little if any impact on altering the solution pH.

It should furthermore be noted that, in the case of the fly ash cubes tested for compressive strength (i.e., following ASTM C109), or in the case of fly ash particulates (e.g., see Figure 5.5, and associated thin-section analysis; not shown), in general, carbonation reactions proceed inward from the surface to the interior and the surface reacts faster than the bulk (e.g., see Figure 5.6c) [216]. The kinetics of such reactions can be analyzed by assessing how the rate of conversion of the reactants is affected by process variables [217]. For example, as noted above in Figure 5.6(a), it is seen that carbonation occurs rapidly at short reaction times, and its rate progressively decreases with increasing reaction time. This nature of rapid early-reaction, followed by an asymptotic reduction in the reaction rate at later times has also been confirmed by carbonation depth test using 1% phenolphthalein solution, an organic compound widely used as a pH indicator, as shown in

Figure 5.7.

(a)   (b)   (c)

(d)   (e)   (f)
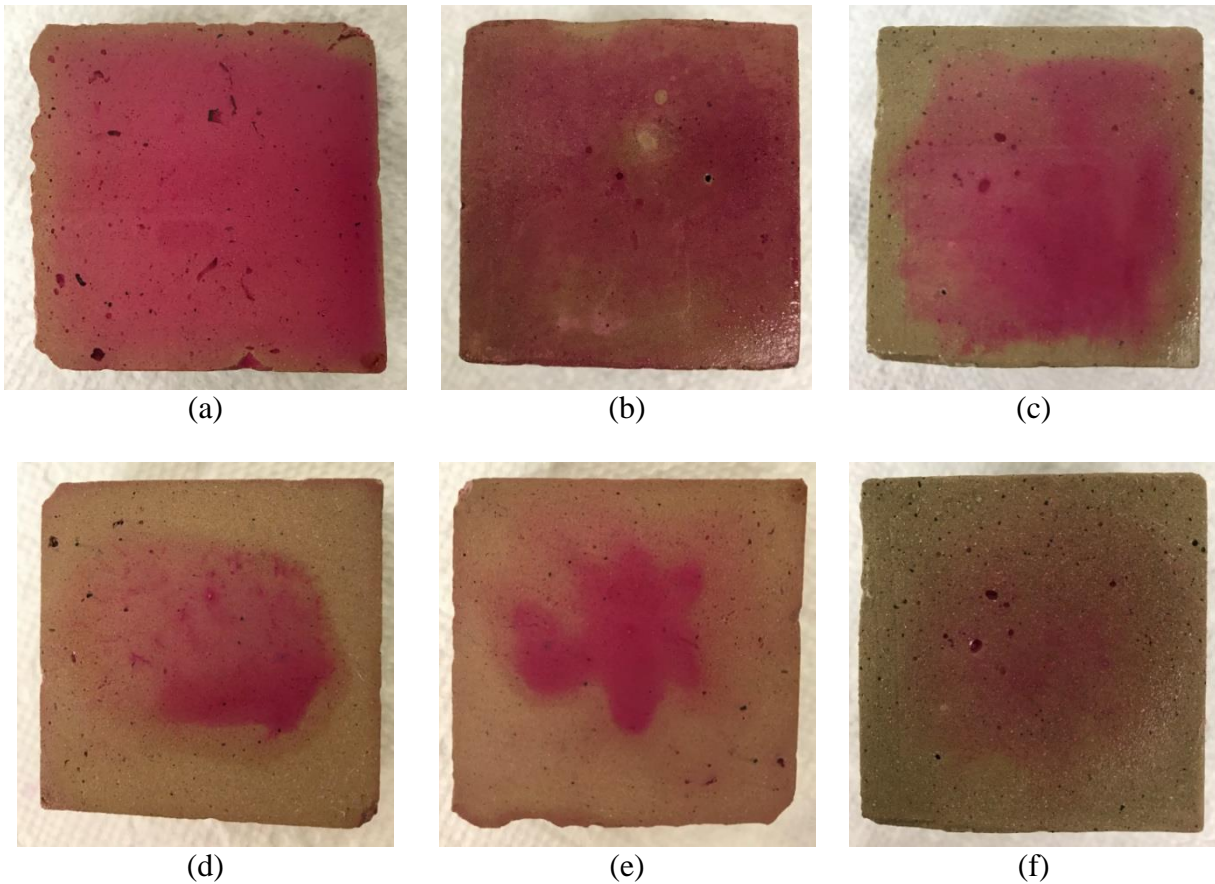
Figure 5.7: Middle cross-sections of fly ash cubes spayed with 1% phenolphthalein solution without carbonation (a); and after carbonation at 75 °C for 1 day (b), 2 days (c), 3 days (d), 5 days (e) and 10 days (f), the cubes have a size of 50 mm x 50 mm x 50 mm.

When no CO_2 was applied, almost the whole section of the sample turned red (Figure 5.7(a)), indicating a pH > 10. After carbonation at 75 °C for 1 day, Figure 5.7(b) displays that the cross-section remained red upon phenolphthalein spraying, however, there was no red color appearing on the surface of the cube when sprayed with phenolphthalein solution, which suggests the surface of the cube has been completely carbonated. Exposure to CO_2 for 1 more day reveals a fast

carbonation process, as the regions near the surface on the cut cross-section did not turn red corresponding to a carbonation product layer from surface nucleation and growth, as shown in Figure 5.7(c). However, further extension of CO_2 curing time did not show clear further decrease in the red-color region on the cross section, instead, the red color at the core area slowly faded away, as shown in Figure 5.7(d-e). These results qualitatively confirmed that formation of a carbonation product layer on the surface of the sample resisted the diffusion of CO_2, which slowed down the carbonation process at later ages.

The mechanism of such phenomenon has been previously attributed to: (i) the nucleation and growth of carbonate crystals which occurs at early reaction times, and whose rate of formation is a function of the surface area of the reactant [218], and, (ii) a diffusion- (transport-) limited process which requires CO_2 species to transport to microstructure hindered sites wherein carbonation occurs [29]. Such kinetics can be described by a generalized reaction-diffusion model as shown in Equation (5.9) [215]:

$$[1 - (1 - \alpha)^{\frac{1}{3}}]^n = kt \qquad \text{Eq. (5.9)}$$

where, α is the CO_2 uptake ratio (g of CO_2 uptake per g of reactant, i.e., fly ash), t is the time (days, d), k (d-1) is the apparent reaction rate constant, and n is an index related to the rate-determining step. For example, n = 1 represents the commonly used "contracting volume model" for rapid initial nucleation and growth of products from the reactants from an outer surface of a spherical shape [215]. When n = 2, Equation (5.9) reduces to Jander's model for diffusion-controlled reactions [215], wherein the reaction rate is determined by the transport of reactants through the product layer to the reaction interface. It should be noted that herein, the presence of liquid water serves to catalyze carbonation reactions, by offering a high pH medium that can host mobile CO_3^{2-}

ions.

Figure 5.8(a) shows fits of Equation (5.9) to the experimental carbonation data taken from Figure 5.6(a) for different carbonation temperatures. A clear change in slope is noted just prior to a reaction interval of 2 days. Across all temperatures, initially the slopes (m, unitless) of all the curves, wherein m = 1/n, are on the order of: m = 1 ± 0.2, while after 2 days, m = 0.5 ± 0.1. The slight deviation of the slopes from their ideal values (n = 1 and 2) is postulated to be on account of the wide-size distributions of the fly ash particles and the irregular coverage of particles offered by the carbonation products, e.g., as shown in Figure 5.5. And indeed, typical reaction models were developed assuming monodisperse, spherical reactant particles [213, 218]. The rate constants obtained from the fittings shown in Figure 5.8(a) were used to calculate the apparent activation energy of the two steps of carbonation reactions, i.e., a topochemical reaction step, followed by a diffusion-limited step as shown in Figure 5.8(b). This analysis reveals: (i) $E_{a,1}$ = 8.9 kJ/mole for surface nucleation reactions indicative of a small dependence of reaction rate on temperature, similar to that observed by Vance et al. for the carbonation of portlandite [5], and, (ii) $E_{a,2}$ = 24.1 kJ/mole for diffusion-controlled reaction; a value similar to that observed by Fernandez et al. [24], and Sun et al. [34] for the carbonation of MgO, and CaO respectively. The fact that the activation energy for surface nucleation reaction is much lower than that for diffusion-controlled reaction suggests that the carbonation reaction is dominated by nucleation and growth of carbonation products initially. However, as carbonation reaction progresses, the precipitation of carbonation products results in the formation of a barrier layer on the fly ash particles (see Figure 5.5) – that binds the particles together and simultaneously increases the resistance to the transport of CO_2 species to carbonation sites. As a result, the transport step assumes rate control in the later stages

of carbonation reactions.
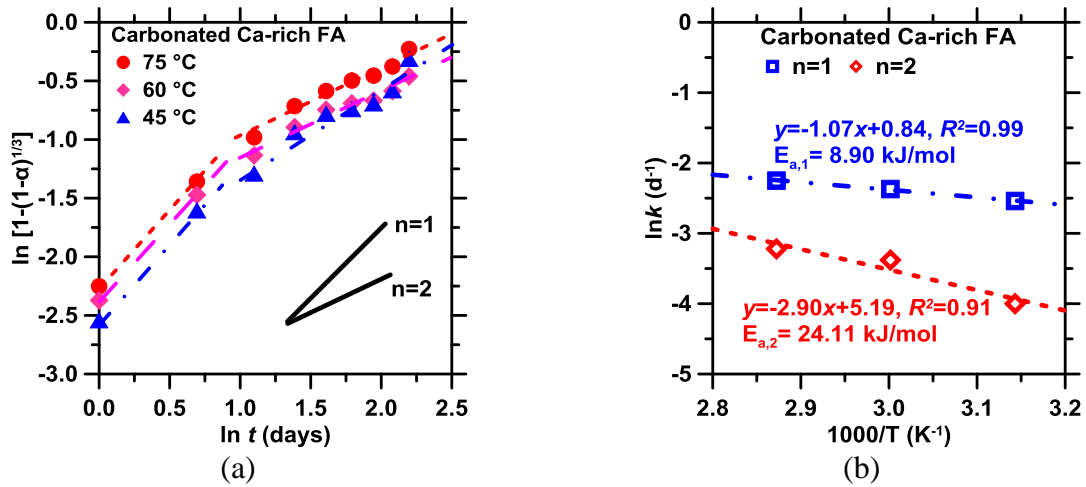
Figure 5.8: (a) Kinetic analysis of carbonation reactions occurring in Ca-rich fly ash formulations reacting at different temperatures in pure CO_2 over a period of 10 days. The data were fitted using the (surface) reaction-diffusion model shown in Equation (9), and, (b) An Arrhenius diagram for determining the apparent activation energies of: (i) surface nucleation and growth (n = 1), and, (ii) diffusion of reactant species through a surficial layer (n = 2).

5.4. Conclusion

This chapter has demonstrated an original means for clinkering free cementation by fly ash carbonation. Specifically, it is shown that Ca-rich fly ashes that host substantial quantities of Ca- (and Mg-) in the form of crystalline compounds, or in the glassy phases readily react with dilute concentrations of CO_2 in moist environments, at ambient pressure, and at sub-boiling temperatures to produce cemented solids whose properties are sufficient for use in structural construction. Indeed, Ca-rich fly ash solids, following CO_2 exposure achieve a strength of around 35 MPa after 7 days or so, and take-up 9% CO_2 by mass of reactants. Detailed results from thermodynamic

modeling, XRD analyses, and SEM observations suggest that fly ash carbonation results in the formation of a range of reaction products, namely calcite, hydrous silica, and potentially some C-S-H which collectively bond proximate particles into a cemented solid. Careful analysis of kinetic (rate) data using a reaction-diffusion model highlights two rate-controlling reaction steps: (a) where the surface area of the reactants, and the nucleation and growth of carbonate crystals there upon is dominant at early reaction times ($E_{a,1}$ = 8.9 kJ/mole), and, (b) a later-age process which involves the diffusion of CO_2 species through thickening surficial barriers to reactant sites ($E_{a,2}$ = 24.1 kJ/mole). It is noted that due to their reduced content of accessible [Ca, Mg] species, Ca-poor fly ashes feature limited potential vis-à-vis Ca-rich fly ashes for CO_2 uptake, and carbonation strengthening. Although the provision of extrinsic Ca sources to Ca-poor fly ashes can somewhat offset this lack, our observations suggest that the amount (mass abundance), reactivity, and spatial distribution of [Ca, Mg] are all important in determining a fly ash solid's suitability for CO_2 uptake and carbonation strengthening. Furthermore, it is noted that strength gain is linearly related to the extent of carbonation (CO_2 uptake). This suggests a straightforward means to estimate strength gain if the extent of carbonation may be known, or vice-versa. These observations are significant in that they demonstrate a new route for producing cemented solids by an innovative clinkering free, carbonation based pathway.

5.5. Implications on solid and flue gas CO_2 waste valorization in coal-fired power plants

Electricity generation from coal and natural gas combustion results in the production of substantial quantities of combustion residues and CO_2 emissions. For example, in the United States alone, coal combustion (for electricity production) resulted in the production of nearly 120 million tons of coal-combustion residuals (CCRs) [219, 220], and 1.2 billion tons of CO_2 emissions in 2016

[221]. While some CCRs find use in other industries (e.g., FGD gypsum, fly ash, etc.), the majority of CCRs continue to be land-filled. For example, in the U.S., only around 45-55 mass % of the annual production of fly ash is beneficially utilized – e.g., to replace cement in the binder fraction in traditional concrete – while the rest is disposed in landfills. Such underutilization stems from the presence of impurities in the fly ash including unburnt carbon and calcium sulfate that forms due to the sulfation of lime that is injected for air pollution control (APC) – which compromises the durability of traditional concrete. The materials examined herein, i.e., fly ashes that are cemented by carbonation, are not expected to be affected by the presence of such impurities – as a result, a wide range of Ca-rich fly ash sources – including those containing impurities, and mined from historical reservoirs (i.e., "ash ponds") are expected to be usable for carbonation-based fly ash cementation. When coupled with the fact that fly ash carbonation can be effected at sub-boiling temperatures, using dilute, untreated (flue-gas) CO_2 streams, the outcomes of this work create a pathway for the simultaneous utilization of both solid- and vapor-borne wastes created during coal combustion. Such routes for waste, and especially CO_2 valorization create value-addition pathways that can be achieved without a need for carbon capture (i.e., or more correctly CO_2 concentration enhancement), thereby offering a line-of-sight to economic viability in commercial markets [222] (N.B.: based on current best-available technologies (BATs) CO_2 capture using an amine stripper is expected to induce a financial burden of $ 60-to-90 per ton of CO_2 in addition to inducing parasitic energy losses for solvent regeneration [223, 224]). Importantly, the simplicity of this carbonation process ensures that it well-suited for co-location ("bolt-on, stack-tap" integration) at large point-source CO_2 emission sites including petrochemical facilities, coal/natural gas fired power plants, and cement plants. In each case, emitted flue gas can be used to provide both waste heat to hasten chemical reactions, and CO_2 to ensure mineralization without imposing any

additional needs for emissions control. The proposed approach is significant since – within a traditional lifecycle analysis (LCA) framework wherein there is no embodied CO_2 impact associated with reactants such as coal combustion wastes, or emitted CO_2, and wherein processing energy (heat) is secured from the flue gas stream – fly ash carbonation, by virtue of active CO_2 uptake, and CO_2 avoidance (i.e., by diminishing the production and use of OPC) has the potential to yield CO_2 negative pathways for cementation, and hence construction. New approaches of this nature are critical to create commercially viable routes for CO_2 utilization, and thereby accelerate the development and maturation of a viable carbon-to-value (CTV) economy [225].

Chapter 6 Summary, conclusions, and future work

6.1 Summary

This study was focused on (i) the evaluation of durability of cementitious composites containing microencapsulated PCMs, and (ii) the feasibility of developing cement-free sustainable building materials for building and infrastructure construction by synergizing the utilization of industrial wastes of fly ash and flue gas from coal-fired power plants. The following section provides a summary of this work.

Microencapsulated PCMs were subjected to simulated cementitious environments to study their survivability and phase change enthalpy stability in highly alkaline and caustic cement paste environments. It has been revealed that: (i) while PCMs remained unaffected in alkaline solutions, they experienced a significant enthalpy reduction, on the order of 25%, when exposed to sulfate-bearing environments. (ii) The mechanism of PCM enthalpy reduction in cementitious environments was hydrolysis of the melamine-formaldehyde shell of the PCM microcapsule, followed by shell rupture and paraffinic PCM core in contact with sulfate ions.

Water absorption and drying shrinkage measurements were performed on cementitious composite specimens containing various volume fractions of microencapsulated PCMs. It has been revealed that: (i) PCMs served as a non-sorptive inclusion similar to graded quartz sand in the composites, therefore, increasing the volume fraction of either inclusion reduced the volume of water sorbed, and the rate of water sorption. (ii) The water absorption behavior of cementitious composites containing PCMs can be described by a sorption-diffusion model to predict time-dependent

moisture ingress. (iii) The extent of terminal water sorption of cementitious composites containing non-sorptive inclusions, can be estimated using Powers' model. (iv) The drying shrinkage of cementitious composites was essentially unaltered by the presence of PCMs, as such, compliant inclusions were unable to offer any resistance to the cement paste's shrinkage. (v) The model of Hobbs is able to properly capture the effects of both inclusion stiffness and volume fraction, providing a means to estimate the shrinkage of cementitious composites containing such inclusions.

Measurements of tensile strength, restrained shrinkage, free shrinkage, and elastic modulus were performed on cementitious composites containing various volume fractions of microencapsulated PCMs to examine the influences of soft PCM inclusions on the cracking resistance of cementitious composites. It has been shown that: (i) in spite of inducing substantial reductions in the compressive strength of cementitious composite, PCM addition (up to 20% volume fraction) did not change the tensile strength of the composite. (ii) Cementitious composites containing microencapsulated PCMs showed substantial delay in their time to cracking when subjected to restrained shrinkage conditions, which was attributed to the effects of crack blunting and deflection resultant from PCM inclusions and enhanced stress relaxation.

Thermal deformation coefficient measurements were performed on prismatic cementitious composites containing various volume fractions of microencapsulated PCM inclusions in order to use experimental data to retrieve deformation properties of microencapsulated PCMs in cementitious composites. It has been found that: (i) Predictions from the effective medium approximation developed by Schapery [176] was found to be capable of retrieving the thermal

deformation coefficient of PCM microcapsules and of quartz sand grains. (ii) The thermal deformation coefficient of the PCM microcapsules was found to be near that of the shell material, due to the fact that the capsules might not be completely filled with PCM, thus leaving space inside for the PCM core to expand. (iii) Schapery's model was shown to predict accurately the effective thermal deformation coefficient of cementitious composite samples with a mixture of microencapsulated PCM and quartz sand inclusions based on the previously retrieved properties. (iv) A design rule can be used to determine the amount of quartz sand required to offset the effect of the PCM microcapsules in increasing the thermal deformation coefficient of PCM-mortar composites.

Carbonation of fly ash paste was performed to explore clinkering free cementation for sustainable building and infrastructure construction. It has been shown that: (i) Ca-rich fly ash can readily react with dilute concentrations of CO_2 in moist environments to produce cemented solids with compressive strength as high as 35 MPa and CO_2 uptake of 9% at 75 °C. (ii) The strength gain is linearly related to the extent of CO_2 uptake, due to the formation of a range of reaction products (e.g., calcite, hydrous silica, and C-S-H) during fly ash carbonation, which collectively bond proximate particles into a cemented solid.

6.2 Conclusions

This study systematically investigated the influences of adding microencapsulated PCMs in cementitious composite on the stability of PCMs and the durability of the composite, it also established a viable means to develop sustainable carbon-negative building materials by fly ash carbonation. The aforementioned summary reveals that while PCMs may themselves be

106

detrimentally impacted in sulfate-containing cementitious environments, they do not detrimentally impact the durability of cementitious composites in which they are embedded. In fact, the addition of soft PCM inclusions in cementitious composites can extend the time to cracking when the specimens are subjected to restrained shrinking condition. In other words, PCM microcapsules embedded in cementitious composites are not only capable of regulating temperature of construction components by their ability to store and release heat in response to environmental temperature changes by undergoing reversible phase transitions, they also have the ability to reduce cracking risk by extending the time to cracking in cementitious composites. To counteract the phase change enthalpy loss due to gradual breakdown of the encapsulation shell in cementitious environments in Chapter 2, new shell materials and technologies are needed for better encapsulation and protection of the paraffinic core. Chapter 3 suggested that addition of soft (compliant) inclusions can enhance the cracking resistance of cementitious composites. This observations, and the presented data (i.e., restrained volume change, composite stiffness, tensile strength) provide foundational inputs to guide modelling efforts that seek to assess and quantify cracking risks of cementitious composites containing soft inclusions. Similarly, the results of thermal deformation properties of microencapsulated PCMs presented in Chapter 4 could be useful in modeling the thermal deformation behavior of pavement sections featuring microencapsulated PCMs for thermally induced crack resistance. Chapter 5 demonstrated the feasibility of using carbonation process to produce prefabricated sections for sustainable construction, which is well suited for efficient integration of manufacturing of upcycled concrete product into large point-source CO_2 emission sites including coal/natural gas fired power plants and cement plants.

6.3 Future work

The following sections present recommendations for future efforts to (i) further investigate and improve the stability and durability of cementitious composites containing microencapsulated PCM inclusions in concrete elements as energy efficient building envelops and crack-resistant pavement sections, and (ii) develop sustainable cementation solutions through mineral carbonation of industrial wastes.

6.3.1 Microencapsulation of PCMs with new shell materials for enhanced stability and durability in cementitious composites

The embedment of PCMs has been demonstrated as a means to improve thermal performance of building envelops and to mitigate thermal cracking in restrained concrete elements such as pavement and bridge decks. However, Chapter 2 revealed that PCMs experienced approximately 25% enthalpy reduction when incorporated in cementitious environments due to gradual hydrolysis of the melamine-formaldehyde (MF) shell of the PCM microcapsule, followed by shell rupture and paraffinic PCM core in contact with sulfate ions. For PCMs encapsulated with other polymeric (e.g., acrylic) shell than MF, a similar reduction in phase change enthalpy was also observed previously when they are embedded in cement paste [51]. However, when PCM microcapsules with both MF and acrylic shells were immersed in sulfate solutions, only those with MF shells showed enthalpy reduction [186]. The reason why PCM capsules with more stable (acrylic) shells would also experience enthalpy reduction in cementitious environments remain unclear and should be interesting to look into. The loss of thermal energy storage capacity of microencapsulated PCMs also suggests a significant disadvantage of current encapsulation material and technology as it makes the thermal benefits of PCMs less effective. Furthermore, the

gradual release of formaldehyde during breakdown of the melamine-formaldehyde shell poses a serious environmental and health problem for PCM-embedded buildings and infrastructure [226]. In addition, there are still other disadvantages associated with polymer-encapsulated PCMs such as flammability and low thermal conductivity, the latter often results in slow heat transfer rate when PCMs are expected to give prompt responses during thermal storage and regulation processes [227]. It is well known that inorganic materials usually have great thermal and chemical stability, and good flame retardant property. Therefore, some of the most interesting directions for further research around this area are (i) the chemical reactions and mechanism of enthalpy reduction associated with PCM encapsulated with polymers other than MF when they are incorporated in cementitious composites, (ii) the kinetics and of formaldehyde release during MF breakdown in cementitious composites and the diffusion behavior of formaldehyde from the composite material to indoor air, (iii) the identification and feasibility of stable inorganic materials for encapsulation of paraffin-based PCMs, and (iv) the thermo-mechanical properties and stability of PCMs capsulated by inorganic materials and their influences on the durability of the cementitious composites in which they are embedded, just to mention a few.

6.3.2 Sustainable cementation by carbonation of industrial wastes

Chapter 5 investigated the feasibility of clinkering free cementation via carbonation of fly ash, which is an abundant by-product from coal combustion in coal-fired power plants. It should be noted that other abundantly available alkaline waste minerals such as residues from municipal waste combustion [34], and steel production (slags) [30, 35] are also good candidates for carbonation to provide sustainable cementation while sequestering CO_2 from flue gas. It was found in Chapter 5 that fly ash paste could achieve a strength as high as 35 MPa. The fly ash used

in the study was a Ca-rich Class C fly ash (with CaO simple oxide content of 26.5%), and the carbonation process was as long as 7 days. Ca-poor fly ash, however, exhibited very limited strength gain upon carbonation, even when Ca-sources were added in to produce Ca contents equivalent to the Ca-rich fly ash. To more efficiently expedite the carbonation process for enhanced strength gain and better take advantage of alkaline industrial solid wastes with lower Ca content for cementation purpose, further research attention should be placed in the following aspects.

It was postulated in the current study that reactive crystalline compounds (e.g., CaO, $Ca_3Al_2O_6$, etc.) present in a Ca-rich fly ash are expected to rapidly dissolve upon contact with water. As the pH systematically increases, with continuing dissolution, alkaline species including Na, K, Ca are expected to be released progressively from the glassy compounds for CO_2 mineralization. However, for other industrial wastes such as crystallized iron slags, Ca and Mg species are expected to dissolve and release very slowly from the crystals under natural conditions [228]. In this case scenario, the crystalized slags can be grounded into fine granules to obtain high surface areas and associated interface effects, and a leaching process can be followed to extract metal ions from the granulated slags to facilitate release of Ca and Mg species. These ions can be further concentrated through capacitive concentrator linked to leaching solutions to further precipitate portlandite [229-231]. The resultant portlandite slurry and leached slag granules can be then mixed together for carbonation strengthening and cementation. Alternatively, Ca and Ma species in slags can be released by an electrolytic process [27], in which acidity generated by electrolysis of wastewater could directly dissolve industrial waste particles in the anode and liberate metal ions, which balance the hydroxide ions produced at the cathode to form metal hydroxide.

References

[1]   Mineral   Comodity   Summaries   2017,   U.S.   Geological   Survey.
https://minerals.usgs.gov/minerals/pubs/mcs/2017/mcs2017.pdf, (accessed June 1 2017).

[2] M. Schneider, M. Romer, M. Tschudin, H. Bolio, Sustainable cement production—present and future, Cement and Concrete Research, 41 (2011) 642-650.

[3] C. Shi, A.F. Jiménez, A. Palomo, New cements for the 21st century: The pursuit of an alternative to Portland cement, Cement and Concrete Research, 41 (2011) 750-763.

[4] J.J. Biernacki, J.W. Bullard, G. Sant, K. Brown, F.P. Glasser, S. Jones, T. Ley, R. Livingston, L. Nicoleau, J. Olek, F. Sanchez, R. Shahsavari, P.E. Stutzman, K. Sobolev, T. Prater, Cements in the 21st century: Challenges, perspectives, and opportunities, Journal of the American Ceramic Society, 100 (2017) 2746-2773.

[5] K. Vance, G. Falzone, I. Pignatelli, M. Bauchy, M. Balonis, G. Sant, Direct carbonation of $Ca(OH)_2$ using liquid and supercritical CO_2: Implications for carbon-neutral cementation, Industrial & Engineering Chemistry Research, 54 (2015) 8908-8918.

[6] G.C. Bye, Portland Cement: Composition, Production and Properties, Thomas Telford, second edition, 1999

[7] P.K. Mehta, P.J.M. Monteiro, Concrete: Microstructure, Properties, and Materials, McGraw-Hill, fourth edition, 2014.

[8] S. Mindess, J.F. Young, D. Darwin, Concrete, Prentice Hall, second edition, 2003.

[9] T. Hemalatha, A. Ramaswamy, A review on fly ash characteristics – Towards promoting high volume utilization in developing sustainable concrete, Journal of Cleaner Production, 147 (2017) 546-559.

[10] G. Montes-Hernandez, R. Perez-Lopez, F. Renard, J.M. Nieto, L. Charlet, Mineral sequestration of CO_2 by aqueous carbonation of coal combustion fly-ash, Journal of hazardous materials, 161 (2009) 1347-1354.

[11] J. Vargas, A. Halog, Effective carbon emission reductions from using upgraded fly ash in the cement industry, Journal of Cleaner Production, 103 (2015) 948-959.

[12] ASTM International, ASTM Standard C618: Standard specification for coal fly ash and raw or calcined natural pozzolan for use in concrete, West Conshohocken, PA, 2015.

[13] Coal combustion residual beneficial use evaluation: fly ash concrete and FGD gypsum

wallboard, U.S. Environmental Protection Agency, February 2014. https://www.epa.gov/sites/production/files/2014-12/documents/ccr_bu_app.pdf (accessed June 1, 2017).

[14] M. Ahmaruzzaman, A review on the utilization of fly ash, Progress in Energy and Combustion Science, 36 (2010) 327-363.

[15] M. Thomas, Optimizing the use of fly ash in concrete, IS548, Portland Cement Association, Skokie, IL, 2007.

[16] S. Kumar, R. Kumar, A. Bandopadhyay, Innovative methodologies for the utilisation of wastes from metallurgical and allied industries, Resources, Conservation and Recycling, 48 (2006) 301-314.

[17] A. Sanna, M. Uibu, G. Caramanna, R. Kuusik, M.M. Maroto-Valer, A review of mineral carbonation technologies to sequester CO_2, Chemical Society Reviews, 43 (2014) 8049-8080.

[18] J. Jaschik, M. Jaschik, K. Warmuziński, The utilisation of fly ash in CO_2 mineral carbonation, Chemical and Process Engineering, 37 (2016) 29-39.

[19] V. Romanov, Y. Soong, C. Carney, G.E. Rush, B. Nielsen, W. O'Connor, Mineralization of carbon dioxide: A literature review, ChemBioEng Reviews, 2 (2015) 231-256.

[20] W. Ashraf, Carbonation of cement-based materials: Challenges and opportunities, Construction and Building Materials, 120 (2016) 558-570.

[21] M. Bauer, N. Gassen, H. Stanjek, S. Peiffer, Carbonation of lignite fly ash at ambient T and P in a semi-dry reaction system for CO_2 sequestration, Applied Geochemistry, 26 (2011) 1502-1512.

[22] D. Daval, I. Martinez, J. Corvisier, N. Findling, B. Goffe, F. Guyot, Combining experimental studies and kinetic modelling to investigate the carbonation of Ca-bearing silicates, Geochimica et Cosmochimica Acta, Goldschmidt Conference Abstract, 72 (2008) A200.

[23] D. Daval, I. Martinez, J. Corvisier, N. Findling, B. Goffe, F. Guyot, Carbonation of Ca-bearing silicates, the case of wollastonite: Experimental investigations and kinetic modeling, Chem Geol, 265 (2009) 63-78.

[24] A.I. Fernandez, J.M. Chimenos, M. Segarra, M.A. Fernandez, F. Espiell, Kinetic study of carbonation of MgO slurries, Hydrometallurdy, 53 (1999) 155-167.

[25] L. He, D. Yu, W. Lv, J. Wu, M. Xu, A Novel Method for CO_2 Sequestration via indirect carbonation of coal fly ash, Industrial & Engineering Chemistry Research, 52 (2013) 15138-15145.

112

[26] W.J.J. Huijgen, G.J. Witkamp, R.N.J. Comans, Mechanisms of aqueous wollastonite carbonation as a possible CO_2 sequestration process, Chemical Engineering Science, 61 (2006) 4242-4251.

[27] L. Lu, Y. Fang, Z. Huang, Y. Huang, Z.J. Ren, Self-sustaining carbon capture and mineralization via electrolytic carbonation of coal fly ash, Chemical Engineering Journal, 306 (2016) 330-335.

[28] M.G. Nyambura, G.W. Mugera, P.L. Felicia, N.P. Gathura, Carbonation of brine impacted fractionated coal fly ash: implications for CO_2 sequestration, Journal of environmental management, 92 (2011) 655-664.

[29] S.Y. Pan, E.E. Chang, P.C. Chiang, CO_2 capture by accelerated carbonation of alkaline wastes: a review on its principles and applications, Aerosol and Air Quality Research, 12 (2012) 770-291.

[30] S. Tian, J. Jiang, K. Li, F. Yan, X. Chen, Performance of steel slag in carbonation–calcination looping for CO_2 capture from industrial flue gas, RSC Advances, 4 (2014) 6858-6862.

[31] N.L. Ukwattage, P.G. Ranjith, M. Yellishetty, H.H. Bui, T. Xu, A laboratory-scale study of the aqueous mineral carbonation of coal fly ash for CO_2 sequestration, Journal of Cleaner Production, 103 (2015) 665-674.

[32] L. Mo, F. Zhang, D.K. Panesar, M. Deng, Development of low-carbon cementitious materials via carbonating Portland cement–fly ash–magnesia blends under various curing scenarios: a comparative study, Journal of Cleaner Production, 163 (2017) 252-261.

[33] D. Zhang, X.H. Cai, Y.X. Shao, Carbonation curing of precast fly ash concrete, Journal of Materials in Civil Engineering, 28 (2016) 04016127.

[34] J. Sun, M.F. Bertos, S.J.R. Simons, Kinetic study of accelerated carbonation of municipal solid waste incinerator air pollution control residues for sequestration of flue gas CO_2, Energy & Environmental Science, 1 (2008) 370-377.

[35] S. Tian, J. Jiang, X. Chen, F. Yan, K. Li, Direct gas-solid carbonation kinetics of steel slag and the contribution to in situ sequestration of flue gas CO2 in steel-making plants, ChemSusChem, 6 (2013) 2348-2355.

[36] M. Mahoutian, Y. Shao, Production of cement-free construction blocks from industry wastes, Journal of Cleaner Production, 137 (2016) 1339-1346.

[37] A.M. Thiele, Z.H. Wei, G. Falzone, B.A. Young, N. Neithalath, G. Sant, L. Pilon, Figure of

merit for the thermal performance of cementitious composites containing phase change materials, Cement and Concrete Composites, 65 (2016) 214-226.

[38] D.W. Hawes, D. Banu, D. Feldman, LATENT-HEAT STORAGE IN CONCRETE, Solar Energy Materials, 19 (1989) 335-348.

[39] M. Pomianowski, P. Heiselberg, R.L. Jensen, Dynamic heat storage and cooling capacity of a concrete deck with PCM and thermally activated building system, Energy and Buildings, 53 (2012) 96-107.

[40] T. Lee, D.W. Hawes, D. Banu, D. Feldman, Control aspects of latent heat storage and recovery in concrete, Solar Energy Materials and Solar Cells, 62 (2000) 217-237.

[41] H.J. Alqallaf, E.M. Alawadhi, Concrete roof with cylindrical holes containing PCM to reduce the heat gain, Energy and Buildings, 61 (2013) 73-80.

[42] Z.H. Wei, G. Falzone, B. Wang, A. Thiele, G. Puerta-Falla, L. Piton, N. Neithalath, G. Sant, The durability of cementitious composites containing microencapsulated phase change materials, Cement and Concrete Composites, 81 (2017) 66-76.

[43] BritishPetroleum, Statistical Review of World Energy, 2010.

[44] L. Perez-Lombard, J. Ortiz, C. Pout, A review on buildings energy consumption information, Energy and Buildings, 40 (2008) 394-398.

[45] D.A. Neeper, Thermal dynamics of wallboard with latent heat storage, Solar Energy, 68 (2000) 393-403.

[46] N. Soares, J.J. Costa, A.R. Gaspar, P. Santos, Review of passive PCM latent heat thermal energy storage systems towards buildings' energy efficiency, Energy and Buildings, 59 (2013) 82-103.

[47] F. Agyenim, N. Hewitt, P. Eames, M. Smyth, A review of materials, heat transfer and phase change problem formulation for latent heat thermal energy storage systems (LHTESS), Renewable and Sustainable Energy Review, 14 (2010) 615-628.

[48] S. Jegadheeswaran, S.D. Pohekar, Performance enhancement in latent heat thermal storage system: A review, Renewable and Sustainable Energy Review, 13 (2009) 2225-2244.

[49] Y. Zhang, G. Zhou, K. Lin, Q. Zhang, H. Di, Application of latent heat thermal energy storage in buildings: State-of-the-art and outlook, Building and Environment, 42 (2007) 2197-2209.

[50] S.D. Sharma, D. Buddhi, R.L. Sawhney, Accelerated thermal cycle test of latent heat-storage materials, Solar Energy, 66 (1999) 483-490.

[51] F. Fernandes, S. Manari, M. Aguayo, K. Santos, T. Oey, Z.H. Wei, G. Falzone, N. Neithalath, G. Sant, On the feasibility of using phase change materials (PCMs) to mitigate thermal cracking in cementitious materials, Cement and Concrete Composites, 51 (2014) 14-26.

[52] Thermal Energy Storage for Sustainable Energy Consumption: Fundamentals, Case Studies and Design, Thermal Energy Storage for Sustainable Energy Consumption: Fundamentals, Case Studies and Design, 234 (2007) 1-447.

[53] A. Oliver, Thermal characterization of gypsum boards with PCM included: Thermal energy storage in buildings through latent heat, Energy and Buildings, 48 (2012) 1-7.

[54] B. Zalba, J.M. Marin, L.F. Cabeza, H. Mehling, Review on thermal energy storage with phase change: materials, heat transfer analysis and applications, Applied Thermal Engineering, 23 (2003) 251-283.

[55] A. Sharma, V.V. Tyagi, C.R. Chen, D. Buddhi, Review on thermal energy storage with phase change materials and applications, Renewable and Sustainable Energy Review, 13 (2009) 318-345.

[56] D. Zhou, C.Y. Zhao, Y. Tian, Review on thermal energy storage with phase change materials (PCMs) in building applications, Applied Energy, 92 (2012) 593-605.

[57] E. Oro, A. de Gracia, A. Castell, M.M. Farid, L.F. Cabeza, Review on phase change materials (PCMs) for cold thermal energy storage applications, Applied Energy, 99 (2012) 513-533.

[58] F. Kuznik, D. David, K. Johannes, J.J. Roux, A review on phase change materials integrated in building walls, Renewable and Sustainable Energy Review, 15 (2011) 379-391.

[59] F. Kuznik, D. David, K. Johannes, J.-J. Roux, A review on phase change materials integrated in building walls, Renewable and Sustainable Energy Review, 15 (2011) 379-391.

[60] V.A.A. Raj, R. Velraj, Review on free cooling of buildings using phase change materials, Renewable and Sustainable Energy Review, 14 (2010) 2819-2829.

[61] A.M. Khudhair, M.M. Farid, A review on energy conservation in building applications with thermal storage by latent heat using phase change materials, Energy Conversion and Management, 45 (2004) 263-275.

[62] D.P. Bentz, R. Turpin, Potential applications of phase change materials in concrete technology, Cement and Concrete Composites, 29 (2007) 527-532.

[63] R. Baetens, B.P. Jelle, A. Gustavsen, Phase change materials for building applications: A state-of-the-art review, Energy and Buildings, 42 (2010) 1361-1368.

[64] A.R. Sakulich, D.P. Bentz, Incorporation of phase change materials in cementitious systems via fine lightweight aggregate, Construction and Building Materials, 35 (2012) 483-490.

[65] C.Y. Zhao, W. Lu, Y. Tian, Heat transfer enhancement for thermal energy storage using metal foams embedded within phase change materials (PCMs), Solar Energy, 84 (2010) 1402-1412.

[66] A.G. Entrop, H.J.H. Brouwers, A.H.M.E. Reinders, Experimental research on the use of micro-encapsulated Phase Change Materials to store solar energy in concrete floors and to save energy in Dutch houses, Solar Energy, 85 (2011) 1007-1020.

[67] D. Zhou, C.Y. Zhao, Experimental investigations on heat transfer in phase change materials (PCMs) embedded in porous materials, Applied Thermal Engineering, 31 (2011) 970-977.

[68] Y. Farnam, M. Krafcik, L. Liston, L. Washington, K. Erk, B. Tao, J. Weiss, Evaluating the use of phase change materials in concrete pavement to melt ice and snow, Journal of Materials in Civil Engineering, 2015 (2015) 1943-5533.

[69] M.N.A. Hawlader, M.S. Uddin, H.J. Zhu, Encapsulated phase change materials for thermal energy storage: Experiments and simulation, International Journal of Energy Research, 26 (2002) 159-171.

[70] N. Zhu, Z. Ma, S. Wang, Dynamic characteristics and energy performance of buildings using phase change materials: A review, Energy Conversion and Management, 50 (2009) 3169-3181.

[71] V.V. Tyagi, S.C. Kaushik, S.K. Tyagi, T. Akiyama, Development of phase change materials based microencapsulated technology for buildings: A review, Renewale and Sustainable Energy Review, 15 (2011) 1373-1391.

[72] M. Kenisarin, K. Mahkamov, Solar energy storage using phase change materials, Renewale and Sustainable Energy Review, 11 (2007) 1913-1965.

[73] H. Bo, E.M. Gustafsson, F. Setterwall, Tetradecane and hexadecane binary mixtures as phase change materials (PCMs) for cool storage in district cooling systems, Energy, 24 (1999) 1015-1028.

[74] A. Sari, A. Karaipekli, Fatty acid esters-based composite phase change materials for thermal energy storage in buildings, Applied Thermal Engineering, 37 (2012) 208-216.

[75] M. Li, H. Kao, Z. Wu, J. Tan, Study on preparation and thermal property of binary fatty acid and the binary fatty acids/diatomite composite phase change materials, Applied Energy, 88 (2011) 1606-1612.

[76] M. Hunger, A.G. Entrop, I. Mandilaras, H.J.H. Brouwers, M. Founti, The behavior of self-

compacting concrete containing micro-encapsulated Phase Change Materials, Cement and Concrete Composites, 31 (2009) 731-743.

[77] Z. Wei, F. Galzone, B. Wang, A. Thiele, G. Puerta-Falla, L. Pilon, N. Neithalath, G. Sant, The durability of cementitious composites containing microencapsulated phase change materials, Cement and Concrete Composites, 86 (2017) 66-76.

[78] P. Meshgin, Y. Xi, Y. Li, Utilization of phase change materials and rubber particles to improve thermal and mechanical properties of mortar, Construction and Building Materials, 28 (2012) 713-721.

[79] B. Savija, E. Schlangen, Use of phase change materials (PCMs) to mitigate early age thermal cracking in concrete: Theoretical considerations, Construction and Building Materials, 126 (2016) 332-344.

[80] J. Skalny, I. Jawed, H.F.W. Taylor, Studies on hydration of cement - recent developments, World Cement Technology, 9 (1978) 183-188.

[81] D.E. Macphee, E.E. Lachowski, A.H. Taylor, T.J. Brown, Microstructural development in pore reduced cement (PRC), Materials Research Society Symposium Proceedings, 245 (1992) 303-308.

[82] D.W. Zhang, H. Furuuchi, A. Hori, T. Ueda, Fatigue degradation properties of PCM-concrete interface, Journal of Advanced Concrete Technology, 7 (2009) 425-438.

[83] A. Sharma, S.D. Sharma, D. Buddhi, Accelerated thermal cycle test of acetamide, stearic acid and paraffin wax for solar thermal latent heat storage applications, Energy Conversion and Management, 43 (2002) 1923-1930.

[84] V.V. Tyagi, D. Buddhi, Thermal cycle testing of calcium chloride hexahydrate as a possible PCM for latent heat storage, Solar Energy Materials and Solar Cells, 92 (2008) 891-899.

[85] J.F. Su, X.Y. Wang, H. Dong, Micromechanical properties of melamine-formaldehyde microcapsules by nanoindentation: Effect of size and shell thickness, Materials Letters, 89 (2012) 1-4.

[86] S. Das, A. Maroli, N. Neithalath, Finite element-based micromechanical modeling of the influence of phase properties on the elastic response of cementitious mortars, Construction and Building Materials, 127 (2016) 153-166.

[87] M. Aguayo, S. Das, A. Maroli, N. Kabay, J.C.E. Mertens, S.D. Rajan, G. Sant, N. Chawla, N. Neithalath, The influence of microencapsulated phase change material (PCM) characteristics on

the microstructure and strength of cementitious composites: Experiments and finite element simulations, Cement and Concrete Composites, 73 (2016) 29-41.

[88] K.C. Ting, P.N. Giannakakos, S.G. Gilbert, Durability of latent-heat storage tube-sheets, Solar Energy, 39 (1987) 79-85.

[89] H. Chao-Lung, B.L. Anh-Tuan, C. Chun-Tsun, Effect of rice husk ash on the strength and durability characteristics of concrete, Construction and Building Materials, 25 (2011) 3768-3772.

[90] D.F. Aponte, M. Barra, E. Vazquez, Durability and cementing efficiency of fly ash in concretes, Construction and Building Materials, 30 (2012) 537-546.

[91] K. Peippo, P. Kauranen, P.D. Lund, A multicomponent PCM wall optimized for passive solar heating, Energy and Buildings, 17 (1991) 259-270.

[92] K. Lin, Y. Zhang, X. Xu, H. Di, R. Qin, R. Yang, Experimental study of under-floor electric heating system with shape-stabilized PCM plates, Proceedings of the 4th International Symposium on Heating, Ventilating and Air Conditioning, Vols 1 and 2, (2003) 646-652.

[93] K.P. Lin, Y.P. Zhang, Modeling and simulation of thermal performance of under-floor electric heating system with shape-stabilized PCM thermal energy storage plate, Energy and Environment, Vols 1 and 2, (2003) 1069-1074.

[94] K.P. Lin, Y.P. Zhang, X. Xu, H.D. Di, R. Yang, P.H. Qin, Modeling and simulation of under-floor electric heating system with shape-stabilized PCM plates, Building and Environment, 39 (2004) 1427-1434.

[95] K.P. Lin, Y.P. Zhang, X. Xu, H.F. Di, R. Yang, P.H. Qin, Experimental study of under-floor electric heating system with shape-stabilized PCM plates, Energy and Buildings, 37 (2005) 215-220.

[96] W. Saman, F. Bruno, E. Halawa, Thermal performance of PCM thermal storage unit for a roof integrated solar heating system, Solar Energy, 78 (2005) 341-349.

[97] K. Lin, Y. Zhang, H. Di, R. Yang, Study of an electrical heating system with ductless air supply and shape-stabilized PCM for thermal storage, Energy Conversion and Management, 48 (2007) 2016-2024.

[98] K.P. Lin, Y.P. Zhang, H.F. Di, R. Yang, Study of an electrical heating system with ductless air supply and shape-stabilized PCM for thermal storage, Energy Conversion and Management, 48 (2007) 2016-2024.

[99] G.B. Zhou, Y.P. Zhang, X. Wang, K.P. Lin, W. Xiao, An assessment of mixed type PCM-

gypsum and shape-stabilized PCM plates in a building for passive solar heating, Solar Energy, 81 (2007) 1351-1360.

[100] M. Isaac, D.P. van Vuuren, Modeling global residential sector energy demand for heating and air conditioning in the context of climate change, Energy Policy, 37 (2009) 507-521.

[101] Y. Hong, X.S. Ge, Preparation of polyethylene-paraffin compound as a form-stable solid-liquid phase change material, Solar Energy Materials and Solar Cells, 64 (2000) 37-44.

[102] A. Sari, Form-stable paraffin/high density polyethylene composites as solid-liquid phase change material for thermal energy storage: preparation and thermal properties, Energy Conversion and Management, 45 (2004) 2033-2042.

[103] S. Karaman, A. Karaipekli, A. Sari, A. Bicer, Polyethylene glycol (PEG)/diatomite composite as a novel form-stable phase change material for thermal energy storage, Solar Energy Materials and Solar Cells, 95 (2011) 1647-1653.

[104] Z. Chen, F. Shan, L. Cao, G. Fang, Preparation and thermal properties of n-octadecane/molecular sieve composites as form-stable thermal energy storage materials for buildings, Energy and Buildings, 49 (2012) 423-428.

[105] C.H. Shen, Z.H. Shui, Unsaturated water transport of cement-based materials, Journal of Wuhan University of Technology, 22 (2007) 770-773.

[106] D.R.M. Brew, F.C. de Beer, M.J. Radebe, R. Nshimirimana, P.J. McGlinn, L.P. Aldridge, T.E. Payne, Water transport through cement-based barriers-A preliminary study using neutron radiography and tomography, Nuclear Instruments and Methods in Physics Research Section A, 605 (2009) 163-166.

[107] C. Hazaree, K.J. Wang, H. Ceylan, K. Gopalakrishnan, Capillary transport in RCC: Water-to-cement ratio, strength, and freeze-thaw resistance, Journal of Materials in Civil Engineering, 23 (2011) 1181-1191.

[108] A.M. Olaru, B. Blumich, A. Adams, Water transport in cement-in-polymer dispersions at variable temperature studied by magnetic resonance imaging, Cement and Concrete Research, 44 (2013) 55-68.

[109] P.K. Hou, X. Cheng, J.S. Qian, R. Zhang, W. Cao, S.P. Shah, Characteristics of surface-treatment of nano-SiO2 on the transport properties of hardened cement pastes with different water-to-cement ratios, Cement and Concrete Composites, 55 (2015) 26-33.

[110] R. Henkensiefken, J. Castro, D. Bentz, T. Nantung, J. Weiss, Water absorption in internally

cured mortar made with water-filled lightweight aggregate, Cement and Concrete Research, 39 (2009) 883-892.

[111] J. Castro, D. Bentz, J. Weiss, Effect of sample conditioning on the water absorption of concrete, Cement and Concrete Composites, 33 (2011) 805-813.

[112] T. Tracz, J. Sliwinski, Effect of cement paste content and w/c ratio on concrete water absorption, Cem Wapno Beton, 17 (2012) 131-137.

[113] ASTM International, ASTM Standard C1585: Standard test method for measurement of rate of absorption of water by hydraulic-cement concretes, , West Conshohocken, PA, 2012.

[114] T.C. Powers, Absorption of water by Portland cement paste during the hardening process, Industry & Engineering Chemistry, 27 (1935) 790-794.

[115] S.D. Abyaneh, H.S. Wong, N.R. Buenfeld, Computational investigation of capillary absorption in concrete using a three-dimensional mesoscale approach, Computational Materials Science, 87 (2014) 54-64.

[116] G. Egan, A. Kumar, N. Neithalath, G. Sant, Re-examining the influence of the inclusion characteristics on the drying shrinkage of cementitious composites, Construction and Building Materials, (Under Review).

[117] K.J. Shin, B. Bucher, J. Weiss, Role of lightweight synthetic particles on the restrained shrinkage cracking behavior of mortar, Journal of Materials in Civil Engineering, 23 (2011) 597-605.

[118] P. Lura, O.M. Jensen, J. Weiss, Cracking in cement paste induced by autogenous shrinkage, Materials and Structures, 42 (2009) 1089-1099.

[119] J. Weiss, P. Lura, F. Rajabipour, G. Sant, Performance of shrinkage-reducing admixtures at different humidities and at early ages, ACI Materials Journal, 105 (2008) 478-486.

[120] C. Hall, W.D. Hoff, M.A. Wilson, Effect of nonsorptive inclusions on capillary absorption by a porous material, Journal of Physics D: Applied Physics, 26 (1993) 31-34.

[121] A.L. Stockett, Schneide.Am, Mardulie.Fj, An Analysis of Drying Shrinkage Data for Portland Cement Mortar and Concrete, Journal of Materials, 2 (1967) 829-835.

[122] B.H. Christian, B.J.F. Patten, Multiphase aspects of concrete drying shrinkage, Civil Engineering Transactions, Institute of Engineerings, Australia, 2 (1968) 229-236.

[123] G. Falzone, G. Puerta, Z. Wei, M. Zhao, A. Kumar, M. Bauchy, N. Neithalath, L. Pilon, G. Sant, The influences of soft and stiff inclusions on the mechanical properties of cementitious

composites, Cement and Concrete Composites, 71 (2016) 153-165.

[124] A.R. Sakulich, D.P. Bentz, Increasing the service life of bridge decks by incorporating phase-change materials to reduce freeze-thaw cycles, Journal of Materials in Civil Engineering, 24 (2012) 1034-1042.

[125] ASTM International, ASTM Standard C150/C150M: Standard specification of portland cement, West Conshohocken, PA, 2012.

[126] ASTM International, ASTM Standard C192/C192M: Standard practice for making and curing concrete test specimens in the laboratory, West Conshohocken, PA, 2012.

[127] ASTM International, ASTM Standard C778: Standard specification for standard sand, West Conshohocken, PA, 2013.

[128] C.F. Ferraris, V.A. Hackley, A.I. Avilés, Measurement of particle size distribution in portland cement powder: Analysis of ASTM round robin studies, Cement Concrete Aggregate, 26 (2004) 1-11.

[129] G. Gao, S. Moya, H. Lichtenfeld, A. Casoli, H. Fiedler, E. Donath, H. Moehwald, The decomposition process of melamine formaldehyde cores: the key step in the fabrication of ultrathin polyelectrolyte multilayer capsules, Macromolecular Materials and Engineering, 286 (2001) 355-361.

[130] G. Ghosh, Dispersion-equation coefficients for the refractive index and birefringence of calcite and quartz crystals, Optics Communications, 163 (1999) 95-102.

[131] ASTM International, ASTM Standard C157: Standard test method for length change of hardened hydraulic-cement mortar and concrete, West Conshohocken, PA, 2014.

[132] ASTM International, ASTM Standard C305: Standard practice for mechanical mixing of hydraulic cement pastes and mortars of plastic consistency, West Conshohocken, PA, 2014.

[133] D.R. Bauer, Melamine formaldehyde cross-linker - characterization, network formation and cross-link degradation, Progress in Organic Coatings, 14 (1986) 193-218.

[134] X.H. Li, S.Z. Yang, W.D. Xiang, Q. Shi, A novel porous supramolecular complex constructed by the co-crystallization of melamine and sulfate via hydrogen bonds and aromatic pi-pi interaction, Structural Chemistry, 18 (2007) 661-666.

[135] C. Hall, Water Sorptivity of Mortars and Concretes - a Review, Magazine of Concrete Research, 41 (1989) 51-61.

[136] C. Hall, W.D. Hoff, S.C. Taylor, M.A. Wilson, B.G. Yoon, H.W. Reinhardt, M. Sosoro, P.

Meredith, A.M. Donald, Water Anomaly in Capillary Liquid Absorption by Cement-Based Materials, Journal of Materials Science Letters, 14 (1995) 1178-1181.

[137] N. Neithalath, Analysis of moisture transport in mortars and concrete using sorption-diffusion approach, ACI Journal, 103 (2006) 209-217.

[138] Y. Xi, Z.P. Bažant, L. Molina, H.M. Jennings, Moisture diffusion in cementitious materials Moisture capacity and diffusivity, Advanced Cement Based Materials, 1 (1994) 258-266.

[139] T.C. Powers, T.L. Brownyard, Studies of the physical properties of hardened portland cement paste, Journal of American Concrete Institute, 43 (1947) 469-504.

[140] J.F. Young, S. Mindess, A. Bentur, R. Gray, The Science and Technology of Civil Engineering Materials, Prentice Hall, 1998.

[141] D.W. Hobbs, The dependence of the bulk modulus, Young's modulus, creep, shrinkage, and thermal expansion of concrete upon aggregate volume concentration, Materials and Structures/Research and Testing (Paris), 4 (1971) 107-114.

[142] G. De Schutter, L. Taerwe, Degree of hydration-based description of mechanical properties of early age concrete, Materials and Structures, 29 (1996) 335-344.

[143] M. Hossain, C. Ketata, Experimental study of physical and mechanical properties of natural and synthetic waxes using uniaxial compressive strength test, In: Proceeding of Third International Conference on Modeling, Simulations and Applied Optimalization, (2009) 1-5.

[144] X.Q. Chen, S.L. Zhang, G.J. Wagner, W.Q. Ding, R.S. Ruoff, Mechanical resonance of quartz microfibers and boundary condition effects, Journal of Applied Physics, 95 (2004) 4823-4828.

[145] R. Hill, The elastic behaviour of a crystalline aggregate, Proceedings of the Physical Society. Section A, 65 (1952) 349-354.

[146] Y. Miyazaki, A.G. Marangoni, Structural-mechanical model of wax crystal networks -a mesoscale cellular solid approach, Materials Research Express, 1 (2014) 025101.

[147] K.G. Babu, D.S. Babu, Behaviour of lightweight expanded polystyrene concrete containing silica fume, Cement and Concrete Research, 33 (2003) 755-762.

[148] A. Turatsinze, J.L. Granju, S. Bonnet, Positive synergy between steel-fibres and rubber aggregates: Effect on the resistance of cement-based mortars to shrinkage cracking, Cement and Concrete Research, 36 (2006) 1692-1697.

[149] K.C. Jajam, H.V. Tippur, Role of inclusion stiffness and interfacial strength on dynamic

matrix crack growth: an experimental study, International Journal of Solids and Structures, 49 (2012) 1127-1146.

[150] P. Jongvisuttisun, K.E. Kurtis, The role of hardwood pulp fibers in mitigation of early-age cracking, Cement and Concrete Composites, 57 (2015) 84-93.

[151] A. Schwartzentruber, M. Philippe, G. Marchese, Effect of PVA, glass and metallic fibers, and of an expansive admixture on the cracking tendency of ultrahigh strength mortar, Cement and Concrete Composites, 26 (2004) 573-580.

[152] ASTM International, ASTM Standard C496/C496M: Standard test method for splitting tensile strength of cylindrical concrete specimens, West Conshohocken, PA, 2011.

[153] ASTM International, ASTM Standard C469/C469M: Standard test method for static modulus of elasticity and Poisson's ratio of concrete in compression, West Conshohocken, PA, 2014.

[154] A.B. Hossain, J. Weiss, Assessing residual stress development and stress relaxation in restrained concrete ring specimens, Cement and Concrete Composites, 26 (2004) 531-540.

[155] J.H. Moon, J. Weiss, Estimating residual stress in the restrained ring test under circumferential drying, Cement and Concrete Composites, 28 (2006) 486-496.

[156] H.R. Shah, J. Weiss, Quantifying shrinkage cracking in fiber reinforced concrete using the ring test, Materials and Structures, 39 (2006) 887-899.

[157] W. Dong, X.M. Zhou, Z.M. Wu, Influence of Specimen Thicknesson Cracking Behaviorin Restrained Shrinkage Ring Test, International Journal of Engineering and Technology, (2013) 698-702.

[158] A.B. Hossain, J. Weiss, The role of specimen geometry and boundary conditions on stress development and cracking in the restrained ring test, Cement and Concrete Research, 36 (2006) 189-199.

[159] ACI Standard 318: Building code requirements for structural concrete, Farmington Hills, MI, 2014.

[160] R. Francois, G. Arliguie, Effect of the ITZ damage on durability of reinforced concrete in chloride environment, Materials Research Society Symposium Proceedings, 370 (1995) 465-470.

[161] R. Gao, P. Stroeven, Particle packing and microstructure of the ITZ in cement-based materials, MCCI'2000: International Symposium on Modern Concrete Composites & Infrastructures, Vol I, (2000) 105-110.

[162] K.L. Scrivener, A.K. Crumbie, P. Laugesen, The interfacial transition zone (ITZ) between cement paste and aggregate in concrete, Interface Science, 12 (2004) 411-421.

[163] V. Birman, K. Chandrashekhara, M.S. Hopkins, J.S. Volz, Strength analysis of particulate polymers, Composites Part B: Engineering, 54 (2013) 278-288.

[164] E.J. Garboczi, J.G. Berryman, Elastic moduli of a material containing composite inclusions: effective medium theory and finite element computations, Mechanics of Materials, 33 (2001) 455-470.

[165] B.A. Young, A.M.K. Fujii, A.M. Thiele, A. Kumar, G. Sant, E. Taciroglu, L. Pilon, Effective elastic moduli of core-shell-matrix composites, Mechanics of Materials, 92 (2016) 94-106.

[166] I. Yoshitake, F. Rajabipour, Y. Mimura, A. Scanlon, A Prediction Method of Tensile Young's Modulus of Concrete at Early Age, Advances in Civil Engineering, 2012 (2012) 1-10.

[167] I. Yoshitake, W.B. Zhang, Y. Mimura, T. Saito, Uniaxial tensile strength and tensile Young's modulus of fly-ash concrete at early age, Construction and Building Materials, 40 (2013) 514-521.

[168] N.X. Xie, W. Liu, Determining Tensile Properties of Mass Concrete by Direct Tensile Test, ACI Materials Journal, 86 (1989) 214-219.

[169] S. Swaddiwudhipong, H.R. Lu, T.H. Wee, Direct tension test and tensile strain capacity of concrete at early age, Cement and Concrete Research, 33 (2003) 2077-2084.

[170] K. Sakata, A Study on Moisture Diffusion in Drying and Drying Shrinkage of Concrete, Cement and Concrete Research, 13 (1983) 216-224.

[171] A. Radlinska, B. Pease, J. Weiss, A preliminary numerical investigation on the influence of material variability in the early-age cracking behavior of restrained concrete, Materials and Structures, 40 (2007) 375-386.

[172] A. Radlinska, F. Rajabipour, B. Bucher, R. Henkensiefken, G. Sant, J. Weiss, Shrinkage Mitigation Strategies in Cementitious Systems: A Closer Look at Differences in Sealed and Unsealed Behavior, Transportation Research Record: Journal of the Transportation Research Board, 2070 (2008) 59-67.

[173] A. Radlinska, J. Weiss, Toward the Development of a Performance-Related Specification for Concrete Shrinkage, Journal of Materials in Civil Engineering, 24 (2012) 64-71.

[174] D. Leguillon, C. Lacroix, E. Martin, Matrix crack deflection at an interface between a stiff matrix and a soft inclusion, Damage, Fatigue, Fracture., 328 (2000) 19-24.

[175] E.M. Wouterson, F.Y.C. Boey, X. Hu, S.-C. Wong, Specific properties and fracture

toughness of syntactic foam: effect of foam microstructures, Composite Science and Technology, 65 (2005) 1840-1850.

[176] R.A. Schapery, Thermal expansion coefficients of composite materials based on energy principles, Journal of Composite Materials, 2 (1968) 380-404.

[177] Z. Hashin, Analysis of composite materials - a survey, Journal of Applied Mechanics, 50 (1983) 481-505.

[178] S. Walker, D.L. Bloem, W.G. Mullen, Effects of temperature changes on concreet as influenced by aggregates, Journal of Proceedings of the American Concrete Institute, 48 (1952) 661-679.

[179] D.J. Hart, H.F. Wang, Laboratory measurements of a complete set of poroelastic moduli for Berea sandstone and Indiana limestone, Journal of Geophysical Research-Solid Earth, 100 (1995) 17741-17751.

[180] W. Martienssen, H. Warlimont, Springer Handbook of Condensed Matter and Materials Data, Springer Science & Business Media, New York, NY, 2006.

[181] L.F. Cabeza, Advances in Thermal Energy Storage Systems: Methods and Applications, Elsevier, Cambridge, UK, 2014.

[182] L.L.C. MatWeb, MatWeb material property data, (2013) http://www.matweb.com, Accessed: Oct 2016.

[183] J. Oishi, T. Kimura, Thermal expansion of fused quartz, Metrologia, 5 (1969) 50-55.

[184] K. Hall, S. Tayabji, Coefficient of thermal expansion in concrete pavement design, Tech. Rep. 2011.

[185] Trends in global CO_2 emissions, 2016 Report, PBL Netherlands Environmental Assessment Agency. http://edgar.jrc.ec.europa.eu/news_docs/jrc-2016-trends-in-global-co2-emissions-2016-report-103425.pdf (accessed June 1, 2017).

[186] Z. Wei, G. Falzone, B. Wang, A. Thiele, G. Puerta-Falla, L. Pilon, N. Neithalath, G. Sant, The durability of cementitious composites containing microencapsulted phase change materials, Cement and Concrete Composites, 81 (2017) 66-76.

[187] T. Oey, J. Timmons, P. Stutzman, J.W. Bullard, M. Balonis, M. Bauchy, G. Sant, An improved basis for characterizing the suitability of fly ash as a cement replacement agent, Journal of the American Ceramic Society, 00 (2017) 1-16.

[188] S. Solomon, G.K. Plattner, R. Knutti, P. Friedlingstein, Irreversible climate change due to

carbon dioxide emissions, Proceedings of the National Academy of Sciences, 106 (2009) 1704-1709.

[189] ASTM International, ASTM Standard C109/C109M: Standard test method for compressive strength of hydraulic cement mortars, West Conshohocken, PA, 2012.

[190] R.C. CPC-18, Measurement of hardened concrete carbonation depth, Materials and Structures, 21 (1988) 453-455.

[191] C.-F. Chang, J.-W. Chen, The experimental investigation of concrete carbonation depth, Cement and Concrete Research, 36 (2006) 1760-1767.

[192] D. Kulik, U. Berner, E. Curti, Modelling chemical equilibrium partitioning with the GEMS-PSI code, PSI Scientific Report, 2004.

[193] T. Thoenen, D. Kulik, Nagra/PSI chemical thermodynamics database 01/01 for the GEM-Selektor (V.2-PSI) geochemical modeling code, PSI TM-44-02-09, 2003.

[194] D. Kulik, T. Wagner, S. Dmytrieva, G. Kosakowski, F. Hingerl, K. Chudnenko, U. Berner, GEM-Selektor geochemical modeling package: revised algorithm and GEMS3K numerical kernel for coupled simulation codes, Computers & Geosciences, 17 (2013) 1-24.

[195] J.W. Johnson, E.H. Oelkers, H.C. Helgeson, SUPCRT92: A software package for calculating the standard molal thermodynamic properties of minerals, gases, aqueous species, and reactions from 1 to 5000 bar and 0 to 1000°C, Computers & Geosciences, 18 (1992) 899-947.

[196] J.P. Hamilton, C.G. Pantano, Effects of glass structure on the corrosion behavior of sodium-aluminosilicate glasses, Journal of Non-Crystalline Solids, 222 (1997) 167-174.

[197] F. Bouville, A.R. Studart, Geologically-inspired strong bulk ceramics made with water at room temperature, Nature Communications, 8 (2017) 14655.

[198] A. Kumar, T. Oey, G. Falzone, J. Huang, M. Bauchy, M. Balonis, N. Neithalath, J. Bullard, G. Sant, The filler effect: The influence of filler content and type on the hydration rate of tricalcium silicate, Journal of the American Ceramic Society, 100 (2017) 3316-3328.

[199] F. Bellmann, G.W. Scherer, Analysis of C-S-H growth rates in supersaturated conditions, Cement and Concrete Research, (2017) http://dx.doi.org/10.1016/j.cemconres.2017.1005.1007.

[200] T. Wang, H. Huang, X. Hu, M. Fang, Z. Luo, R. Guo, Accelerated mineral carbonation curing of cement paste for CO_2 sequestration and enhanced properties of blended calcium silicate, Chemical Engineering Journal, 323 (2017) 320-329.

[201] F. Barthelat, H. Tang, P.D. Zavattieri, C.M. Li, H.D. Espinosa, On the mechanics of mother-

of-pearl: A key feature in the material hierarchical structure, J Mech Phys Solids, 55 (2007) 306-337.

[202] H.L. Gao, S.M. Chen, L.B. Mao, Z.Q. Song, H.B. Yao, H. Colfen, X.S. Luo, F. Zhang, Z. Pan, Y.F. Meng, Y. Ni, S.H. Yu, Mass production of bulk artificial nacre with excellent mechanical properties, Nature Communications, 8 (2017) 287.

[203] C. Ortiz, M.C. Boyce, Bioinspired structural materials, Science, 319 (2008) 1053-1054.

[204] U.G.K. Wegst, H. Bai, E. Saiz, A.P. Tomsia, R.O. Ritchie, Bioinspired structural materials, Nature Materials, 14 (2015) 23-36.

[205] H.A. Lowenstam, S. Weiner, On Biomineralization, Oxford University Press, 1989.

[206] P. Atkins, J. de Paula, Elements of Physical Chemistry, 5th ed., Oxford University Press, 2007.

[207] S.C. Ma, J. Chai, K.L. Jiao, L. Ma, S.J. Zhu, K. Wu, Environmental influence and countermeasures for high humidity flue gas discharging from power plants, Renewable and Sustainable Energy Review, 73 (2017) 225-235.

[208] A. Morandeau, M. Thiery, P. Dangla, Investigation of the carbonation mechanism of CH and C-S-H in terms of kinetics, microstructure changes and moisture properties, Cement and Concrete Research, 56 (2014) 153-170.

[209] T.A. Bier, J. Kropp, H.K. Hilsdorf, Carbonation and Realcalinisation of Concrete and Hydrated Cement Paste, in: J.C. Maso (Ed.) Durability of Construction Materials, Chapman and Hall, London-New York, 1987, pp. 927-934.

[210] T.A. Bier, J. Kropp, H.K. Hilsdorf, Formation of silica gel during carbonation of cementitious systems containing slag cements, ACI Special Publications SP 14-69, (1989) 1413-1428.

[211] L. Fernandez-Diaz, J.M. Astilleros, C.M. Pina, The morphology of calcite crystals grown in a porous medium doped with divalent cations, Chemical Geology, 225 (2006) 314-321.

[212] L.A. Perez-Maqueda, J.M. Criado, P.E. Sanchez-Jimenez, Combined kinetic analysis of solid-state reactions: a powerful tool for the simultaneous determination of kinetic parameters and the kinetic model without previous assumptions on reaction mechanism, Journal of Physical Chemistry A, 110 (2006) 12456-12462.

[213] F.J. Gotor, J.M. Criado, J. Malek, N. Koga, Kinetic analysis of solid-state reactions: the universality of master plots for analyzing isothermal and nonisothermal experiments, Journal of

Physical Chemistry A, 104 (2000) 10777-10782.

[214] S. Vyazovkin, C.A. Wight, Isothermal and nonisothermal reaction kinetics in solids: in search of ways toward consensus, Journal of Physical Chemistry A, 101 (1997) 8279-8284.

[215] J.H. Sharp, G.W. Brindley, B.N. Narahari Achar, Numerical data for some commonly used solid state reaction equations, Journal of the American Ceramic Society, 49 (1966) 379-382.

[216] M. Thiery, G. Villain, P. Dangla, G. Platret, Investigation of the carbonation front shape on cementitious materials: Effects of the chemical kinetics, Cement and Concrete Research, 37 (2007) 1047-1058.

[217] O. Levenspiel, Chemical Reaction Engineering, John Wiley & Sons, New York, 1999.

[218] A. Khawam, R. Flanagan, Solid-state kinetic models: Basics and mathematical fundamentals, Journal of Physical Chemistry B, 110 (2006) 17315-17328.

[219] Production and use of coal combustion products in the U.S., American Road and Transportation Builders Association, 2015.

[220] Coal ash recycling reaches 52 percent as production and use trends shift, American Coal Ash Association, October 2016. https://www.acaa-usa.org/Portals/9/Files/PDFs/News-Release-Coal-Ash-Production-and-Use-2015.pdf (accessed September 5, 2017).

[221] U.S. Energy Information Administration: How much of U.S. carbon dioxide emissions are associated with electricity generation? https://www.eia.gov/tools/faqs/faq.php?id=77&t=11 (accessed September 5, 2017)

[222] J.M. Matter, M. Stute, S.O. Snaebjornsdottir, E.H. Oelkers, S.R. Gislason, E.S. Aradottir, B. Sigfusson, I. Gunnarsson, H. Sigurdardottir, E. Gunnlaugsson, G. Axelsson, H.A. Alfredsson, D. Wolff-Boenisch, K. Mesfin, D.F.D. Taya, J. Hall, K. Dideriksen, W.S. Broecker, Rapid carbon mineralization for permanent disposal of anthropogenic carbon dioxide emissions, Science, 352 (2016) 1312-1314.

[223] R.F. Service, Cost of carbon capture drops, but does anyone want it?, Science, 354 (2016) 1362-1363.

[224] Carbon Capture, Utilization, and Storage: Climate Change, Economic Competitiveness, and Energy Security. U.S. Department of Energy, 2016. https://energy.gov/sites/prod/files/2016/09/f33/DOE%20-%20Carbon%20Capture%20Utilization%20and%20Storage_2016-09-07.pdf (accessed June 5, 2017).

128

[225] W.M. Budzianowski, Implementing carbon capture, utilisation and storage in the circular economy, International Journal of Global Warming, 12 (2017) 272-296.

[226] M.Z.M. Salem, M. Bohm, J. Berankova, J. Srba, Effect of some manufacturing variables on formaldehyde release from particleboard: Relationship between different test methods, Building and Environment, 46 (2011) 1946-1953.

[227] S.Y. Yu, X.D. Wang, D.Z. Wu, Microencapsulation of n-octadecane phase change material with calcium carbonate shell for enhancement of thermal conductivity and serving durability: Synthesis, microstructure, and performance evaluation, Applied Energy, 114 (2014) 632-643.

[228] R. Siddique, Waste Materials and By-Products in Concrete, Springer, 2008.

[229] J. Choi, H. Lee, S. Hong, Capacitive deionization (CDI) integrated with monovalentcation selective membrane for producing divalent cation-rich solution, Desalination, 400 (2016) 38-46.

[230] H. Sakar, O. Karatas, C.B. Canbolat, B. Keskinler, A. Karagunduz, Removal of ammonium ions by capacitive deionization and membrane capacitive deionization units, Desalination and Water Treatment, 75 (2017) 260-267.

[231] W.W. Tang, D. He, C.Y. Zhang, T.D. Waite, Optimization of sulfate removal from brackish water by membrane capacitive deionization (MCDI), Water Research, 121 (2017) 302-310.